Numerical and Granulometric Approaches to Geophysical Granular Flows

By

Sébastien Dartevelle

A DISSERTATION

Submitted in partial fulfillment of the requirements for the degree of

DOCTOR of PHILOSOPHY

Department of Geological and Mining Engineering and Sciences

MICHIGAN TECHNOLOGICAL UNIVERSITY

2003

This dissertation, “Numerical and Granulometric Approaches to Geophysical Granular Flows”, is hereby approved in partial fulfillment of the requirements for the degree of DOCTOR of PHILOSOPHY in the field of Applied Mathematics and Geophysics.

Department of Geological and Mining Engineering and Sciences.

Dissertation advisor	Dr. William I. Rose, Michigan Technological University
Dissertation co-advisor	Dr. John Stix, McGill University
Department chair	Dr. Wayne D. Pennington, Michigan Technological University

Houghton, Michigan,

_____

Date

Table of Contents

List of Figures

List of Tables

List of Annexes

List of Appendixes

"*Making the simple complicated is common place;*
making the complicated simple, awesomely simply, that is creativity."

Charles Mingus (1922-1979).

Executive Summary

This dissertation explores granular matter and processes in volcanology. Granular materials display a wide variety of behavior and features. They cannot be easily classified as solids, gas or liquids, and should be seen as a new state of matter, *granular*. Granular flows are economically important (in the pharmaceutical industry, corn flow in a silo, coal and flour in a bin, granular material flowing under the action of gravity in a hopper) and often associated with gigantic, dangerous, deadly and devastating phenomena, either natural (e.g., plinian clouds, pyroclastic-surges and -flows, turbidity currents, landslides, snow avalanches, dusty clouds generated by forest fire, dust storms), or man-made (e.g., mushroom and surge clouds formed by nuclear explosion). Because geophysical granular flows display a wide variety of behaviors over many scales, they are poorly understood in geophysics-volcanology. Yet the need to approach, understand, and characterize them in better ways has never been so important owing to the potential damage they may cause to humans, living stock, environment, and the potential disruption of a local economy as seen for instance during the 1991 Mount Pinatubo eruption in the Philippines. Therefore, this dissertation objectives are threefold, which can be summarized as follow and are further developed in the next three chapters:

- *First* (chapter 1): how to best characterize a given set of grains within pyroclastic deposits in order to infer key properties regarding the flowing processes? This dissertation develops new tools in grainsize analyses of pyroclastic deposits based upon theoretical developments achieved in mining engineering and atmospheric sciences. It contrasts the dimensionless phi-scale solely used in volcanology and geology with the more conventional metric-scale and metric grainsize parameters rather used in other scientific and engineering fields. This first chapter shows some applications of the new grainsize approach. For instance, it highlights the fundamental grainsize differences between pyroclastic-flow vs. -surge deposits and plinian fallout vs. co-ignimbrite fallout deposits. This allows us, for instance, to conclude that the fallout deposit from the 15 June 1991 Mt. Pinatubo had a major coignimbrite origin instead of a solely plinian origin as previously thought. With these new grainsize parameters (and those of the traditional phi-scale), volcanologists should have accurate and powerful tools to characterize a set of grains within pyroclastic deposits and, hopefully, tools for better constraining the physical processes that have generated them. We may conclude with this new grainsize approach that a specific flowing

process of granular materials may develop unique grainsize characteristics, which leads us to the second and third objectives of this Ph.D. project.

- *Second* (chapter 2): how to model geophysical granular mass flows (e.g., pyroclastic-flows, surges, plinian clouds)? This chapter explores the theoretical foundations of flowing and depositional mechanisms of granular media (diluted and concentrated). We demonstrate that there are three fundamental regimes in a flowing granular medium, which are essentially controlled by the grain volumetric concentration: kinetic, kinetic-collisional, and frictional. Therefore, the rheological behavior within pyroclastic-flows and -surges may be -at any time and anywhere- unsteady, non-uniform and highly nonlinear. These theoretical facts are backed up by more than 30 years of experiments and modeling efforts in chemical engineering and fluid dynamics, which are reviewed in this chapter. In addition to these three regimes, granular flows own a distinctive and fundamental feature, their multiphase nature, making them the most challenging kind of flow to model and simulate. Indeed, in geophysics, a granular medium can be typically defined as *a collection of discrete, solid particles dispersed in a moving interstitial fluid*. Clearly, modeling granular flows -hence pyroclastic phenomena- with a pseudo-gas assumption (i.e., monophase), with linear rheologies (e.g., Bingham, Newtonian), or with an inviscid assumption, is a plain denial -not even a rough approximation- of their true nature. Unfortunately, such denial of their multiphase nature and of their nonlinear rheology is commonplace in volcanology which explains why, so far, modeling efforts in volcanology have failed to shed lights on the exact nature of the flowing process (expanded vs. concentrated) and the exact nature of the depositional process (progressive aggradation vs. en masse). With this in mind, we have developed an hydrodynamic model and its constitutive equations for modeling granular media at any concentrations. We particularly focus on the plastic (i.e., frictional) formulation which turns out to be the critical element of our mathematical model for rightly simulate depositional processes. Throughout this chapter, we systematically discuss the key assumptions behind the mathematical model and its shortcomings. Even though there is room for improvements (i.e. two way-coupling between turbulence of solid and gas phases), we believe such model represents a major step forward in the modeling of geophysical granular flows as demonstrated in the last chapter of this thesis dissertation.

- *Third* (chapter 3): How to (best) numerically solve the mathematical multiphase model presented in chapter 2? And what are the practical potentialities in geophysics and in volcanology

of such a numerical approach? The numerical tool used in this project is a FORTRAN 90 general purpose multiphase code developed by the National Energy Technology Laboratory (NETL) and Oak Ridge National Laboratory (ORNL): **M**ultiphase **F**low with **I**nterphase e**X**change (MFIX). We have further adapted MFIX into a **G**eophysical-atmospherical version, (G)MFIX, in keeping all the capabilities of MFIX and adding new ones for typical geophysical applications. The practical potentialities of both the mathematical model and (G)MFIX are shown in answering some of the most debated and heated questions in volcanology; such as, (1) Are numerical multiphase models able to simulate into the atmosphere a complete and stable plinian cloud over a long period of time?, (2) Are pyroclastic-flows expanded (diluted) or concentrated? In other words, how do pyroclastic-flows exactly move?, (3) What is the main depositional process of pyroclastic-flow, *en masse* or progressive aggradation?, (4) Is there a continuum between pyroclastic-flow and -surges? And, somehow related to this, how does flow transformation occur (pyroclastic-flows↔pyroclastic-surges)? Some of those questions can only be answered if we redefine the concepts of pyroclastic-surges and -flows in the lights of classical granular theories. Yet answers are not always straightforward to formulate as our scientific background may deeply influence the way we interpret the results. For instance, from the kinetic granular standpoint, there is a strict continuum between expanded, dilute flow and concentrated collisional flows, and a clear discontinuity between kinetic-collisional and frictional flows. However volcanologists and geologists tend to define discontinuities (if any) based upon field evidences within the deposit. Hence the concept of continuum or not between pyroclastic-flows and -surges is rather based, for instance, upon concentration gradient within the flow. In this case, there are very little evidences from our simulations for supporting any sort of continuity between kinetic, expanded surges and collisional, concentrated flows. Clearly, volcanologist modelers must somehow compromise between different scientific and engineering fields. Besides pyroclastic-flow and -surge simulations, chapter 3 demonstrates that within the limitations of our mathematical model (and the way it treats turbulence), multiphase flow computer models are able to simulate complete and stable plinian clouds. This would hopefully cut short the arguments of those who believe that multiphase codes are, if not inherently flawed, at best, clumsy, sophisticated, and obscure tools. But, more importantly, this allows us to validate our work in comparing with remote-sensing data of plinian clouds, with simple observations of historical eruptions (e.g., height vs. mass flux), and with previous plume and jet theoretical developments. This dissertation research has potentially opened new doors for multiphase computer models in the fields of atmospheric sciences, airborne dispersion models, and, of course, explosive volcanology at large.

In conclusions, the major part of this dissertation tackles one of the most challenging problem in geophysical computational fluid dynamics: how to model both dilute and concentrate granular flows? We show that it is possible to model and simulate them with an unified mathematical model and computer codes. However, we also acknowledge that there is still room for achievable improvements over the next decade or so:

1- The first and most important task to be accomplished is to include a true multiphase turbulence model to account for the two-way coupling between turbulence in the gas phase and turbulence in the solid phase. We have disregarded such two-way coupling as it is beyond the time frame of this Ph.D. project and beyond our current computer capabilities. However, the exact rheological behavior of the dilute part of granular flows is expected to be deeply influenced by multiphase turbulence. Such daunting task is worth embarking upon as it would allow us to understand and simulate unsuspected rich and subtle physics. For instance, we surmise that it may enable us to model grain-clustering within dusty turbulent clouds (hence to understand the second maximum in fallout deposit?). This overall task is intellectually and technically challenging but a prerequisite step forward for those who want to rightly approach diluted granular flows.

2- The second task is to include water phase change (i.e., condensation, sublimation, evaporation). Such a phenomenon may deeply influence the thermodynamic of a rising stratospheric wet dusty cloud (e.g., plinian, coignimbrite). Theoretically, it should no be too much a difficulty, even though, it would imply to perform simulations with supplementary phases (liquid water, ice, others …), hence imply more powerful computer capabilities. In addition, turbulence models must be included in the rate of mass transfer between phases.

3- Natural granular flows are made of grains of different sizes. Although (G)MFIX and MFIX can perform multi grainsize simulations, we believe -within this current project- it would have added unnecessary complexities in the understanding of basic granular rheologies. Even though other multiphase modelers in volcanology perform simulations with more than three grainsizes, their results are *de facto* questionable knowing they have completely overlooked the true nonlinear rheological behavior of granular flows. Nevertheless, there is a necessity -in the long run- to simulate granular flows with more than one grainsize provided that multi-grainsize rheology and turbulence is mastered and

understood. Within the plastic (frictional) model presented in chapter 2, there should be no problem to include more than one grainsize. However, this may be more complicate within the kinetic-collisional rheology because it would imply a complete reformulation of the theoretical model presented in this dissertation.

This dissertation is organized in three chapters, each written as journal manuscript. The first chapter, "*Origin of the Mount Pinatubo climactic cloud: Implications for volcanic hazards and atmospheric impacts*" by *Dartevelle et al*. [*2002*] has been published in *Geology*, 30, 663-666, July 2002. We present here the exact published version plus two unpublished supplementary annexes describing the mathematical formulation of the new grainsize parameters (Annex 2) and the variation with distance from source of the amount of PM_{10} in the Askja and Mt. Pinatubo fallout deposits (Annex 3). The second chapter "*Numerical modeling of geophysical granular flows: Part I. A review of multiphase flow models and granular rheologies*" by *Dartevelle* [*2003*] and the third chapter "*Numerical modeling of geophysical granular flows: Part II. Computer simulations of plinian clouds, pyroclastic flows and surges*" by *Dartevelle et al*. [*2003*] will be both submitted by September 2003 to one of the journals of the American Geophysical Union (AGU), either *G-cubed* (the new AGU web-based journal) or the *Journal of Geophysical Research* (traditional paper format). Chapter 2 has a supplementary annex describing the effective molecular (non-turbulent) heat conductivity model in a multiphase system (Annex 4). Chapter 3 has two supplementary annexes which demonstrate grid-size independence of (G)MFIX for plinian cloud simulations (Annex 5) and which detail the numerical scheme and technique used in (G)MFIX codes (Annex 6). These annexes will not be submitted for publication owing to the strict AGU journals space limitation. Each chapter can be read as an independent manuscript. All tables, figures, and annexes are located at the end of each chapter (after the captions).

Because we strongly believe that Sciences should be built upon sharing principles and openness, we have developed during this Ph.D. project a website entirely devoted to granular matter and processes:

http://www.granular.org

and

http://www.granular-volcano-group.org

where can be found the complete mathematical model, its demonstration, and all our numerical simulations. This website is entirely part of the this Ph.D. project. For instance, most of chapter 2 is a condensed version of the theoretical contents of this website.

This web project was selected as the best resource of the web by the "American Association for the Advancement of Science" (AAAS), the "American Institute of Physics" (AIP), the "Mathematical Association of America" (MAA), the "Particle Technology Forum" (PTF) of the "American Institute of Chemical Engineers" (AIChE).

The U.S. Department of Energy (DOE) selected this project as a "Science and Technology Research Highlight" (August 2002). This Ph.D. project and its web emanation have been very generously highlighted by *Science* magazine, "*Totally Granular*", 297, 483, July 2002.

We have computer generated animation movies of all the simulations analyzed in chapter 3. Those movies can be watched and downloaded from the two following websites (including the PDF version of this dissertation thesis):

http://www.geo.mtu.edu/volcanoes/granular/

and

http://www.granular.org/phd/

Those animation movies can be watched with the latest version of either Microsoft Windows Media Player, RealAudio Player One, or QuickTime Player, which can be all downloaded for free on their respective websites.

Acknowledgements

I warmly thank my two Ph.D. advisors, Prof. William I. Rose and Prof. John Stix, for their assistances and advices. I am particularly thankful for their trusts and for giving me the opportunity and the liberty to achieve my project as I have imagined and wanted it since the very first day. This "taste" of freedom has been unique and fundamentally important for the achievement of this project. I also acknowledge Dr. James W. Vallance for his support in my "transfer" to Michigan Tech Ph.D. program.

I thank my Ph.D. committee for their interests in this project, *viz.*, Prof. A. Mayer, Prof. M. Mullins, and Dr. J.W. Vallance.

I am grateful to all the "MFIX-team" at the National Energy Technology Laboratory (NETL) and the Oak Ridge National Laboratory (ORNL) for sharing their multiphase computer codes and their assistance, *viz*., Dr. S. Pannala, Dr. M. Syamlal, Dr. T. O'Brien, and Mr. P. Nicolleti.

I am obliged to Prof. T. Druitt and Prof. K. Kelfoun for inviting me and financially supporting me during my two months stay in Clermont-Ferrand, France, in 2001.

I also wish to warmly cheer all the volcano graduate students at Michigan Tech.

And, of course, I do not forget all the fine people who have crossed, randomly or not, my path these past years.

Houghton, Michigan, 5 July 2003.

Chapter 1.

Origin of the Mount Pinatubo climactic eruption cloud Implications for volcanic hazards and atmospheric impacts

Keywords: grain size, PM_{10}, specific surface area, Pinatubo, pyroclastic deposits, Plinian, coignimbrite, volcanic hazards.

"*No great advances has never been made in science, politics, or religion without controversy.*"

Lyman Beecker (1775-1863).

Abstract

Volcanic ash clouds can be fed by an upward-directed eruption column (Plinian column) or by elutriation from extensive pyroclastic-flows (coignimbrite cloud). For large-scale eruptions, there is considerable uncertainty about which mechanism is dominant. Here we analyze in a novel way a comprehensive grainsize database for pyroclastic deposits. We demonstrate that the Mount Pinatubo climactic eruption deposits were substantially derived from coignimbrite clouds, and not only by a Plinian cloud as generally thought. Coignimbrite ash-fall deposits are much richer in breathable <10 μm ash (5–25 wt%) than pure Plinian ash at most distances from the source volcano. We also show that coignimbrite ash clouds, as at Pinatubo, are expected to be more water rich than Plinian clouds, leading to removal of more HCl prior to stratospheric injection, thereby reducing their atmospheric impact.

This work has been published in:

Geology, v.30, n.7, p. 663-666, July 2002; 3 figures and data repository item 2002071.

1. Introduction

Volcanic ash clouds are a significant hazard to aircraft [*Rose et al., 1995; Casadevall et al., 1996; Sparks et al., 1997*], involve chemical reactions [*Hofmann and Solomon, 1989; Mankin et al., 1992; Tabazadeh and Turco, 1993*], affect the global climate [*Sparks et al., 1997*], and pose potential health risks [*Óskarsson, 1980; Mercado et al., 1996; Norton and Gunter, 1999; Baxter, 2000*]. Ash clouds can be fed by an upward-directed eruption column (Plinian column; Figure 1A) or elutriated from extensive pyroclastic-flows generated by fountain collapse (coignimbrite ash cloud; Figure 1B) [*Sparks et al., 1997*]. Knowledge of the ash cloud origin is very important since the impacts on animal and human health, on the environment, and on aircraft safety may differ greatly. Coignimbrite ash clouds are much richer in breathable dust-size ash and can be substantially richer in water and ice than Plinian columns reaching the same height. As pyroclastic-flows move downslope, they entrain moist tropospheric air and incorporate water by vaporizing streams, lakes, seawater, snow or ice.

Evaluations of atmospheric impacts and health hazards of the Pinatubo ash cloud have previously assumed a dominant Plinian eruption-column origin. Here, we demonstrate that the Pinatubo fall deposit is unusually fine grained for a Plinian deposit, and that all grainsize features can be reconciled with a major coignimbrite origin.

2. Climactic eruption of Mount Pinatubo

The Pinatubo climactic eruption on June 15, 1991, was one of the largest of the twentieth century. The eruption cloud reached 34 km in height [*Koyaguchi and Tokuno, 1993*], lasted more than ~6 h [*Rosi et al., 2001*], and released a bulk tephra volume (fall and flow) of 8.4–10.4 km^3 [*Scott et al., 1996; Paladio-Melosantos et al., 1996*], ~4.5 Mt of HCl, and ~20 Mt of SO_2 [*Tabazadeh and Turco, 1993*], caused by sulfur enrichment of the dacitic magma system [*Bernard et al., 1991*]. The eruption has been widely studied, but the origin of the giant ash cloud remains unclear [*Scott et al., 1996; Rosi et al., 2001*]. It is generally interpreted as a Plinian column (Figure 1A) [*Koyaguchi and Tokuno, 1993; Tabazadeh and Turco, 1993; Holasek et al., 1996; Paladio-Melosantos et al., 1996*]. However, field observations indicate unusual features for a Plinian column deposit, e.g., equal volumes and simultaneous emplacement of pyroclastic flow and fall deposits [*Scott et al., 1996; Paladio-Melosantos et al., 1996; Rosi et al., 2001*]. The flow deposits are depleted in fines [*Scott et al., 1996*], and the fall layer is thin, even close to source [*Paladio-Melosantos et al., 1996; Sparks et al., 1997; Rosi et al., 2001*]. It has been surmised that

the ash cloud may not have been Plinian, and that a coignimbrite origin should be evaluated further (Figure 1B) [*Scott et al., 1996; Sparks et al., 1997; Rosi et al., 2001*]. A coignimbrite origin is consistent with satellite observations. Indeed, multispectral digital data [*Holasek et al., 1996; Volon, 1997*], acquired with two AVHRR thermal infrared channels (T4 and T5), show that the volcanic cloud was indistinguishable from meteorological clouds (i.e., T4-T5>0) [*Casadevall et al., 1996; Volon, 1997*]. The positive T4-T5 signatures in the semitransparent regions of the ash cloud are consistent with strong water enrichment and ash particles encased in ice, which prevents detection of their true silicate spectral infrared signature [*Rose et al., 1995*]. Such a water enrichment is not expected for a Plinian column; e.g., a positive anomaly was not observed for the 1982 El Chichón Plinian columns, which also erupted into a wet tropical atmosphere.

3. Story in the Grains

To evaluate the origin of the Pinatubo climactic ash cloud, we measured grainsize characteristics of our own samples collected around Mount Pinatubo (see Annex 1) and analyzed an integrated data set including PHIVOLCS and deep-sea ash data [*Paladio-Melosantos et al., 1996; Wiesner et al., 1995*]. In grain-size analysis, the logarithm of grain "diameter" is traditionally used as the random variable [*Krumbein, 1936*]. This logarithmic scale is named the phi-scale, where $\phi = -\log_2 \frac{d}{d_0}$, d is the grain's linear dimension in mm, and d_0 is taken as 1 mm in order to make the number inside the logarithm dimensionless, hence to prevent erroneously transforming the phi values back to the metric-scale [*McManus, 1963*]. On the other hand, the direct use of "d" as the random variable is logical since it is related to our experience of directly measuring the grains in terms of metric-length units and is routinely used in engineering and aerosol science [e.g., *Rhodes, 1999*]. This study is the first application of this approach to volcanic deposits (see Annex 2). Hence we use first moment and standard deviation (both in meters) of the mass grain-size distribution. The standard deviation measures the dispersion of the grainsize distribution (i.e., metric sorting). We also calculate the bulk specific surface area (SSA), which is the total surface area of a set of grains to their total volume (in m^{-1}). SSA is proportional to the inverse of the Sauter mean diameter of the number grainsize distribution in the metric-scale. SSA of a set of grains is sensitive to the bulk grain size (e.g., it decreases with increasing grainsize) and is a first-order control on heat transfer and chemical exchange between ash and any gas within ash clouds [*Óskarsson, 1980*].

Figure 2 compares variations of mean, sorting and SSA versus distance for the fall deposit from the unambiguously Plinian Askja D deposit, Iceland, 1875 deposits [*Sparks et al., 1981*] and the fall deposit from the Pinatubo climactic eruption ash cloud (layer C). Both Pinatubo and Askja are interpreted as eruptions of relatively similar intensity with respect to the duration of the eruption (~6 h), the wind velocity (~25 m/s) and altitude reached by the columns (~30 km ±4 km) [*Sparks et al., 1981; Carey and Sparks, 1986; Rosi et al., 2001*]. Between 10 and 50 km from source, Pinatubo SSA values are about one to two orders of magnitude higher than those for Askja, while mean and sorting values are about an order of magnitude smaller than those for Askja. In the same distance range, SSA increases 5-fold for Askja, whereas it does not even double for Pinatubo. Those contrasting trends appear exactly as expected by theory if Pinatubo and Askja were coignimbrite and Plinian falls respectively [*Bonadonna et al, 1996*]. Moreover, the Askja deposits show no <10 μm ash (PM_{10}) for locations up to 145 km (Annex 3), while Pinatubo shows a rapid enrichment in PM_{10}, ~5–11 wt% at 10–45 km increasing to 26 wt% at 250–600 km. Such high amounts of PM_{10} are only found ultradistally in Plinian fall deposits after extreme aerial sorting, *e.g.*, ~28 wt% PM_{10} at ~1900 km for Askja falls (Annex 3). All the available data indicate that the Pinatubo giant ash cloud deposited dominantly homogeneous fine ash enriched in PM_{10} (mainly micrometer to millimeter size range, regardless of distance from the source), while the Askja Plinian cloud deposited coarser and more heterogeneous falls.

We also introduce two new grain-size parameters: (1) SSA/mean (in m^{-2}) and (2) mean/sorting (dimensionless). The first ratio distinguishes coarse-grained from fine-grained deposits (e.g., flow from surge deposits, proximal fall from distal fall deposits). The second ratio discriminates gravity-controlled flow and coignimbrite fall deposits from pure Plinian fall deposits. Using Figure 2 for a given deposit, the mean and sorting decay in a similar fashion with distance. Hence, to a first approximation, the mean/sorting ratio does not change much with distance from source, particularly proximally. In Figure 3, we show the grain-size ratios for 600 samples from many locations and eruptive styles (Plinian, subPlinian, Strombolian) representing the main types of pyroclastic activity (surge, flow, fall, and coignimbrite fall) [*Murai, 1961; Kuntz et al., 1981; Sparks et al., 1981; Sigurdson and Carey, 1989; Lirer and Vinci, 1991; Wiesner et al., 1995; Paladio-Melosantos et al., 1996*]. Pyroclastic-flow and -surge deposits have a low mean/sorting ratio relative to Plinian fall deposits, enabling us to separate gravity current from Plinian fall deposits, regardless of the distance from source. As expected for Plinian falls, the SSA/mean ratio increases with distance from the volcano, while the mean/sorting ratio spans the same value range (i.e., ~0.8–2.1 at <100 km and ~1.0–1.6 at >100 km). Also plotted are the coignimbrite falls from

the 1980 Mount St. Helens, and the 1815 Tambora eruptions [*Kuntz et al., 1981; Sigurdson and Carey, 1989*]. Surge and coignimbrite fall deposits span the same range of mean/sorting values as dense pyroclastic-flow (0.1–~1.0) because they are typically derived from them. Hence they are mainly distinguished from flows by contrasting SSA/mean ratios. Elutriation clouds (e.g., surge, coignimbrite clouds) contain mostly fine ash from their parent pyroclastic-flows. Thus their SSA is much higher and their mean much lower than their parent pyroclastic-flows. In Figure 3, Pinatubo fallouts clearly plot in the coignimbrite-surge-flow domain, and not in the Plinian fall domain. On the basis of all available data for Pinatubo, we conclude that the climactic-phase fall layer was substantially derived from an ash cloud fed by large pyroclastic-flows, with a less important role for Plinian input than previously thought.

4. Implications

Compared to Plinian clouds, coignimbrite clouds are richer in breathable fine ash, which poses a threat to human health [*Mercado et al., 1996; Norton and Gunter, 1999; Baxter, 2000*]. Short-term exposure to PM_{10} ash during and after the Pinatubo eruptions was suggested as a possible initiating factor in acute respiratory infections (ARI) leading to chronic obstructive pulmonary diseases (such as pneumonia, bronchitis, bronchial asthma, emphysema). After the Pinatubo eruptions, an average weekly mortality of 16 per 10,000 due to ARIs was documented in 1992 [*Mercado et al., 1996*]. However, in the absence of continuous monitoring of airborne ash levels and their possible health effects, the deaths have been related to measles and pneumonia induced by poor nutritional status and health of victims (R.A. Mercado, P. Baxter and C. Newhall, personal communications, 2001). Today, 11 yr after the Pinatubo eruptions, the PM_{10} fraction of ash resuspended by winds and human activities remains a potential, yet unmonitored, health risk causing many respiratory problems (L. Yoshisaki, 2001, personal communication). This may be aggravated by an average cristobalite content in the Pinatubo PM_{10} of ~2 wt% (measured by Rietveld X-ray diffraction), a level 20 times higher than the minimum level considered to be a potential health hazard [*Smith, 1997*].

Coignimbrite clouds are potentially richer in water than Plinian columns of similar intensity. From local atmospheric profiles taken by the U.S. Air Force on June 15, 1991 and from the *Woods* [*1988*] Plinian column model, we estimate the mass of tropospheric water entrained into the volcanic ash cloud as it rises to be ~42 Mt (assuming a 250 m vent radius at 2 km above sea level). This is small compared to the 500 Mt of magmatic water initially released by the eruption [*Sparks et al., 1997*]. In contrast (S. Sparks, 2001, personal communication), a rising

coignimbrite ash cloud is expected to entrain 60 times more tropospheric water than a Plinian column (~2520 Mt, assuming a minimum averaged basal radius of 10 km for the coignimbrite source within a lower moister atmosphere). As it rises, the water vapor condenses and freezes onto the fine ash, which masks their spectral infrared signature [*Rose et al., 1995; Volon, 1997*]. This water enrichment in coignimbrite clouds for many of the largest eruptions prevents automatic detection of ash clouds using the infrared T4-T5 split window method. This is a cause for concern for aircraft safety during coignimbrite eruptions. For example, there were at least 16 aircraft encounters with the giant Pinatubo ash cloud [*Casadevall et al., 1996*].

The water enrichment also explains why the HCl emitted by Pinatubo was so efficiently scavenged [*Mankin et al., 1992; Tabazadeh and Turco, 1993*]. El Chichón initially released 1.8 Mt of HCl, 60% less than Pinatubo (4.5 Mt) [*Hofmann and Solomon, 1989; Tabazadeh and Turco, 1993*]. However, both eruptions injected equivalent amounts of HCl into the stratosphere (~0.04 Mt) [*Hofmann and Solomon, 1989; Tabazadeh and Turco, 1993*]. Thus, in terms of stratospheric volcanic chlorine injections and their effect on ozone levels, coignimbrite ash clouds should have a smaller impact. Water droplets and ice also scavenge some of the SO_2 emitted, thereby reducing effects from SO_2-derived aerosols on ozone and temperature [*Rose et al., 1995*]. However, higher stratospheric water injections can also lead to higher levels of OH radicals, which contribute to ozone destruction [*Hofmann and Solomon, 1989*]. Models of atmosphere-climate impacts must account for these key differences between Plinian columns and coignimbrite ash clouds.

Since its introduction in the thirties [*Krumbein, 1936*], the phi-scale has been favored by geologists over the metric-scale used in engineering. However, the metric-scale has clear assets. First, it has a dimension, which makes metric grain-size statistics intuitive to interpret and easily usable by theoretical fluid-dynamic models. Second, it has a much larger variety of statistical parameters, opening promising new opportunities for the field of grain-size analysis in geology. Third, because of this, geologists can choose the best parameters depending on the nature of the grainsize frequency function, on the measurement technique, and on their objectives. Fourth, any combination (ratio) of grainsize parameters can be calculated to shed new light on genetic processes without losing any information and physical meaning; e.g., in volcanology, the mean/sorting ratio tends to constrain distance effects along one axis and potentially may be used for quantifying the proportions of ash from different end-member sources (plinian and coignimbrite) within the deposit. In order to capture all the complexities of sedimentological processes, geologists should express their results in more than one manner [*Krumbein, 1936*].

5. References

Baxter, P.J., 2000, Impacts of eruptions on human health, *in* Sigurdsson, H., ed., Encyclopedia of volcanoes: Academic Press, p. 1035-1043.

Bernard, A., Demaiffe, D., Matielli, N., and Punongbayan, R.S., 1991, Anhydrite-bearing pumices from Mount Pinatubo: Further evidence for the existence of sulphur-rich silicic magmas: Nature, v. 354, p. 139-140.

Bonadonna, C., Ernst, G.G.J., and Sparks, R.S.J., 1998, Thickness variations and volume estimates of tephra fall deposits; the importance of particle Reynolds number: Journal of Volcanology and Geothermal Research, v. 81, p. 173-187.

Carey, S., and Sparks, R.S.J., 1986, Quantitative models of the fallout and dispersal of tephra from volcanic eruption columns: Bulletin of Volcanology, v. 48, p. 109-125.

Casadevall, T.J., Delos Reyes, P.J., and Schneider, D.J., 1996, The 1991 Pinatubo eruptions and their effects on aircraft operations, *in* Newhall, C.G. and Punongbayan, R.S., eds., Fire and Mud, Eruptions and Lahars of Mount Pinatubo, Philippines: PHIVOLCS and University of Washington, p. 1071-1088.

Hofmann, D.J., and Solomon, S., 1989, Ozone destruction through heterogeneous chemistry following the eruption of El Chichón: Journal of Geophysical Research, v. 94, p. 5029-5041.

Holasek, R.E., Self, S., and Woods, A.W., 1996, Satellite observations and interpretation of the 1991 Mount Pinatubo eruption plumes: Journal of Geophysical Research, v.101, p. 27635-27655.

Koyaguchi, T., and Tokuno, M., 1993, Origin of the giant eruption cloud of Pinatubo, June 15, 1991: Journal of Volcanology and Geothermal Research, v. 55, p. 85-96.

Krumbein, W.C., 1936, Application of logarithmic moments to size frequency distributions of sediments, Journal of Sedimentary Petrology, v. 6, p. 35-47.

Kuntz, M.A., Rowley, P.D., Macleod, N.S., Reynolds, R.L., McBroome, L.A., Kaplan, A.M., and Lidke, D.J., 1981, Petrography and particle-size distribution of pyroclastic-flow, ash-cloud and surge deposits, *in* Lipman, L.P. and Mullineau, D.R., eds., The 1980 Eruptions of Mount St. Helens, Washington: USGS, p. 525-539.

Lirer, L., and Vinci, A., 1991, Grain-size distributions of pyroclastic deposits: Sedimentology, v. 38, p. 1075-1083.

Mankin, W.G., Coffey, M.T., and Goldman, A., 1992, Airborne observations of SO_2, HCl, and O_3 in the stratospheric plume of the Pinatubo volcano in July 1991: Geophysical Research Letter, v. 19, p. 179-182.

McManus, D.A., 1963, A criticism of a certain usage of the phi-notation: Journal of Sedimentary Petrology, v. 33, p. 670-674.

Mercado, R.A., Lacsamana, J.B.T., and Pineda, G.L., 1996, Socioeconomic impacts of the Mount Pinatubo eruption, *in* Newhall, C.G. and Punongbayan, R.S., eds., Fire and Mud, Eruptions and Lahars of Mount Pinatubo, Philippines: PHIVOLCS and University of Washington, p. 1063-1069.

Murai, I., 1961, A study of the textural characteristics of pyroclastic flow deposits in Japan: Bulletin of the Earthquake Research Institute, v. 39, p. 133-248.

Norton, M.R. and Gunter, M.E., 1999, Relationships between respiratory diseases and quartz-rich dust in Idaho, U.S.A.: American Mineralogist, v. 84, p. 1009-1019.

Óskarsson, N., 1980, The interaction between volcanic gases and tephra: Fluorine adhering to tephra of the 1970 Hekla eruption: Journal of Volcanology and Geothermal Research, v. 8, p. 251-266.

Paladio-Melosantos, M.L.O., Solidum, R.U., Scott, W.E., Quiambao, R.B., Umbal, J.V., Rodolfo, K.S., Tubianosa, B.S., Delos Reyes, P.J.; Alonso, R.A.; and Ruelo, H.B., 1996, Tephra falls of the 1991 eruptions of Mount Pinatubo, *in* Newhall, C.G. and Punongbayan, R.S., eds., Fire and Mud, Eruptions and Lahars of Mount Pinatubo, Philippines: PHIVOLCS and University of Washington, p. 513-535.

Rhodes, M., 1999, Introduction to Particle Technology: John Wiley & Sons, Chichester, 320 p.

Rose, W.I., Delene, D.J., Schneider, D.J., Bluth, G.J.S., Krueger, A.J., Sprod, I., McKee, C., Davies, H.L., and Ernst, G.G.J., 1995, Ice in the 1994 Rabaul eruption cloud: implications for volcanic hazard and atmospheric effects: Nature, v. 375, p. 477-479.

Rosi, M., Paladio-Melosantos, M.L., Di Muro, A., Leoni, R., and Bascolcol, T., 2001, Fall vs flow activity during the 1991 climactic eruption of Pinatubo volcano (Philippines): Bulletin of Volcanology, v. 62, p. 549-566.

Scott, W.E., Hoblitt, R.P., Torres, R.C., Self, S., Martinez, M.M.L., and Timoteo, N.Jr., 1996, Pyroclastic flows of the June 15, 1991, climactic eruption of Mount Pinatubo, *in* Newhall, C.G. and Punongbayan, R.S., eds., Fire and Mud, Eruptions and Lahars of Mount Pinatubo, Philippines: PHIVOLCS and University of Washington, p. 545-570.

Sigurdson, H., and Carey, S., 1989, Plinian and co-ignimbrite tephra fall from the 1815 eruption of Tambora volcano: Bulletin of Volcanology, v. 51, p. 243-270.

Sparks, R.S.J., Wilson, L., and Sigurdson, H., 1981, The pyroclastic deposits of the 1875 eruption of Askja, Iceland: Royal Society of London Philosophical Transaction Series, v. A299, p. 241-273.

Sparks, R.S.J., Bursik, M.I., Carey, S.N., Gilbert, J.G., Glaze, L.S., Sigurdson, H., and Woods, A.W., 1997, Volcanic Plumes: John Wiley & Sons, Chichester, 574 p.

Smith, D.K., 1997, Evaluation of the detectability and the quantification of respirable crystalline silica by X-ray powder diffraction methods: Powder Diffraction, v. 12, p. 200-227.
Tabazadeh, A., and Turco, R.P., 1993, Stratospheric chlorine injection by volcanic eruptions: HCl scavenging and implications for ozone: Science, v. 260, p. 1082-1086.
Volon, C., 1997, Problématique des panaches d'éruptions volcaniques injectés dans l'atmosphère: détection et modélisation au moyen de l'image satellitaire, [PhD thesis]: Brussels, Belgium, Department of Earth and environmental Science, Université Libre de Bruxelles, 172 p.
Wiesner, M.G., Wang Y., and Zheng, L., 1995, Fallout of volcanic ash to the deep South China Sea induced by the 1991 eruption of Mount Pinatubo: Geology, v. 23, p. 885-888.
Woods, A.W., 1988, The fluid dynamics and thermodynamics of eruption columns: Bulletin of Volcanology, v. 50, p. 169-193.

GSA Data Repository item 2002071 is available on request from Document Secretary, GSA, P.O. Box 9140, Boulder, CO 80301-9140, USA, editing@geosociety.org or at http://www.geosociety.org/pubs/ft2002.html.

Acknowledgements

We are indebted to L. Lirer, A. Vinci, and M.L.O. Paladio-Melosantos for sharing raw data. We thank W.I. Rose, S. Carey, G.P.L. Walker, R.S.J. Sparks, W. Scott and an anonymous reviewer for helpful comments on this manuscript; P. Baxter, R.A. Mercado, L. Yoshisaki, and C. Newhall for sharing medical information. The 1991 field work of Bernard in the Philippines was funded by the Fond National de la Recherche Scientifique. Dartevelle thanks McGill University, and the Université Libre de Bruxelles for their administrative and financial supports. Stix acknowledges financial support from NSERC and FCAR. Ernst thanks La Fundation Belge de la Vocation and Nuffield Foundation.

Figure and Annex captions

Figure 1

Two mechanisms can generate stratospheric ash cloud: A represents Plinian column, and B is coignimbrite ash cloud formed from extensive pyroclastic-flows resulting from fountain collapse. When pyroclastic-flows become buoyant and loft, they can generate stratospheric coignimbrite cloud. Plinian column tends to encompass very heterogeneous materials of various sizes, whereas coignimbrite plume is made of only small grains.

Figure 2

Variation of grain-size parameters with distance (km) from vent for Plinian Askja (closed symbols) and for coignimbrite Mount Pinatubo deposits (opened symbols). For a given deposit, circles represent first moment (arithmetic metric mean, m), triangles standard deviation (metric sorting, mm), and squares bulk specific surface area (SSA, m^{-1}).

Figure 3

Grain-size ratios for 600 samples. Vertical axis is specific surface area over mean (SSA/mean, m^{-2}), and horizontal axis is mean over sorting (mean/sorting, dimensionless). Closed diamonds are for fall deposits from Plinian, subPlinian or Strombolian clouds. Opened triangles represent pyroclastic-flow deposits, and opened squares represent pyroclastic-surge deposits. Black line, drawn from a best visual fit, indicates boundary between pure Plinian fall domain (right side) and pyroclastic-flow and -surge domains (left side). As indicated, coignimbrite fall deposits from Mount St. Helens (closed squares), Tambora (closed triangle), and Pinatubo (circles) eruptions plot in flow-surge domain. Distance on the right side only refers to Plinian deposits, and represents actual distance between the deposits and the volcano.

Annex 1

Sampling techniques and locations around Mount Pinatubo.

Annex 2

Description of the various grainsize parameters in the metric scale used in this chapter. P is the weight distribution function (wt.%), d is the grain diameter (m), and Λ is a shape factor (6 for spheres and cubes, dimensionless). [this was not part of the original publication in Geology].

Annex 3

Amount of PM_{10} (wt.%) in the fallout deposits vs. distance from source for Askja and for Mt. Pinatubo eruptions. Within the first 140 km, there is no PM_{10} in the Askja plinian fallout deposits, which contrast greatly with Mt. Pinatubo coignimbrite fallouts. [this was not part of the original publication in Geology].

Chapter 1 - Figure 1

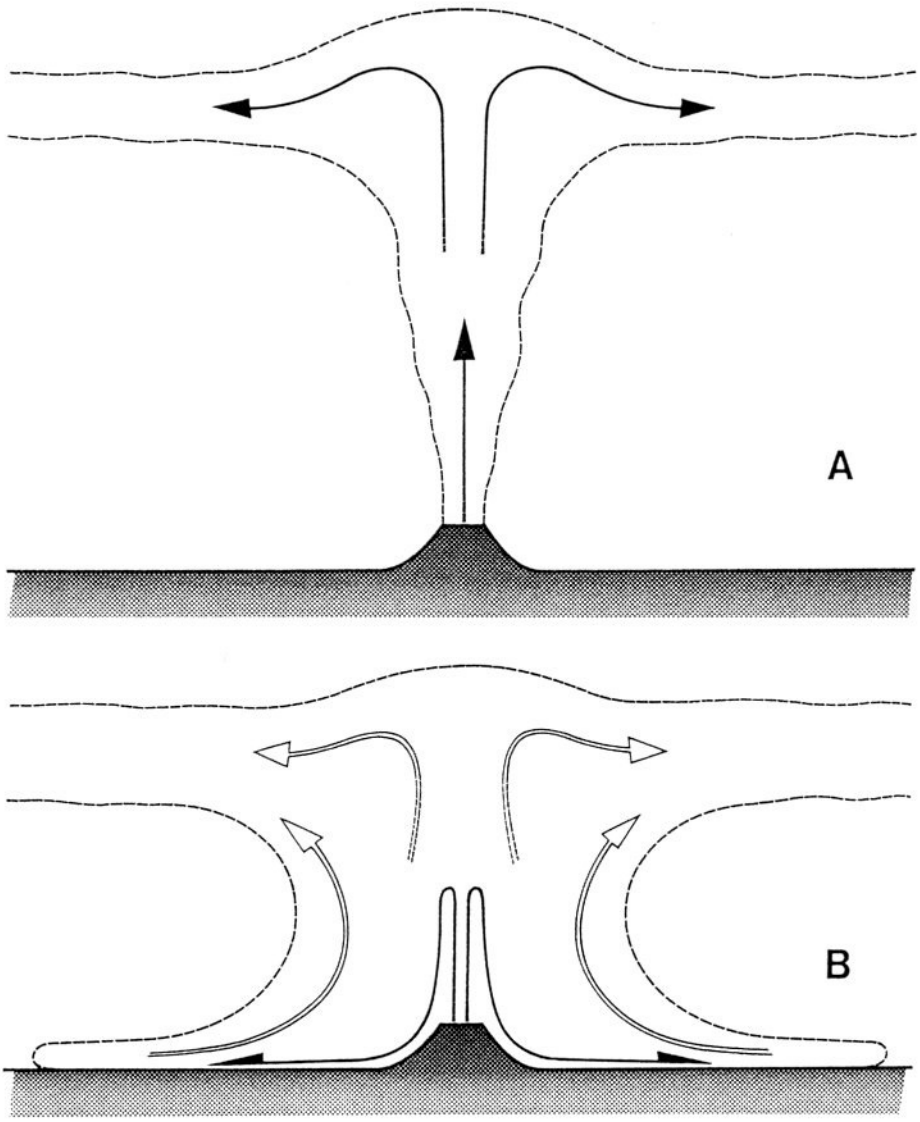

Chapter 1 - Figure 2

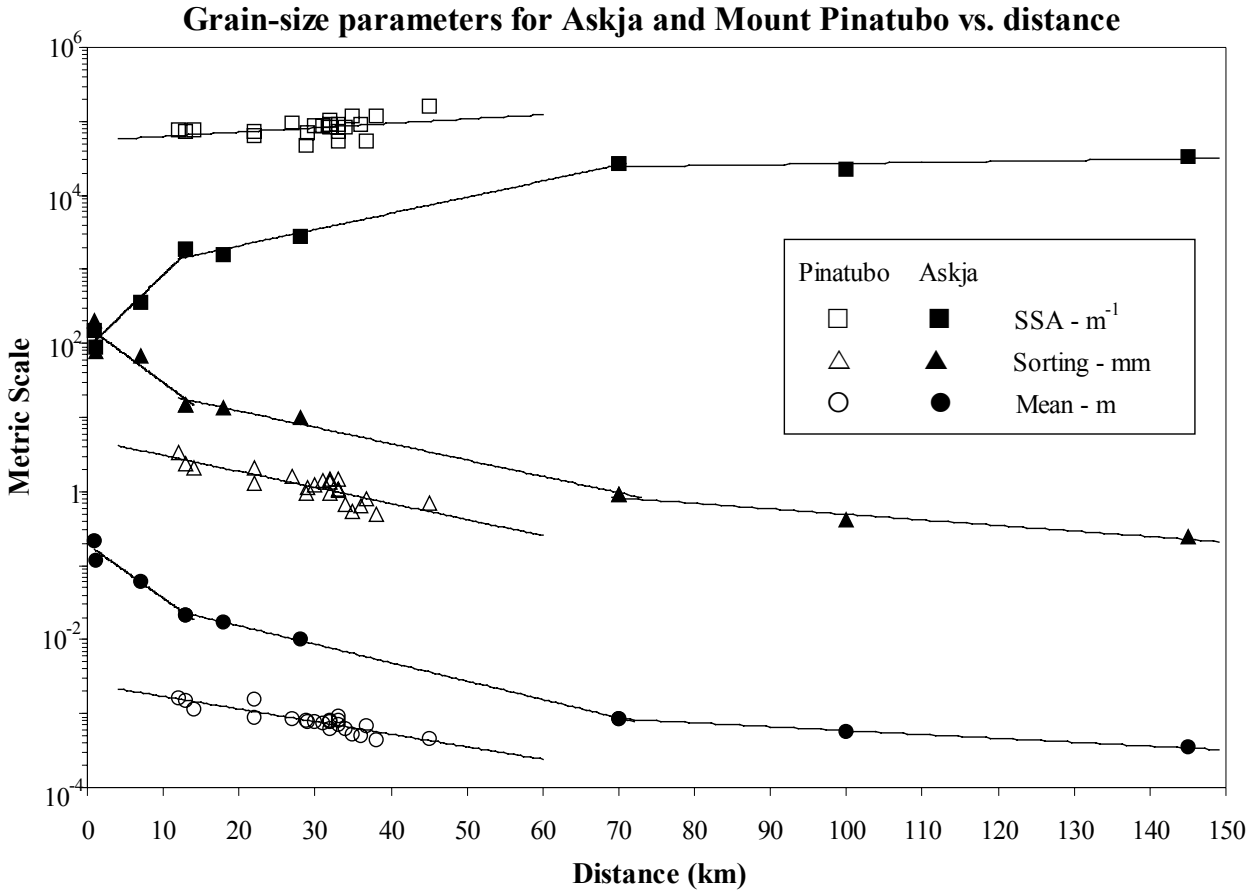

Chapter 1 - Figure 3

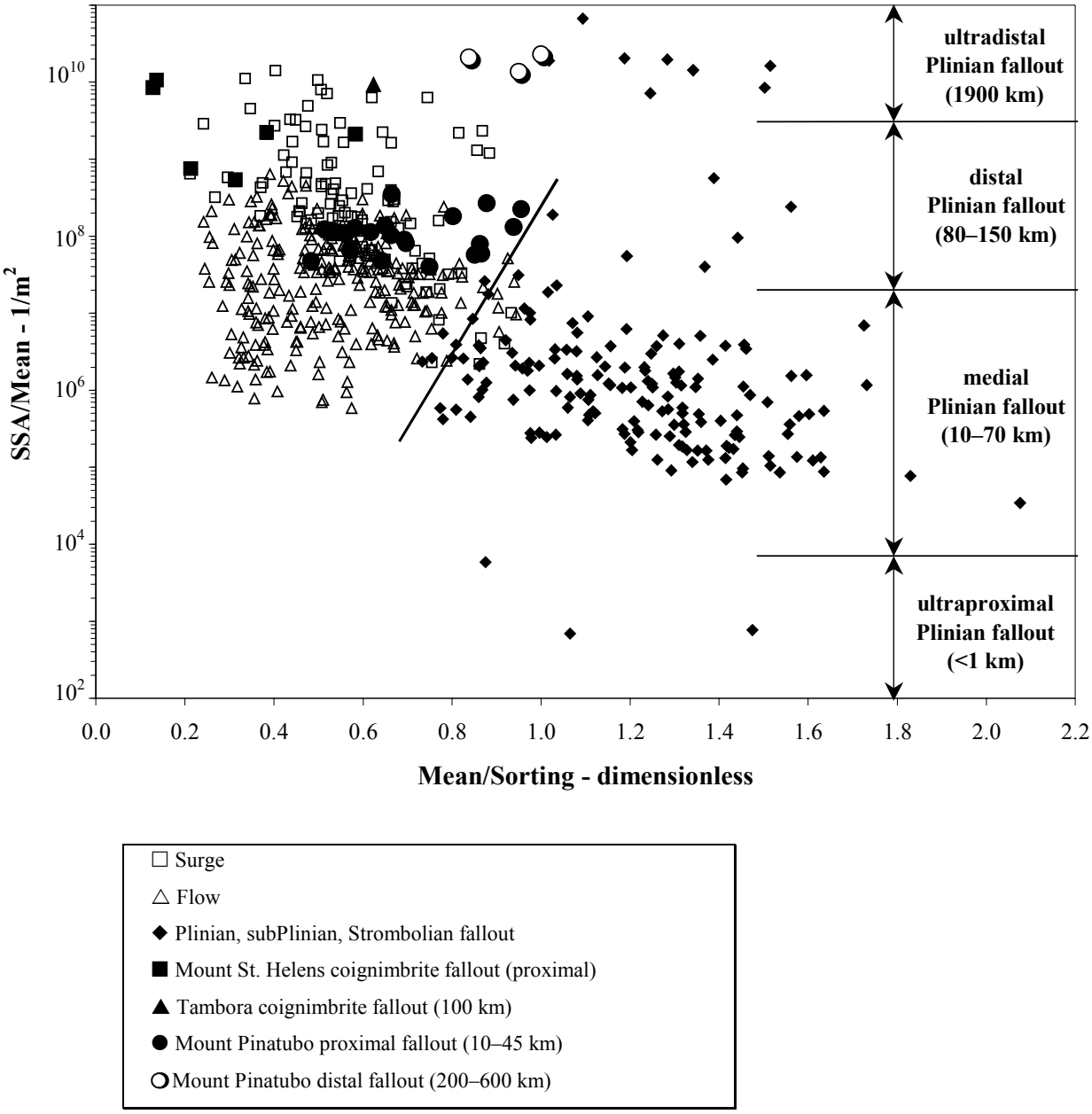

Chapter 1 - Annex 1: GEOLOGY Data Repository – item 2002071

All the data used in this manuscript are from our sampling campaign carried out early in September, 1991. We took drillcore samples with PVC tubes all around the volcano in order to sample the entire stratigraphy. The sampling distance range was from about 11 km to 45 km away from the volcano (see Figure DR1 for the exact locations). Since samples have been collected just after the climactic eruption, the layer C has not yet been modified, cut-off, or secondarily reworked in any ways. In addition, all the layer C were still layered between layer B (bottom, pre-climactic eruption deposits) and layer D (top, post-climactic eruption deposits) (Paladio-Melosantos et al., 1996), which confirms we had the complete stratigraphic section of layer C.

We used wet sieving techniques (ASTM screen sieve with 1Φ intervals and 1/2Φ for the finer sizes) from 16 mm to 44.19 μm (from -4 to 4.5 Φ). This wet sieving method was chosen to reduce abrasion. Because the finest fraction (less than 44.19 μm) was non-negligible, we also used a laser-diffraction analyzer (Cilas model 226). The laser diffraction size analysis is based on the principle that particles of a given size diffract through a given angle. This angle increases with decreasing size. If we assume that all the grains have the same density, the analyzer gives a mass frequency function. This assumption is mostly true since most grains of this size are volcanic glass. With this laser analyzer, the class intervals were 1/2Φ wide and range from 4Φ (62.5 μm) to 10Φ (0.98 μm).

We also analyzed ultradistal fallout samples from the Plinian Askja eruption (collected in Sweden at ~1900 km from source) with the same laser technique. No-sieving was required for those fine ash samples from this Askja eruption.

It is worth noting that many grain-size analysis found in the past literature disregard and neglect the very fine ash. Not taking into account the fines creates a strong bias in the statistical analysis. Most of the conclusions of this paper would not have been found without the accurate knowledge of the full range of the grain size distributions. Therefore, most of the 600 grain-size data in our database have been carefully chosen because of their high analytical quality.

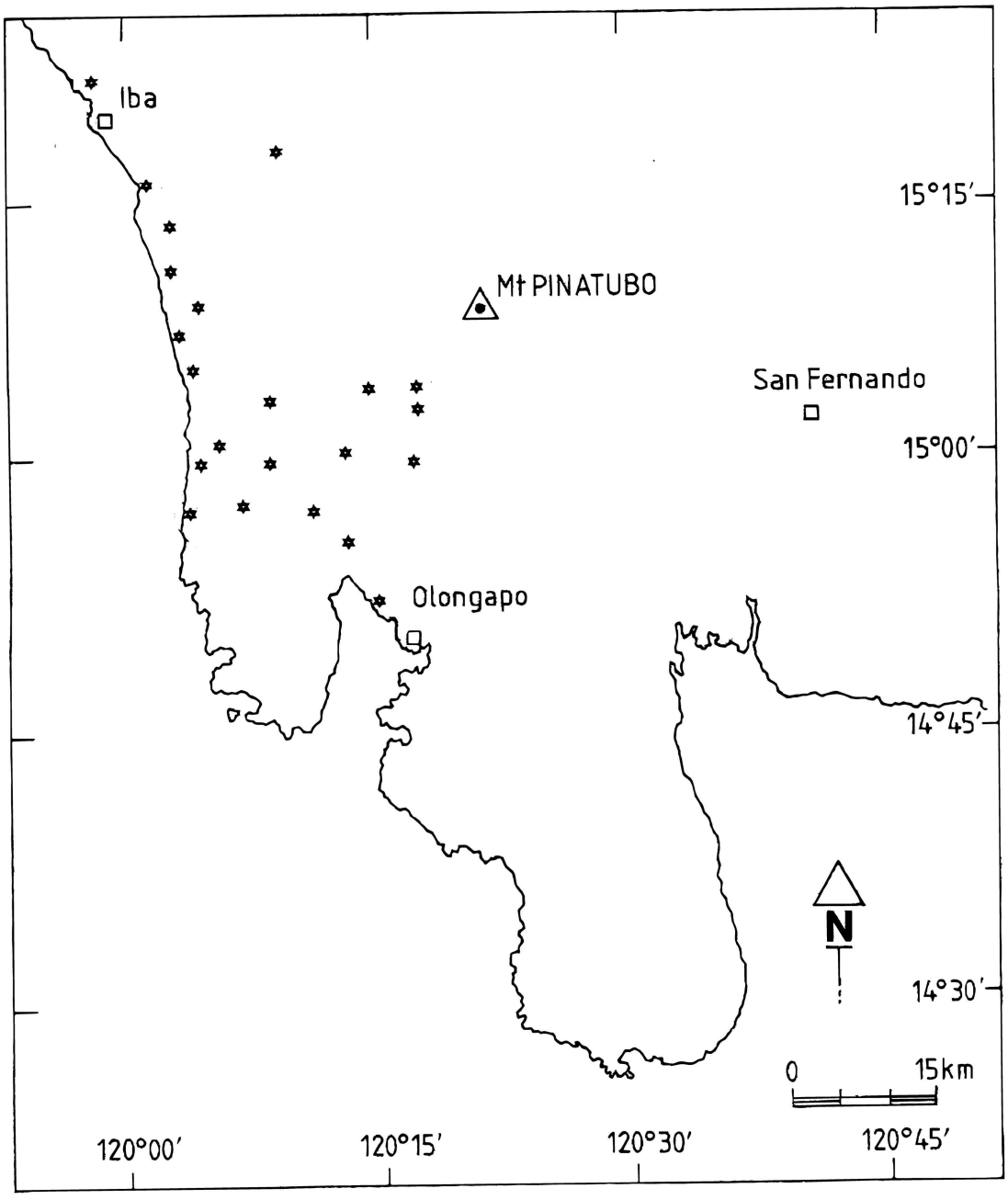

Figure DR1. Location (represented by a star) of all our samples collected around Mount Pinatubo volcano and used in this manuscript.

Chapter 1 - Annex 2: Definition of the grainsize parameters

Definition		Definition - Interpretation
1st statistical moment, $\overline{m}$	$\overline{m} = \frac{\int_0^1 d\, dP}{\int_0^1 dP}$	This represents the metric arithmetic mean of the weight distribution function of the pyroclastic deposit
Standard deviation, $\overline{s}$	$\overline{s}^2 = \frac{\int_0^1 (d - \overline{m})^2\, dP}{\int_0^1 dP}$	This represents the metric granulometric sorting of the deposit.
Bulk Specific Surface Area, SSA	$SSA = \Lambda \frac{\int_0^1 \frac{1}{d} dP}{\int_0^1 dP}$	SSA represents the bulk surface area of a set of grains relative to their total volume. It is proportional to the inverse of the harmonic mean of the weight grain-size distribution function. It is mathematically equivalent to state that SSA is proportional to the inverse of the Sauter mean diameter of the number grainsize distribution function.
Grain-size ratios	$\frac{Mean}{Sorting} = \frac{\overline{m}}{\overline{s}}$	for a separation between pure fallout deposits from plinian, subplinian, strombolian clouds and gravity controlled deposits. For a given deposit, this ratio remains roughly constant with distance.
	$\frac{SSA}{Mean} = \frac{SSA}{\overline{m}}$	for a better separation between flow and surge deposits. It might also be used to distinguish different types of flows (block-and-ash flow, flow, nuée ardente, etc).

Chapter 1 - Annex 3: PM_{10} variation vs. distance from source

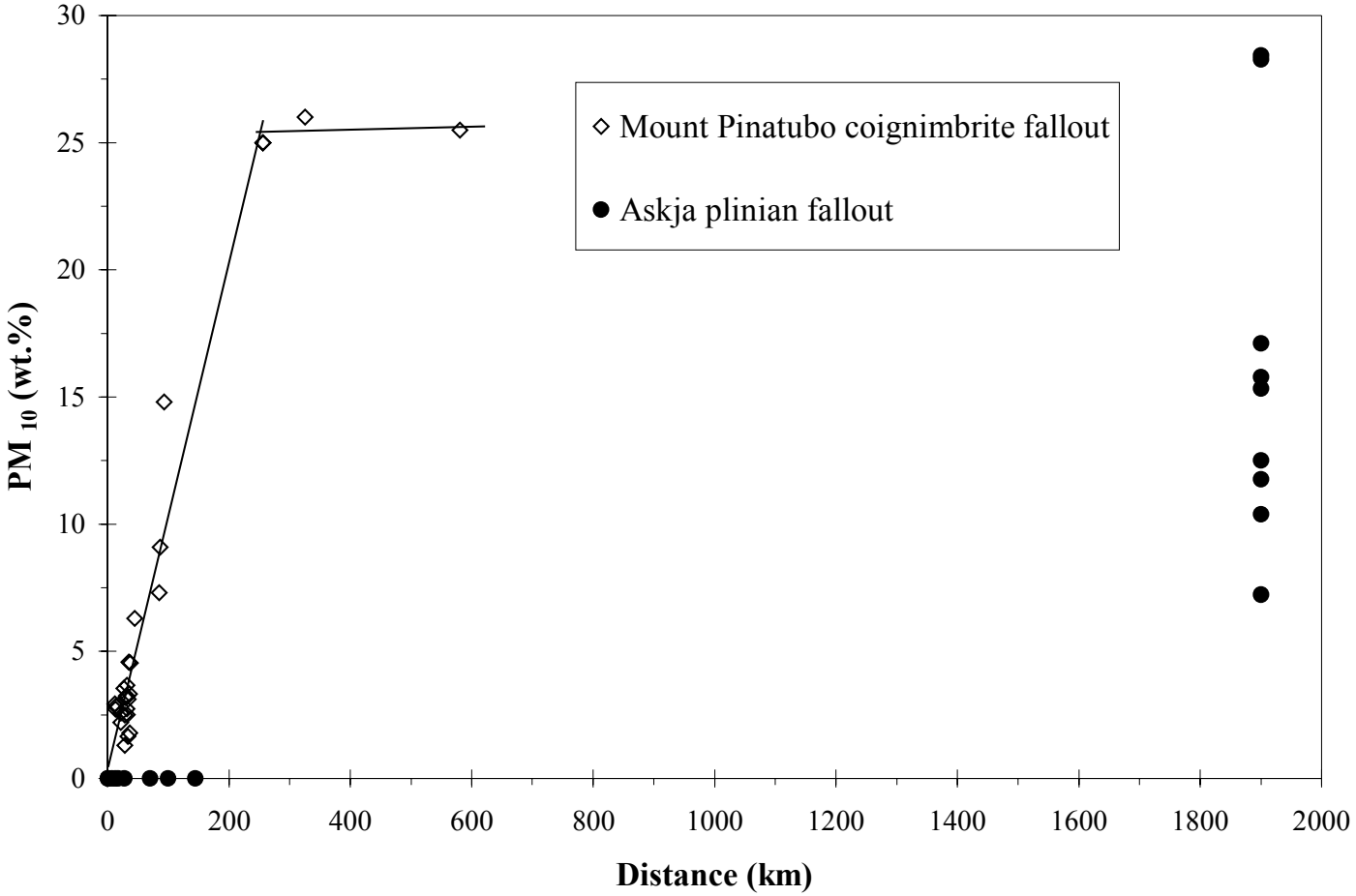

Chapter 2.

Numerical Modeling of Geophysical Granular Flows: Part I. A Review of Multiphase Flow Models and Granular Rheologies

Keywords: Granular flow, multiphase flow, granular gravity currents, granular rheology, kinetic, collisional, frictional, plastic, granular-temperature, critical state, contractancy, dilatancy, plastic potential, yield locus.

"*As far as the laws of mathematics refer to reality they are not certain; and as far they are certain, they do not refer to reality.*"

Albert Einstein (1879-1955).

Abstract

Geophysical granular materials display a wide variety of behaviors and features, which are systematically reviewed in this manuscript. Typically, granular flows (i) are multiphase flows, (ii) are very dissipative over many different scales, (iii) display a wide range of grain concentrations, and (iv), as a final result of these previous features, display complex nonlinear, non-uniform, and unsteady rheologies. Therefore the objectives of this manuscript are twofold, (i) setting up a hydrodynamic model which acknowledges the multiphase nature of granular flows and multiphase turbulence, and (ii) defining a comprehensive rheological model which accounts for all the different forms of viscous dissipations within granular flows *at any concentration*. Hence three important regimes within granular flows must be acknowledged: kinetic (pure free flights of grain), kinetic-collisional and frictional. The momentum and energy transfer will be different according to the granular regimes; i.e., strain-rate dependent in the kinetic and kinetic-collisional cases and strain-rate independent in the frictional case. A "universal" granular rheological model requires a comprehensive unified stress tensor able to adequately describe viscous stress within the flow for any of these regimes, and without imposing *a priori* what regime will dominate over the others. The kinetic-collisional viscous regime is defined from the Boltzmann's kinetic theory of dense gas modified to account for inelastic collisions between grains and the presence of the gas phase. The frictional viscous regime is defined from the plastic potential and the critical state theories which account for compressibility of granular matter (e.g., dilatancy, consolidation and critical state). Yield functions are represented by a family of nested ellipsoids in the principal stress space, each one corresponding to an unique granular concentration. This compressible plastic model allows to simulate depositional processes. In the companion paper [*Dartevelle et al., 2003*], we will introduce an unified computer code, (G)MFIX, which accounts for all the granular regimes and rheology and present typical simulations of diluted (e.g., plinian clouds) and concentrated geophysical granular flows (i.e., pyroclastic-flows and -surges). Throughout this manuscript, we will also discuss the fundamental assumptions behind this model as well as its weakness and strength.

1. Introduction

Granular flow can be defined as *a collection of discrete, solid particles dispersed in a moving interstitial fluid*; hence its owns all the common properties of multiphase flow. Such flows have been extensively studied for many decades in the field of physics, chemical engineering, fluid mechanics, computational fluid dynamics. They are ubiquitous and can be observed anywhere, e.g., in nuclear, chemical, petroleum, metallurgical industries, in handling and retrieval of foods processes, and in pharmaceuticals. In geophysics, turbidity currents, landslides, dry snow avalanches, pyroclastic-flows are a few common examples of concentrated granular flows, while plinian clouds, coignimbrite ash clouds, and pyroclastic-surges represent the diluted end-members of those geophysical granular flows. The cost associated with granular flows is enormous. In oil and chemical industries more than $61 billion is linked to particle technology [*Ennis et al., 1994*] as one-half of the products and at least three-quarter of the raw materials are in a granular form [*Nedderman, 1992*]. Each year, only in North America, one thousand silos, bins, hoppers fail and, even worse, sometime collapse [*Knowlton et al., 1994*]. Needless to say that the human and financial cost associated to geophysical granular flows such as pyroclastic phenomena, landslides and snow avalanches is inestimable. For instance, it is surmised that, since the 19th century, volcanic eruptions have caused the direct death of more than 150,000 people (only pyroclastic-flows and -surges, this does not include lahars and tsunamis). In addition, the destructive effects of pyroclastic phenomena can continue many decades after the eruption itself [*Rampino, 1991; Robock, 2000; Dartevelle et al*., 2002]. Despite of their ubiquity and seeming simplicity, granular flows and materials are still poorly understood as they behave differently from the other familiar state of matter: they do not solely behave as a solid, liquid or gas state, and should rather be considered as a additional state of matter in its own right [*Jaeger et al., 1996*].

Granular flows in both geophysics and in small-scale industrial environment have some remarkable features that can be summarized as follow. (1) Depending on the loading conditions, granular flows are highly dissipative because of static frictions, the inelasticity of collisions between grains [*Jaeger et al., 1996; Brey et al., 1999*], and/or the multiphase turbulence (for diluted flows) [*Besnard and Harlow, 1988; Violet et al., 1992; Kashiwa and VanderHeyden, 2000; Lakehal, 2002*]. Hence the assumptions that grains are in dynamic equilibrium with the carrier phase (i.e., pseudo-gas) or inviscid are questionable [e.g., *Murray, 1967; Grace, 1970; Wilson and Head, 1981; Didwania and Homsy, 1981; Freundt and Bursik, 1998; Calder et al,*

2000]. (2) Granular flows can display a wide range of grain concentrations [*Syamlal, 1987*]. This has been subject to debate between volcanologists for many decades as pyroclastic-flows can be seen as diluted and expanded [*Valentine, 1987; Braney and Kokelaar, 1992; Freundt, 1999*], poorly expanded, except perhaps at the head [*Sparks, 1976; Wilson and Walker, 1985*], or behaving according to the frictional Mohr-Coulomb law (i.e., highly concentrated) [*Iverson and Denlinger, 2001; Denlinger and Iverson, 2001*]. Clearly, modeling granular flows should account for all possible concentrations without imposing *a priori* a grain concentration span within the flow (thereof an *a priori* rheology). (3) As a results of the previous properties, granular flows display complex nonlinear, unsteady, and non-uniform rheological behaviors [*Lun et al., 1984; Schaeffer, 1987; Syamlal, 1987; Gray and Stiles, 1988; Boyle and Massoudi, 1989; Ding and Gidaspow, 1990; Nieuwland et al., 1996; Dartevelle, 2003; Dartevelle et al., 2003*].

Having these properties in mind, the objectives of this manuscript are twofold. First, we develop a hydrodynamic model which specifically recognizes the multiphase nature of geophysical-atmospherical granular flows. Second, we develop an "universal" rheological model for the granular phase which can deal with the whole spectrum of grain concentrations, hence grain behaviors (free flights, binary collisions, frictions). The rheological model specifically deals with the nonlinear, non-uniform, unsteady nature of granular matter in accounting for the various forms of dissipations taking place within fluidized and frictional granular flows. As illustrate in the companion paper, this model allows to simulate granular flows from diluted and fluidized dusty surge clouds to idle high-concentration granular deposits [*Dartevelle et al., 2003*].

This manuscript is organized as follows. First (§2), we briefly introduce the hydrodynamic model. Next (§3), we introduce the general concepts behind granular rheologies and demonstrate the constitutive equations of the kinetic-collisional (§3.2) and plastic-frictional (§3.3) models. Then (§4), we develop the Large Eddy Simulation (LES) closures used in our model to approach turbulence effects. In the companion paper [*Dartevelle et al., 2003*], we introduce the numerical methodology used in (G)MFIX computer codes, and discuss the plinian cloud, pyroclastic-flow and -surge numerical simulations.

All the symbols, constants, operator, tensors, invariants, SI units, and acronyms in this manuscript and in the companion paper are thoroughly defined in Appendix 1 and Appendix 2. The sign convention for stress is such that it follows the same convention as Fick and Fourier laws [*Bird et al., 1977*]. In other words, viscous stress is positive in the direction of decreasing velocities. Hence compressive stress, compressive strain, and their rates are taken positive.

2. Hydrodynamic model

Since the system is made up of a large number of particles, it is impractical to solve the motion of each individual particle; hence we have chosen the **I**mplicit **M**ulti**F**ield formalism (IMF) which treats all phases in the system as interpenetrating continua. Each point variable (mass, velocity, temperature, pressure, …) is volume-averaged over a region that is large compared with the particle spacing but much smaller than the overall flow domain [*Anderson and Jackson, 1967; Syamlal et al, 1993*]. Hence we do not resolve the detailed small-scale flow fluctuations of each point variable but rather we smooth out all the fluctuations in replacing point variables by local mean variables (see *Anderson and Jackson* [*1967*] for the averaging techniques used here). The fact we have averaged out some details is not worrisome as we are mostly concerned in the bulk flow behavior and as we rather want to know how the system works as a whole as opposed to wanting to know the exact history of a particular grain within the flow. However, in the averaging process, we have lost some information that may affect the bulk flow behavior and therefore it is necessary to supply specific constitutive relations (e.g., viscous stress, interfacial heat and momentum transfers, heat conduction, so forth) [*Drew, 1983; Syamlal et al, 1993; Crowe et al., 1996*].

The equations of the hydrodynamic model (Table 1) are written in terms of the local volume averaged variable for each phase, where $\hat{\rho}$, **u**, t and y pertain for macroscopic density, velocity vector, time, and mass fraction of gas components. The indices 's' and 'g' are for the solid and gas phase, while 'a' and 'w' pertain for dry-air and water vapor (see Appendix 1). We assume only one grainsize and two species components within the gas phase. Because all phases form interpenetrating continua, they can be present at the same time in the same Control Volume, CV [*Harlow and Amsden, 1975*]. Hence, we must distinguish the microscopic density (actual microscopic mass per unit of volume) of a particular material, ρ (*e.g.*, 1500kg/m^3 for pumice) from the macroscopic bulk density, $\hat{\rho} = \varepsilon \rho$, where ε is the volumetric fraction of the phase under consideration. If grains are assumed spherical and smooth, we have $\varepsilon_s = \frac{\pi}{6} n d^3$ and $\hat{\rho} = n m$, where 'd' is the diameter of the grain, 'n' is the number of grains in a given volume, and 'm' the mass of the grains [*Gidaspow, 1994*]. The maximum solid volumetric concentration in a randomly packed structure of equal-size spheres is ${}^{max}\varepsilon_s \sim 0.64$ [e.g., *Lun et al., 1984*]. Continuity implies within a given CV for all phases that $\varepsilon_s+\varepsilon_g=1$ and for all gas species that $y_a+y_w=1$. The gas phase is modeled as an ideal gas:

$$\rho_g = \frac{P_g}{\tilde{R}\ T_g} \tag{1}$$

where P_g is the gas pressure, T_g the gas temperature and $\tilde{R}$ is the ratio of the universal gas constant (R) and the molar mass of a gas mixture:

$$\tilde{R} = R\left(\frac{y_a}{M_a} + \frac{y_w}{M_w}\right) \tag{2}$$

where M_a and M_w are the molar mass of dry air and water vapor respectively.

In Table 1, we have assumed that there is no phase change, no chemical reaction and grains are not fractured or do not aggregate. Therefore, Eq.(T1.1) to Eq.(T1.4) simply state that net mass change with time per unit of volume (left-hand side, LHS) is equal to the net rate of convective mass flux (right-hand side, RHS). The continuity equations and the treatment of the gas species pose no problem and are completely identical with *Dobran et al* [*1993*] and with PDAC2D codes [e.g., *Neri and Macedonio, 1996; Todesco et al., 2002*].

The momentum equations of the gas phase and solid phase in (G)MFIX have some subtle differences with PDAC2D and previous works in volcanology [e.g., *Valentine and Wohletz, 1989; Dobran, 1993*] with respect to (i) the viscous stress in the solid phase, (ii) the subgrid stress (SGS) and subgrid heat flux (SGH) due to turbulence in both phases, and (iii) the buoyancy. In the momentum equations, K, $\mathbf{g}$, $\boldsymbol{\tau}$ respectively pertain for interfacial drag, gravity vector, and viscous stress tensor. The first term on the LHS in Eq.(T1.5) and Eq.(T1.6) represents the net rate of momentum variation within the Control Volume and the second term is the net rate of momentum transferred by convection into CV. Therefore, the whole LHS term is the net change of momentum, *i.e*., the net acceleration due to the forces acting on CV and listed on the RHS: (i) drag force (friction between solid and gas) which is caused by the slip velocity between phases, (ii) pressure gradient, (iii) viscous forces, (iv) gravity force acting upon the gas phase in Eq.(T1.5), and net buoyancy acting upon the solid phase in Eq.(T1.6) (sum of the Archimedean force and the gravity force). The net buoyancy is acting only along the vertical direction, which is not the case in other Eulerian-Eulerian models [e.g., *Valentine and Wohletz, 1989; Dobran et al., 1993; Neri and Macedonio, 1996; Todesco et al., 2002*], which use a full 3D buoyancy model

(i.e., $-\varepsilon_s \nabla P_g$). We have opted for the Archimedean 1D (vertical) buoyancy because when ∇P_g appears in both solid and gas phase momentum equations, the system of equations has imaginary characteristics and the initial-value problem is ill-posed in that it tends to be elliptic instead of hyperbolic. A lack of hyperbolicity in a multiphase code made the code inherently and unconditionally unstable and subject to growing instabilities [e.g., *Lyczkowski, 1982; Sursock, 1982; Prosperetti, 1999*]. Although buoyancy is fundamentally a 3D phenomenon, we have not seen in all our simulations any differences in our results between those two buoyancy models, which suggests that buoyancy mostly dominates along the vertical direction in atmospherical applications. This result is consistent with previous observations in chemical engineering [e.g., *Gidaspow, 1994*]. The drag interfacial term used herein (K) is calculated from well-established semi-experimental correlations for multiphase flow models [e.g., *Kuipers et al., 1993; Gidapsow, 1994; Neri and Macedonio, 1996*] as seen in Table 2. For dilute suspensions (ε_g>0.8), a single sphere drag function modified by the presence of nearby spheres is used (Eq.(T2.1)), while at high solid concentration, *Ergun* [*1952*] equation is used (Eq.(T2.2)). The viscous stress tensor in both momentum equations includes turbulence closures (LES or kinetic-collisional models) and, in addition for the granular phase, includes a plastic model (for frictions). Those tensors will be examined in details in §3 and §4.

The LHS of the energy equations (Eq.(T1.7) and Eq.(T1.8)) represents the net rate of change of temperature within a CV and is equal to the sum of the work done by all the forces and the heat flux, i.e., in the RHS from left to right, (i) heat conduction within the phase following the Fourier law (heat loss or gain depending on the gradient of the temperature, $\mathbf{q}_{eff} = -\varepsilon k_{eff} \nabla T$ where k_{eff} is the sum of molecular and turbulent thermal conductivities), (ii) heat exchange between phases, and in the gas phase only (Eq.(T1.7)): (iii) work done by the drag force (frictional contacts between particles and gas), (iv) work associated to the change of volume of the gas phase because of the time-variations of ε_g and because of compression/expansion of the gas phase. The former term is important as it expresses the adiabatic heating/cooling of a plume moving within a stratified atmosphere, therefore allows to correctly calculate the temperature anomalies at the top of a plinian cloud (see companion paper *Dartevelle et al*. [*2003*]). Viscous dissipation in the gas phase and heat radiation are ignored since they are of minor importance relative to other heat sources (convection, conduction, interfacial heat exchange, volume change work) [*Valentine and Wohletz, 1989; Dobran et al., 1993; Neri and Macedonio, 1996*]. Notice that there is no viscous dissipation in the granular phase (Eq.(T1.8)), which is a key aspect from

kinetic granular theory. The viscous dissipation of the solid phase plays in favor of the granular-temperature and not necessarily and directly in favor of the thermal temperature of the solid phase. In the same vein, the work associated to the solid pressure variation (P_s) plays only onto the granular-temperature (therefore, onto the granular fluctuating energy). Eventually, because collisions are inelastic the granular-temperature will be dissipated into thermal heat [*Ogawa et al., 1980*] (see section §3.2). For sake of simplicity, the work associated with viscous dissipation of frictional forces between grains is neglected. In the energy equations, the specific heat at constant volume in the solid phase (Cv_s) is assumed to be constant (see Table 3) [*Valentine and Wohletz, 1989*], and, for the gas phase, Cv_g is calculated following the properties of ideal gas [*Wood, 1991*]:

$$Cv_g = Cp_g - \tilde{R} \tag{3}$$

where $Cp_g = y_a Cp_a + y_w Cp_w$; Cp_a and Cp_w are given in Eq.(T3.1) and Eq.(T3.2) following the unified calculation procedure of air properties by the European metrology laboratories [*Rasmusen, 1997*]. In Table 2, the interfacial heat transfer coefficient does not pose any particular problem as it is widely used by many multiphase models [e.g., *Kuipers et al, 1993; Neri and Macedonio, 1996*]. Eq.(T2.4) initially proposed by *Gunn* [*1978*] relates the Nusselt number (Nu), particle Reynolds number (Re), and the Prandtl number (^{mol}Pr) for all the porosity we are dealing in our simulations (e.g., $36 \leq \varepsilon_g \leq 100$ vol.%) and for Reynolds number up to 10^5.

In both Eq.(T1.7) and Eq.(T1.8), the proper specification of the thermal conductivities $k_{g,eff}$ and $k_{s,eff}$ poses a major difficulty within the IMF framework. Previous models [e.g., *Valentine and Wohletz, 1989; Dobran et al., 1993; Neri and Macedonio, 1996; Todesco et al., 2002*] assume that the conductivity coefficients are constant and unaffected by the presence of the other phase, which cannot be the case since both phases are interpenetrated in each other. Therefore, a given phase will "disrupt" the heat conduction within the other phase. In addition, turbulence will also greatly enhance the effective conductivity in a given phase. The molecular effective conductivities (i.e., "molecular" is used in a very loose way throughout this paper, it simply means "not due to turbulence" and applies for both granular and gas phases), $^{mol}k_{g,eff}$ and $^{mol}k_{s,eff}$, should be seen as effective transport properties which should depend on the phasic volumetric concentration (ε) and on the molecular conductivity of a phase alone ($^{mol}k_g$ and $^{mol}k_s$ in Table 3). The dependency formulations must be partially formulated with the recourse of experimental data

[e.g., *Zehner and Schlunder, 1970*]. The *Zehner and Schlunder* [*1970*]'s heat conductivity model was initially developed for estimating the effective radial thermal conductivity in packed granular bed, but it has been generalized to fluidized bed as well [e.g., *Kuipers et al, 1992*] as given in Table 4. For a complete demonstration of this model see, for instance, *Kuipers et al*. [*1992*] and Annex 4 in *Dartevelle* [*2003*]. From the effective (molecular) thermal conductivities for the gas phase (Eq.(T4.3)) and the solid phase (Eq.(T4.4)), it is obvious that whenever $\varepsilon_s \to 0$ (no particle, only gas phase), ${}^{mol}k_{s,eff} \to 0$ and ${}^{mol}k_{g,eff} \to {}^{mol}k_g$ and, for any ε_s, ${}^{mol}k_{s,eff} << {}^{mol}k_s$ as expected. Note that ω_k, A_k, given in Table 4, are for spherical particles only [*Zehner and Schlunder, 1970; Kuipers et al, 1992*]. The effect of turbulence in heat conductions will be examined in the LES section (§4).

3. Granular Rheologies

We now discuss the rheological model of the granular phase in order to set the constitutive relationships of the various viscous contributions in the solid momentum equations.

In chemical engineering, many early hydrodynamic models of fluidization [e.g., *Pigford and Baron, 1965; Anderson and Jackson, 1967; Homsy, 1983; Gidaspow and Ettahadieh, 1983*] have shown that model with zero granular viscosity leads to unrealistic growing disturbances within the fluidized bed [*Anderson and Jackson, 1967*; *Drew, 1983*] and were not able to match experimental data without using granular viscosity in the range of 13 to 19 Poise [*Didwania and Homsy, 1981*]. It is also well-known in multiphase computational fluid dynamics that two-phase flow inviscid equations are inherently ill-posed [*Drew, 1983*]. Viscous and eddy stress are fundamentally important. *Gidaspow and Ettehadieh* [*1983*] found it was also necessary to include a normal component of granular stress (*i.e*., a granular pressure) in order to prevent the particles from reaching unrealistic high concentration values. Many experimental attempts have been carried out to measure the granular viscosity of a fluidized medium. *Murray* [*1967*] and *Grace* [*1970*] have experimentally shown that the viscosity of a fluidized granular medium could be as high as 4 to 13 Poise, which is as high as the viscosity of glycerin [*Syamlal*, *1987*]. *Campbell and Wand* [*1991*] based on fluidization experiments have shown that the particle pressure is not a theoretical concept and can be measured. It changes according to the gas flow velocity within the granular bed, to the voidage and the particle sizes. Typically the particle pressure is maximum at zero superficial gas velocity as the entire bed is supported only across interparticle contact point, but with a fluidizing gas going through the bed, the particle pressure decreases to a minimum as progressively more and more of the bed is supported by fluid forces. *Campbell and Wand* [*1991*]

also note that a further increase in gas velocity causes the particle pressure to increase once again owing to the (chaotic) agitation of the granular bed around gas bubbles. Those experiments have been recently confirmed by even more sophisticated experimental measurements [*Gidaspow and Huilin, 1998*]. Of course, it may appear counter-intuitive that solid matter, as grains, can have a viscosity as any gas and can give rise to some forms of "thermodynamical" pressure. However, experimental data clearly show the existence of interparticle forces within a fluidized bed [*Davidson et al., 1977*]. For instance, electrical conductivity experiments indicate that particle actually come into contact and may even form bridges that conveys electric current across significant portions of the bed and, hence, interparticle forces must be considered [*Goldschmidt and Le Goff, 1963; Reed and Goldberger, 1966; Graham and Harvey, 1966; Jones and Wheelock, 1970*]. In addition, granular flows at high concentration (>50 vol.%) which are not fluidized anymore but rather purely frictional equally display nonlinear rheologies and, most importantly, are subject to important compressibility effects which must be included in the model [*Schaeffer, 1987; Pitman and Schaeffer, 1987; Gray and Stiles, 1988*]. Those plastic-frictional flows can also be characterized by frictional viscosities and normal isotropic pressure [*Pitman and Schaeffer, 1989*] which is also reported in volcanology: *Wilson and Head* [*1981*] measured viscosities in the range $\mathcal{O}(10)$ to $\mathcal{O}(10^4)$ Pa·s in the Mt. St. Helens newly deposited pyroclastic-flows.

3.1. Open statements

As shown in Figure 4, we must distinguish three granular behaviors depending on the grain volumetric concentration: (i) in the dilute part of the flow, grains randomly fluctuate and translate, this form of viscous dissipation and stress is named *kinetic*; (ii) at higher concentration, in addition to the previous dissipation form, grains can collide shortly, this gives rise to further dissipation and stress, named *collisional*, and (iii) at very high concentration (>50 vol.%), grains start to endure long, sliding and rubbing contacts, which gives rise to a *frictional* (or plastic) dissipation. In the fluidized part of the flow, the gas phase turbulence may enhance and/or inhibit the kinetic and collisional dissipation.

An *ad hoc* mathematical model requires a comprehensive unified stress tensor able to adequately describe stress within the flow for any of these regimes, and this without imposing *a priori* what regime will dominate over the others. The idea initially suggested by *Savage* [*1983*] and formulated by *Anderson and Jackson* [*1992*] is:

$$\mathbf{T}_s = P_s\,\mathbf{I} + \boldsymbol{\tau}_s = {}^{f}\mathbf{T} + {}^{k/c}\mathbf{T} \qquad (4)$$

where the total stress tensor of the solid phase is the sum of the kinetic, collisional and frictional tensors, the superscript "f" stands for frictional and "k/c" for kinetic-collisional. Hence the solid pressure, P_s, and the viscous stress, $\boldsymbol{\tau}_s$, must encompass all the contributions from kinetic, collisional, and frictional dissipations. The kinetic and collisional contributions will be defined from Boltzmann's statistical approach of dense gas kinetic theory [*Chapman and Cowling, 1970; Lun et al., 1984; Boyle and Massoudi, 1989; Gidaspow, 1994; Gombosi, 1994*], while the frictional contribution will be defined from the plastic-potential theory [*Hill, 1956; Jackson, 1983; Schaeffer, 1987; Pitman and Schaeffer, 1987; Gray and Stiles, 1988; Nedderman, 1992*]. Those two stress tensors have a deep difference in their nature: ${}^{k/c}\mathbf{T}$ is a rate-of-strain dependent stress tensor and ${}^{f}\mathbf{T}$ is a rate-of-strain independent stress tensor. ${}^{k/c}\mathbf{T}$ may be regarded as a pure viscous (dynamic) stress due to the momentum transfer during grain random motions and their collisions, which corresponds to the grain-inertia regime of *Bagnold* [*1954*] and is only important for "diluted", fluidized flows at high rate-of-strains. At very high concentrations and low rate-of-strain, collisions cannot be seen as instantaneous anymore, grains enjoy long and permanent contacts in rubbing, rolling on each other and only the frictional stress tensor, ${}^{f}\mathbf{T}$, is dominant. Overall, it is clear this complex rheological behavior is nonlinear (i.e., not Newtonian or Bingham) and, possibly, unsteady and non-uniform as well.

In the following, "viscosity" is a positive scalar variable defined by the ratio of viscous stress and rate-of-strain. If stress and rate-of-strain tensors are both traceless (i.e., deviatoric), the scalar is a shear viscosity; if both tensors are spherical, the scalar is a bulk viscosity. Within the kinetic-collisional-plastic rheological models, granular viscous stress is developed to reduce the rate-of-strain within the granular phase. However, unlike a "traditional" (Newtonian) view of viscosity (i.e., the higher the rate-of-strain, the higher the viscous stress where viscosity is held constant), granular viscosities (shear and bulk) are non-linear functions because they depend on the flow conditions (i.e., rate-of-strain, granular-temperature, solid concentrations, ...).

3.2. Kinetic and collisional stress

The physical principles have been defined for the first time by *Ogawa et al.* [*1980*] and are depicted in Figure 5. Grains are in a continuous and chaotic restlessness within the fluid [*Batchelor, 1988*]. The production of this granular random motion is done mostly through

viscous dissipation but the subtle interplay with the gas phase has also an important role since the slip between gas and solid is a source of this random motion [*Sangani et al, 1996; Koch and Sangani, 1999; Agrawal et al, 2001*]. Afterwards, both viscous damping of the gas phase and the inelastic nature of grain collisions will dissipate the granular fluctuating energy into conventional thermal heat. Those two previous effects make a granular medium fundamentally different than a gas medium (e.g., gas molecule collisions are perfectly elastic). Therefore, E_Θ represents a transient energy state in the dissipation process of fluidized granular materials. This random motion promotes particle collisions and migrations of grains, and therefore, promotes momentum transfer as it is the case for the gas phase [*Chapman and Cowling, 1970, Syamlal, 1987*].

Let us note that the actual instantaneous velocity of the particle is $\mathbf{c}_s$, while the mean bulk velocity is $\mathbf{u}_s$ (where $\mathbf{u}_s = \langle \mathbf{c}_s \rangle$ as in equations of Table 1), and $\mathbf{C}_s''$ is the fluctuating velocity due to this grain random motion with $\mathbf{c}_s = \mathbf{C}_s'' + \mathbf{u}_s$ [*Lun et al., 1984*], where the double prime stands for "fluctuating" or "turbulent". The concept of "granular-temperature" (Θ) and fluctuating energy (E_Θ) can be defined as:

$$\begin{cases} \Theta = \dfrac{1}{3}\left\langle \mathbf{C}_s'' \cdot \mathbf{C}_s'' \right\rangle \\ E_\Theta = \dfrac{1}{2}\left\langle \mathbf{C}_s'' \cdot \mathbf{C}_s'' \right\rangle = \dfrac{3}{2}\Theta \end{cases} \tag{5}$$

Θ and E_Θ quantify the magnitude of the random motion of the granular matter, and like the temperature of a gas, both are an average measure of the chaotic motion of particles within the flow [*Boyle and Massoudi, 1989*]. Care must be taken as the concept of "granular-temperature" applied to granular media can be a little bit misleading because (i) there is no thermometer for measuring it, (ii) the fluctuating energy per unit of mass is not converted into some temperature degree-unit (*e.g.*, degree Kelvin for conventional heat) as done in the gas phase through the Boltzmann constant [*Gidaspow, 1994*], and (iii) the definition of this "temperature" is done without the mass of the particle. Hence, if compared with the definition of the temperature of the gas phase [*Chapman and Cowling, 1970*] the ratio of the Boltzmann constant to the mass of the particles is set to unity following classical granular kinetic formulations [*Gidaspow, 1994*].

The development of kinetic-collisional theory for granular flow closely follows the Chapman-Enskog approach of dense gases [*Chapman and Cowling, 1970*], which must be modified for

accounting the inelasticity of collisions [*Lun et al., 1984; Boyle and Massoudi, 1989; Ding and Gidaspow, 1990; Gidaspow, 1994*] and gas phase effects (i.e., slip and drag) [*Sangani et al, 1996; Koch and Sangani, 1999; Agrawal et al, 2001*]. In the Chapman-Enskog theory, a quantity ϕ (*e.g.*, mass m, momentum m**c**, kinetic energy of the random motion $\frac{1}{2}mC_s''^2$) can be transported by two transport mechanisms (Figure 4). The first is the kinetic transport of ϕ during the free flight of grains between collisions, while the second is the collisional transfer of ϕ from one particle to another during binary collisions. Let us define in the phase-space $\mathbf{r}\mathbf{c}_s$, the velocity distribution function $f(\mathbf{r},\mathbf{c}_s,t)$ which is a function of position **r**, time t, and the instantaneous velocity $\mathbf{c}_s$ of a large collection of grains. Then, the infinitesimal number of grains in a volume d**r**, at **r** having velocities between $\mathbf{c}_s$ and $\mathbf{c}_s+d\mathbf{c}_s$ is $dn=f(\mathbf{r},\mathbf{c}_s,t)d\mathbf{r}d\mathbf{c}_s$ [*Gombosi, 1994*]. Hence the total number of particles per unit of volume at time t, n, is $n = \int f(\mathbf{r}, \mathbf{c}_s, t)\, d\mathbf{c}_s$ and the average of a quantity ϕ transported by a number n of particle is $\langle \phi \rangle = \frac{1}{n} \int \phi\, f(\mathbf{r}, \mathbf{c}_s, t)\, d\mathbf{c}_s$ (i.e., first moment of ϕ in the statistical sense). After a time interval dt, the infinitesimal number of particle that have moved from **r** to a new location at $\mathbf{r}+\mathbf{c}_s dt$ with velocities around $\mathbf{c}_s+\mathbf{F}dt$ will be $dn'=f(\mathbf{r}+\mathbf{c}_s dt,\mathbf{c}_s+\mathbf{F}dt,t+dt)d\mathbf{r}d\mathbf{c}_s$, where **F** is the sum of all the external forces (per unit of mass) acting on the particles (i.e., gravity and gas-particle drag) [*Ding and Gidaspow, 1990*]. If particles would not endure any collisions, scattering, and would not be removed or added into the stream of flowing particles, then their number must remain constant within that stream at any time, i.e., dn'=dn. However, collisions do occur. Then the number of particles can change within the stream during the interval dt. Let us denote the net rate of change per unit of time of the number of particles due to collisions, dn_{col}. We must then have $dn'-dn=dn_{col}$. If we expand this expression in a Taylor series about dt, and this for any arbitrary space volume (d**r**), velocities (d**c**) and time interval (dt), we have the so-called Boltzmann integro-differential equation [*Chapman and Cowling, 1970; Gidaspow, 1994; Gombosi, 1994*]:

$$\frac{\partial f}{\partial t} + \mathbf{c} \cdot \frac{\partial f}{\partial \mathbf{r}} + \mathbf{F} \cdot \frac{\partial f}{\partial \mathbf{c}} = \left(\frac{\partial f}{\partial t} \right)_{\text{collisional}} \tag{6}$$

This equation states that, at steady state, the rate of change of the velocity distribution function (1st term of LHS) is balanced by the collisional rate of change (RHS), the rate of change of $f(\mathbf{r},\mathbf{c}_s,t)$ due to particle motion (2nd term of LHS) and due to external forces acting on the particles

(3^{rd} term of LHS). The LHS represents the kinetic transport mechanism and the RHS is the collisional transport. In this paper, we will not detail all the mathematics from which Eq.(6) is developed into useful constitutive equations. The mathematical methodology can be found in *Lun et al*. [*1984*] from which our model is based; see also the comprehensive review in *Boyle and Massoudi* [*1989*], *Gidaspow* [*1994*], and for the derivations and integrations used, see *Jenkins and Savage* [*1983*] and chapter 16 (§16.41, §16.42, §16.8) of *Chapman and Cowling* [*1970*]. Herewith, we will rather explain the core assumptions made in order to develop the granular kinetic-collisional constitutive equations. These different assumptions can be listed as follow:

Assumption 1: all the particles in the system have the same diameter and the same density (i.e., one grainsize).

Assumption 2: the inelasticity of collisions is accounted through the coefficient of restitution 'e', which is the ratio of the relative velocity along the line-of-centers of the particles before and after collisions (see Figure 6) [*Jenkins and Savage, 1983*]:

$$\mathbf{k}\cdot\mathbf{c}'_{12} = -\,e\,(\mathbf{k}\cdot\mathbf{c}_{12}) \tag{7}$$

where the prime indicates after collision, $\mathbf{k}$ is a unit vector along the line of centers from particle 1 to particle 2, $\mathbf{c}_{12}=\mathbf{c}_{s,1}-\mathbf{c}_{s,2}$ is the relative velocity, and $0<e\leq 1$ (0, perfectly inelastic and 1, perfectly elastic). Eq.(7) indicates that the relative velocity in the direction of the line of centers just after collisions is less than the relative velocity just before collision and, after collision, is in the opposite direction. The coefficient 'e' parameterizes the loss of granular-temperature.

Assumption 3: solving Eq.(6) requires the knowledge of the pair-frequency distribution function ${}^2f(\mathbf{r}_1,\mathbf{r}_2,\mathbf{c}_{s,1},\mathbf{c}_{s,1},t)$ to estimates the probability of finding a pair of particles in the volume element $d\mathbf{r}_1 d\mathbf{r}_2$ centered on the points $\mathbf{r}_1$ and $\mathbf{r}_2$, and having their velocity within the range of $\mathbf{c}_1$ to $\mathbf{c}_1+d\mathbf{c}_1$ for particle 1, and $\mathbf{c}_2$ to $\mathbf{c}_2+d\mathbf{c}_2$ for particle 2; i.e., ${}^2f(\mathbf{r}_1,\mathbf{r}_2,\mathbf{c}_{s,1},\mathbf{c}_{s,2},t)d\mathbf{r}_1 d\mathbf{c}_{s,1} d\mathbf{r}_2 d\mathbf{c}_{s,2}$ [*Chapman and Cowling, 1970*]. Assuming that the molecular chaos assumption holds, i.e., the velocities of two grains just before they collide are uncorrelated (i.e., independent in the statistical sense), it is possible to write the pair distribution function as the product of two single particle velocity distribution function at time t, and at the collisional location $\mathbf{r}$ [*Chapman and Cowling, 1970; Boyle and Massoudi, 1989*]:

$${}^2f\left(\mathbf{c}_{s,1}, \mathbf{r}-{}^{d}\!/_{2}\ \mathbf{k}, \mathbf{c}_{s,2}, \mathbf{r}+{}^{d}\!/_{2}\ \mathbf{k}, t\right) = g_0\ f(\mathbf{c}_{s,1}, \mathbf{r}, t)\ \ f(\mathbf{c}_{s,2}, \mathbf{r}, t) \tag{8}$$

The exact location where collision occurs, $\mathbf{r}=\mathbf{r}_2-\frac{1}{2}d\,\mathbf{k}$, is half a diameter apart from the center of the particles (Figure 6). In Eq.(8), g_0 is the radial distribution function which describes the probability of finding two particles at that specific location [*Boyle and Massoudi, 1989*]. It also corrects the probability of a collision for the effects of the non-negligible volume occupied by the particles [*Nieuwland et al., 1996*] and therefore acts as a correcting factor when concentration is high enough to break the molecular chaos assumption. Numerous semi-empirical forms exist for the radial distribution function, we have chose the one from *Carnahan and Starling* [*1969*] because it gives excellent results for solid concentration up to 50 vol.% when compared with molecular dynamic data of *Alder and Wainwright* [*1960*]. For higher concentration, *Carnahan and Starling*'s g_0 [*1969*] is fairly inaccurate [*Ding and Gidaspow, 1990*] but at those high concentrations the contact between grains is mostly frictional and the molecular chaos assumption cannot hold anymore. For concentration larger than 50 vol.%, a plastic-frictional model is then needed (see §3.3). The *Carnahan and Starling* [*1969*]'s radial distribution function is:

$$g_0 = \frac{1}{\varepsilon_g} + \frac{3\varepsilon_s}{2\varepsilon_g^2} + \frac{\varepsilon_s^2}{2\varepsilon_g^3} = \frac{2-\varepsilon_s}{2\varepsilon_g^3} \tag{9}$$

Assumption 4: it concerns the exact nature of the velocity distribution for each particle. The Boltzmann's H-theorem states that without the action of any external forces, the distribution function tends to a Maxwellian function (i.e., Gaussian). The granular matter is said to be in the "Maxwellian state", i.e., a steady, uniform and isotropic state (this is the zeroth-order solution to the velocity distribution function):

$$f_0(\mathbf{r}, \mathbf{c}_s, t) = \frac{n}{(2\pi\,\Theta)^{3/2}} \quad \exp\left[\frac{(\mathbf{c}_s - \mathbf{u}_s)^2}{2\,\Theta}\right] \tag{10}$$

Clearly, the zeroth-order solution cannot hold for granular matter because of the steady state and no-external force assumptions, hence the velocity distribution function is rather written as a first-order perturbation to the Maxwellian state, $f_1=f_0\cdot(1+{}^1\Phi_f)$, where ${}^1\Phi_f$ ($<<1$) is a measure of the (slight) deviation of f_1 from the Maxwellian distribution and is written as a linear function of

the first derivatives of n, Θ and $\mathbf{u}_s$ with respect of time and space. Various forms of ${}^1\Phi_f$ can be found in *Chapman and Cowling* [*1970*] (chap. 16.3), *Lun et al*. [*1984*], and *Nieuwland et al*. [*1996*]. As mentioned earlier, we have followed *Lun et al*'s model [*1984*]. The deviation from the Maxwellian state is generally minor, e.g., *Chen and Chao* [*1987*] and *Gidaspow and Huilin* [*1998*] have shown experimentally that the velocity distribution function is approximately Gaussian in a fluidized bed.

Assumption 5: The equipartition of fluctuating kinetic energy is assumed to hold (i.e., isotropic granular-temperature), which explains the number 3 in the denominator of Eq.(5).

Within this framework of classical granular kinetic assumptions, it is possible to deduce an effective granular stress tensor that can be divided in two parts: kinetic and collisional [e.g., *Lun et al, 1984*]. In Table 5, we have written the complete formulation of the different components of the granular kinetic-collisional rheological model. It can be seen that those formulations depends on the granular-temperature, which must be calculated from a supplementary transport equations (Eq.(T1.9)). The first term on the LHS represents the net rate of fluctuating energy change and the second term represents the net rate of fluctuating energy transferred by convection into a fixed CV. On the RHS from left to right, we have: (i) the kinetic-collisional viscous dissipation, (ii) reversible work done by volumetric change (expansion/contraction) of the solid phase, (iii) conduction of the granular-temperature (following a Fourier law), (iv) rate of production of granular-temperature by gas-particle slip, where Γ_{slip} is always positive and is given by Eq.(T5.12) [*Koch and Sangani, 1999; Agrawal et al., 2001*], (v) loss of granular heat due to the inelastic nature of grain collisions, where S_{coll} is always positive and is given by Eq.(T5.13); it causes a transformation (or dissipation) of granular-temperature into conventional heat, (vi) gas viscous damping of granular-temperature, where S_{drag} is always positive and is given by Eq.(T5.14). Γ_{slip} and S_{drag} do not exist in earlier granular theories [e.g., in *Jenkins and Savage, 1983; Lun et al., 1984*] which do not consider the gas phase and its effects on the granular-temperature [*Ding and Gidaspow, 1990*]. It should be noted -and this is the 6th and most critical assumption- that the fluid-particle covariance, $\langle \mathbf{C}_g'' \cdot \mathbf{C}_s'' \rangle$ (i.e., production of granular-temperature by the gas phase turbulence) has been ignored because this term it is difficult to calculate and would imply a comprehensive gas-particle turbulence model which is beyond this present project. It is very likely that such a term can be neglected for large, heavy, and inertial particle in a concentrated flow. However for small particles and highly diluted flows (i.e, coignimbrite and

plinian clouds), gas phase fluctuation will be important, and this granular kinetic-collisional model may be inaccurate.

It is worth noting that in Eq.(T5.7) and Eq.(T5.8), the conductivity of the granular-temperature strongly depends on the grain concentration, grainsize and collisional inelasticity. Generally speaking, the higher the grainsize or the higher the grain concentration, the better the granular-temperature conduction. Eq.(T5.13) represents the loss of granular heat due to the inelastic collisions: the higher the concentration or the smaller the grainsize, the higher S_{coll}. In the same vein, the shear viscosity in Eq.(T5.4) and Eq.(T5.6) is also directly proportional to the grain diameter. Consequently, a granular flow made of small grains tends to be much less viscous than a coarse-grained flow because the viscosity is smaller and also because the granular-temperature loss is higher. A close look at Eq.(T1.9) with Eq.(T5.12) to Eq.(T5.14) suggests that a diluted (purely kinetic) granular flow may have higher granular viscosity than a more concentrated kinetic-collisional one as S_{coll} and S_{drag} are negligible, and Γ_{slip} is higher in a purely kinetic flow. The relationships between the granular variables are shown in Figure 7 drawn from numerical data generated by several simulations of pyroclastic-flows and -surges including the simulations analyzed in the companion paper [*Dartevelle et al*., *2003*]. Highly dilute flow ($\varepsilon_s << 10^{-3}$ vol.%) may display high granular-temperature (Figure 7A), hence high granular shear viscosity (Figure 7B). As inelastic collisions become more and more important ($\varepsilon_s >> 10^{-3}$ vol.%), the granular-temperature is dissipated into conventional heat which decreases the viscosity of the granular phase. Hence a predominantly collisional granular flow ($\varepsilon_s >> 1$ vol.%) is less viscous than a highly diluted flow (i.e, purely kinetic) because the granular-temperature dwindles to nothing owing to the predominance of inelastic collisions and the reduction of the mean free path of the grains. At a concentration of 50 vol.%, the plastic-frictional model takes over the kinetic-collisional one (next section §3.3). Those general granular behaviors have also been previously reported by others [e.g., *Lun and Bent, 1994*], particularly the importance of collisions within diluted flows as reported here (O. Simonin, personal communication, 2003) [e.g., *Yamamoto et al., 2001, Simonin et al., 2002*]. Figure 7 will be furthermore discussed in connection with the pyroclastic-flow and -surge dynamics in the companion paper [*Dartevelle et al., 2003*].

From Table 5, it is obvious that there is a strong analogy between the solid phase kinetic-collisional stress constitutive equations and those of the gas phase. For instance, in Eq.(T5.2), the kinetic solid pressure, ${}^{k}P = \varepsilon_s \rho_s \Theta$, is exactly the relationship for an ideal gas, while the supplementary term arising from collisions (${}^{c}P = 4 g_0 \varepsilon_s \eta\, \varepsilon_s \rho_s \Theta$) is just equivalent to the one for

dense gas pressure (i.e., the van der Waals equation of state) [*Chapman and Cowling, 1970; Ding and Gidaspow, 1990*]. Because this collisional pressure term (^{c}P), P_s quasi-monotonically increases with ε_s as collisions becomes more and more predominant (Figure 7C). At concentrations between 20 vol.% to 64 vol.%, ^{c}P starts to decrease owing to the very low values of Θ; at 50 vol.%, the frictional pressure (^{f}P) will take over ^{c}P. The ideal granular viscosity in Eq.(T5.6) (for diluted flow only) can be clearly expressed as for an ideal gas viscosity:

$$\mu_s^{dil} \propto \underbrace{\frac{d}{\varepsilon_s}}_{\text{mean free-path}} \underbrace{\hat{\rho}_s}_{\text{density}} \underbrace{\sqrt{\Theta}}_{\text{square-root of temperature}}$$

However, at higher concentration when inelastic collisions becomes more and more prevalent, this simple relationship does not hold valid anymore and, instead, Eq.(T5.4) is used where ζ and η take into account inelastic collisional effects, non-punctual volume effects (i.e., when the mean fee path is equivalent to the grain diameter), and correction effects of the molecular chaos.

3.3. Frictional stress

At very high concentrations and low rate-of-strain, collisions cannot be seen as instantaneous anymore [*Savage, 1983*]. Therefore, a frictional stress model must be taken into account. This can be achieved using plasticity theories in which the material behavior is assumed to be independent of the rate-of-strain [*Tüzün et al., 1982*]. Needless to say, this is atypical for a viscous Newtonian or Bingham flow where stress specifically depends on the rate-of-strain. Under a normal stress, a granular material will shear only when the shear stress attains a critical magnitude. This can be described -among many other laws- by a Mohr-Coulomb law based on the laws of sliding friction [*Syamlal, 1987*]. However, the Mohr-Coulomb law and other yielding laws say nothing about how the granular material deforms and flows, it rather describes the *onset of yielding* [*Jackson, 1983; Syamlal, 1987*]. The plastic potential theory will provide the required constitutive equations for describing the deformation of a granular material under frictional motions [*Drucker and Prager, 1952; Schofield and Wroth, 1968; Jackson, 1983; Schaeffer, 1987*] in agreement with the behaviors of granular material described by the critical state theory (which will not be detailed here, see http://www.granular.org, *Schofield and Wroth* [*1968*],

Jackson [*1983*], *Pitman and Schaeffer* [*1987*], *Nedderman* [*1992*], *Dartevelle* [*2003*]). However, the 2D Mohr-Coulomb yielding law or, in 3D, the extended von Mises yielding law, lead to three unacceptable physical inconsistencies within the plastic potential framework: (i) it predicts an infinite dilatancy of the granular medium as deformation proceeds, (ii) as a consequence of the latter, it is unable to describe the contractancy (or work-hardening) and critical state behaviors, and (iii) it predicts a nil rate of energy dissipation which is clearly inconsistent with the microscopic behavior of a loss of mechanical energy caused by the friction between the sliding particles [*Syamlal, 1987; Gray and Stiles, 1988*]. A better 3-dimensional yielding law must be defined for our purpose: (i) being easily useable within the plastic potential framework, (ii) being able to successfully describe the phenomenon of dilatancy (or failure, work-softening), contractancy (or consolidation), critical state (no bulk density change), (iii) leading to an independence between the rate-of-strain and the stress tensors, and (iv) predicting positive plastic dissipation of energy.

Let ${}^{f}T_{ii}$ be the elements of a stress tensor of the solid phase ${}^{f}\mathbf{T}_s$ in any coordinate system X_i (i=1,2,3), and let the eigenvalues of ${}^{f}\mathbf{T}_s$ be σ_1, σ_2, σ_3 with $\sigma_1 \geq \sigma_2 \geq \sigma_3$ and their associated eigenvectors (principal directions) be $\mathbf{n}_1$, $\mathbf{n}_2$, $\mathbf{n}_3$ respectively. In the Mohr-Coulomb case, ${}^{f}T_{22} = \sigma_2$ and the principal direction $\mathbf{n}_1$ forms an angle ψ measured counterclockwise with the X_1-direction, which lead to a simple 2-dimensional analysis of stress (within the plane X_1X_3). It is relatively easy to show that the onset of yielding described by Mohr-Coulomb can be written in terms of the eigenvalues of ${}^{f}\mathbf{T}_s$ assuming a cohesionless, rigid-plastic, isotropic granular materials [*Tüzün et al., 1982*]:

$$\tau = \langle \sigma \rangle \sin \phi_s \qquad \text{a.}$$

$$\frac{\sigma_1}{\sigma_3} = \frac{1 + \sin \phi_s}{1 - \sin \phi_s} \qquad \text{b.} \qquad (11)$$

$$\left(\sigma_1 - \langle \sigma \rangle\right)^2 + \left(\sigma_3 - \langle \sigma \rangle\right)^2 = 2 \langle \sigma \rangle^2 \sin^2 \phi_s \qquad \text{c.}$$

which are three different forms of the same Mohr-Coulomb yield condition (equality only holds at yield), where ϕ_s is the angle of repose of the granular materials (or the angle of internal friction). This angle of repose is low when grains are smooth, coarse or rounded, and high for sticky, sharp, or very fine particles. Typically, ϕ_s is between 15^o and 50^o [*Nedderman*, *1992; Gidaspow, 1994*]. Experiments suggest that this coefficient of friction drops when motions

begins, i.e., the kinetic friction coefficient is less than the static coefficient. However, no data exist for granular material, and the universal assumption is that the kinetic and static coefficient of friction are more and less equal [*Gray and Stiles, 1988*]. The normal and shear stress in the principal stress components are (in 2D):

$$\langle\sigma\rangle = \frac{\sigma_1 + \sigma_3}{2} \qquad \text{a.}$$
$$\tau = \frac{\sigma_1 - \sigma_3}{2} \qquad \text{b.} \tag{12}$$

Eq.(11) shows the admissible states of stress and states that slip occurs if and only if equality holds. The linear relation between τ and $\langle\sigma\rangle$ or σ_1 and σ_3 is called the *yield line* in the *stress plane* defining a *yield condition* as shown in Figure 8A drawn from Eq.(11b).

One of the main problem of the Mohr-Coulomb law is its 2-dimensional nature (i.e., ${}^{f}T_{22} = \sigma_2$), hence the failure criterion is independent of the intermediate principal stress. This assumptions would be acceptable in 2D axisymmetric problem (typically in a silo) with $\mathbf{n}_2$ parallel to the axis of symmetry. Such imposed symmetry cannot be reconciled with the 3D general nature of granular gravity-currents. Fortunately, it is easy to generalize in 3D using the extended von Mises yield criterion (or conical yield criterion):

$$\tau = \langle\sigma\rangle \sin\phi_s \qquad \text{a.}$$
$$II_{dT} = \langle\sigma\rangle^2 \sin^2\phi_s \qquad \text{b.} \tag{13}$$

which are 2 different forms of the same extended von Mises yield condition, where the octahedral normal and shear stress are given by [*Nedderman, 1992*]:

$$\langle\sigma\rangle = \frac{\sigma_1 + \sigma_2 + \sigma_3}{3} \qquad \text{a.}$$
$$\tau = \sqrt{\frac{(\sigma_1 - \sigma_2)^2 + (\sigma_2 - \sigma_3)^2 + (\sigma_3 - \sigma_1)^2}{6}} = \sqrt{II_{dT}} \qquad \text{b.} \tag{14}$$

and II_{dT} is the second invariant of the deviator of the frictional stress tensor ${}^{f}\mathbf{T}_s$ (see Eq.(A.5) in the Appendix 2). In Eq.(14b) each principal stress difference is equal to the diameter of the

appropriate Mohr's circle. Whenever the intermediate principal stress is equal to the average between the minor and major principal stress, we find the 2D Mohr-Coulomb yield criterion. In 3D, in the principal stress space, the extended von Mises yield has the geometrical shape of a cone with its apex at the origin and its axis of symmetry represents the hydrostatic/isotropic pressure (see Figure 8B). However, as it will become clear with the plastic potential theory, it is required to modify the conical yield in order to account for compressibility effects (dilatancy and contractancy) in the granular phase. This new "compressible" yield function:

$$II_{dT} = \left(2\,{}^{f}P - \langle\sigma\rangle\right)\langle\sigma\rangle \sin^2\phi_s \tag{15}$$

where ${}^{f}P$ is the "Equation of State" (EOS) of frictional granular matter, positive function which measures the compressibility of the granular matter and increases monotonically with the solid volumetric concentration (see Eq.(T5.19)). According to Eq.(15), the higher the solid volumetric concentration, the higher ${}^{f}P$, the higher the strength of the plastic granular material. This "compressible" yield function has been formulated in 3D by *Gray and Stiles* [*1988*] based upon the 2D compressible granular flow work of *Pitman and Schaeffer* [*1987*] and is equivalent to Roscoe and co-workers yield model developed in soil mechanics at Cambridge University [*Schofield and Wroth, 1968*]. In the principal stress space (Figure 8C), the yield surface has a shape of a circular ellipsoid with the hydrostatic axis as principal axis. The radius of this function is given by [*Gray and Stiles, 1988*]:

$$\sqrt{2\sin^2\phi_s \left\| \left(\langle\sigma\rangle - {}^{f}P\right)^2 - {}^{f}P^2 \right\|} \tag{16}$$

At its the two apexes, the radius is zero (on the hydrostatic axis for $\langle\sigma\rangle=0$ and $\langle\sigma\rangle=2\,{}^{f}P$), and the radius is maximum whenever $\langle\sigma\rangle={}^{f}P$ which defines a critical state. A close inspection of Figure 8C shows that this new yield function has a convexity. Hence according to the critical state theory, the normal to the surface has a negative projection on the hydrostatic axis for $\langle\sigma\rangle<{}^{f}P$ (failure process), a positive projection for $\langle\sigma\rangle>{}^{f}P$ (consolidation process), and an orthonormal projection at $\langle\sigma\rangle={}^{f}P$ (critical state where there is no change of the bulk density).

Those three previous yield functions say nothing about the nature of motion initiated at yield [*Jackson, 1983*]. The plastic potential theory provides a way to predict the velocity distribution

within the granular medium, at yield, using three concepts: (i) a yield function Y, (ii) a plastic potential function G, and (iii) a flow rule [*Schaeffer, 1987; Gray and Stiles, 1988; Nedderman, 1992*]. The plastic potential function (G) is defined so that the rate-of-strain of the granular phase in any arbitrary directions (D_{ij}) is proportional to the derivative of G with respect to the corresponding stress ($^{f}T_{ij}$):

$$\mathbf{D}_s = q\frac{\partial G}{\partial\, {}^{f}\mathbf{T}} \qquad \text{a.}$$
$$\boldsymbol{\Delta} = q\frac{\partial G}{\partial \boldsymbol{\sigma}} \qquad \text{b.} \tag{17}$$

where q is a positive scalar named "plastic multiplier". This scalar is not a property of the material but rather a property of the flow conditions. Eq.(17b) expresses the same relation in terms of the eigenvalues of $\mathbf{D}_s$ (i.e., Δ_i) and $^{f}\mathbf{T}$ (i.e., σ_i). According to the associated flow rule, the plastic potential function is the yield function itself, i.e., Mohr-Coulomb: Eq.(11), extended von Mises: Eq.(13), modified von Mises: Eq.(15). Substituting the modified "compressible" von Mises (Eq.(15)) and the definition of II_{dT} in the Appendix 2 (Eq.(A.5b)) into Eq.(17b):

$$\Delta_i = q\left[\frac{\partial Y}{\partial \sigma_i}\right] = q\left[\left(\sigma_i - \langle\sigma\rangle\right) + \frac{2}{3}\sin^2\phi_s\left(\langle\sigma\rangle - {}^{f}P\right)\right] \tag{18}$$

From Eq.(17) and Eq.(18) we can state the two key properties of the plastic potential theory. First, the co-axiality which states that the principal axes of the rate-of-strain are aligned with those of stress in agreement with the intuitive idea that the material should respond to unequal stress by contracting in direction of greater stress and expanding in the direction of lesser stress. Second, the normality which is a direct consequence of Eq.(17) since, at yield, $\boldsymbol{\Delta}$ must be a vector perpendicular to the level surface G in the principal stress space. Calculating the first invariant of the rate-of-strain tensor, I_D for the three yield functions (in terms of the principal rate-of-strain):

Modified "compressible" von Mises case:

$$\nabla \cdot \mathbf{u}_s = -I_D = -\sum_{i=1}^{3} \Delta_i = -2\, q \sin^2 \phi_s \left(\langle \sigma \rangle - {}^{f}P \right) \qquad \text{a.}$$

Mohr-Coulomb case (2D) and extended von Mises case (3D):

$$\nabla \cdot \mathbf{u}_s = -I_D = 2\, q \sin^2 \phi_s \langle \sigma \rangle \quad > 0 \qquad \text{b.}$$

(19)

where for Eq.(19b), we have used Eq.(17b) with the yield function given by Eq.(11c) (Mohr-Coulomb case) or Eq.(13b) (extended von Mises case). Eq.(19) is an important results as in both Mohr-Coulomb and extended von Mises cases, the granular body, at yield, suffers an unbounded and continued dilatation (i.e., divergence of the velocity field is always positive), which is physically impossible. While in the modified "compressible" von Mises case, the divergence of the velocity field will be positive or negative depending on the sign of $\langle \sigma \rangle - {}^{f}P$. Whenever $\langle \sigma \rangle - {}^{f}P<0$, the divergence is positive in agreement with Reynolds' principle of dilatancy, when $\langle \sigma \rangle - {}^{f}P>0$, we have a consolidation process (or compression). And when $\langle \sigma \rangle - {}^{f}P=0$, a critical state with neither expansion, nor compression as expected by the critical state theory [*Jackson, 1983*]. Within the modified "compressible" von Mises yield, we may rewrite with a few manipulations Eq.(18) using Eq.(19a) as:

$$\mathbf{D}_s = q\, {}^{f}\overset{\circ}{\overset{=}{\mathbf{T}}} + \frac{2}{3} q \sin^2 \phi_s \left(\langle \sigma \rangle - {}^{f}P \right) \mathbf{I} \qquad \text{a.}$$

$$\Leftrightarrow \quad \mathbf{D}_s = q\, {}^{f}\overset{\circ}{\overset{=}{\mathbf{T}}} - \frac{1}{3} \nabla \cdot \mathbf{u}_s \, \mathbf{I} \qquad \text{b.}$$

$$\Rightarrow \quad \overset{\circ}{\overset{=}{\mathbf{D}}}_s = q\, {}^{f}\overset{\circ}{\overset{=}{\mathbf{T}}} \qquad \text{c.}$$

(20)

Eq.(20c) states a proportional relationship between the deviator of the rate-of-strain (pure shear) and the deviator of the stress within the granular medium. Such a flow rule, which is a direct result from the plastic potential theory, is often named the *Levy-von Mises flow rule* [*Nedderman, 1992*] and necessarily implies that the granular flow is slightly compressible. Thanks to this flow rule, it is possible to find the plastic multiplier from Eq.(20c), using Eq.(15) and Eq.(19a):

$$\left\| \overset{\circ}{\overline{\mathbf{D}}}_s \right\| = q \left\| {}^{f}\overset{\circ}{\overline{\mathbf{T}}} \right\| \qquad \text{a.}$$

$$\Leftrightarrow \quad II_{dD} = q^2 \; II_{dT} \qquad \text{b.}$$

$$\Leftrightarrow \quad II_{dD} = q^2 \sin^2 \phi_s \left[{}^{f}P^2 - \frac{\left(\nabla \cdot \mathbf{u}_s \right)^2}{4\, q^2 \sin^4 \phi_s} \right] \qquad \text{c.} \tag{21}$$

$$\Rightarrow \quad q = \frac{\sqrt{4 \sin^2 \phi_s \; II_{dD} + \left(\nabla \cdot \mathbf{u}_s \right)^2}}{2 \sin^2 \phi_s \; {}^{f}P} \qquad \text{d.}$$

which shows that, except for ϕ_s, q is a function of the flow properties and not the material itself. Once the plastic multiplier is known, it is not too difficult to find an expression for the granular frictional shear viscosity ($^{f}\mu$) and the bulk viscosity ($^{f}\mu^{b}$) as seen in Table 5, knowing that for any stress tensor $\mathbf{T} = \overset{\circ}{\mathbf{T}} + \overset{\circ}{\overline{\mathbf{T}}}$, the spherical part is ${}^{f}\overset{\circ}{\mathbf{T}} = \langle \sigma \rangle \mathbf{I} = \left({}^{f}P - {}^{f}\mu^{b} \, \nabla \cdot \mathbf{u}_s \right) \mathbf{I}$, and the deviatoric part is ${}^{f}\overset{\circ}{\overline{\mathbf{T}}} = 2 \, {}^{f}\mu \, \overset{\circ}{\overline{\mathbf{D}}}_s = 2 \, {}^{f}\mu \left(\mathbf{D}_s + \frac{1}{3} \nabla \cdot \mathbf{u}_s \, \mathbf{I} \right)$. A close inspection of Eq.(T5.20), Eq.(T5.21) and Eq.(21d) shows that the frictional viscosities for a given angle of internal friction is not a property of the material but rather of the flow. For a given solid volumetric concentration (i.e., constant ^{f}P) the frictional viscous stress tensor is independent of the rate-of-strain tensor as required by the plasticity theory. Indeed, if the components of $\mathbf{D}_s$ are multiplied by a factor, the components of the stress tensor remain unchanged (because II_{dD} and $\nabla \cdot \mathbf{u}_s$ at the denominator) (i.e., frictional flow must be rate-of-strain independent). Lastly, for a given rate-of-strain or a given applied normal stress on the granular material, the higher ε_s, the higher ^{f}P, the higher the strength of the material II_{dT}, the higher the granular frictional viscosities. In addition, the frictional viscous dissipation, $^{f}\Phi$:

Modified "compressible" von Mises case:

$$^{f}\Phi = \sum_{i=1}^{3} \sigma_i \; \Delta_i = 2 \, q \sin^2 \phi_s \, \langle \sigma \rangle \, {}^{f}P \quad > 0 \qquad \text{a.}$$

Mohr-Coulomb (2D) and extended von Mises case (3D):

$$^{f}\Phi = 0 \qquad \text{b.} \tag{22}$$

${}^{f}\Phi$ is always positive with the "compressible" yield function as required by thermodynamics but ${}^{f}\Phi$ is always equal to zero for both the extended von Mises and Mohr-Coulomb yields which is an unacceptable result for frictional flows. In Figure 7, it can be seen that when the volumetric grain concentration reaches 50 vol.%, ${}^{f}P$ and ${}^{f}\mu$ increase with the solid concentration and asymptotically go to infinite when ε_s~64 vol.%. At this concentration, the granular flow is quasi-frozen and immobile. Hence, the implementation of such plastic rheological behavior in multiphase computer model is fundamentally important since it enables to simulate depositional processes as demonstrated in the companion paper [*Dartevelle et al*., *2003*].

4. Large Eddy Simulation closures

Turbulence is a very complex phenomenon and, in general, it is difficult to model with great details and without some empiricisms. However, there are some minimal properties of turbulence that a model should attempt to capture. Turbulence possesses structure on many scales where the turbulent kinetic energy, $E(k_\lambda)$, cascades towards the smallest scales (Kolmogorov scale) where molecular (or granular) viscosity dissipate the turbulent kinetic energy. Turbulence strongly depends on mean flow properties, hence is time and space dependent. It significantly contributes to the transport of momentum, heat and mass [*Rodi, 1993*]. The nature of turbulence can be captured by means of Large Eddy Simulation models (LES). LES directly simulates the large scale effects of turbulence (large eddies, e.g., a few meters to ~1000m, or more) and only models the effects of turbulence within the subgrid level (cm to a few meters) [*Moeng, 1984*]. If the resolution length scale, λ, of the largest unresolved turbulent eddies (or wave number scale $k_\lambda=\lambda^{-1}$) lies within the Kolmogorov inertial range with energy cascade rate ε_E whose energy density or spectrum is given by the law, $\Lambda(k_\lambda) \propto \varepsilon_E^{2/3}\ k_\lambda^{-5/3}$, then the unresolved small scale (subgrid) turbulence must be isotropic and in equilibrium, and simple scaling arguments can be used to deduce an appropriate eddy-viscosity (SGS) and eddy-thermal diffusibility (SGH) [*Smagorinsky, 1993; Leith, 1993*]. The specific turbulent kinetic energy of the unresolved eddies at any wave numbers k_λ [*Leith, 1993*]:

$$E(k_\lambda) \propto \int \Lambda(k_\lambda)\ dk_\lambda \propto \varepsilon_E^{2/3}\ k_\lambda^{-2/3} \propto \varepsilon_E^{2/3}\ \lambda^{2/3} \tag{23}$$

Following *Smagorinsky* [*1963*], the eddy viscosity is based on a local balance between shear production of subgrid turbulent kinetic energy $E(k_\lambda)$ and its removal by cascade and viscous

dissipation at the rate ε_E. The turbulent subgrid shear stress (SGS) and turbulent heat flux (SGH) are respectively proportional to the mean velocity gradient and to the mean temperature gradient [*Bellan, 2000*]:

$$\begin{aligned} {}^{tur}\boldsymbol{\tau} &= 2\ {}^{tur}\mu\ \overset{\circ}{\overline{\overline{\mathbf{D}}}} \\ {}^{tur}\mathbf{q} &= -\,{}^{tur}k\,\nabla T \end{aligned} \tag{24}$$

where ${}^{tur}\mu$ is the turbulent (eddy-) viscosity, which must scale with the root-mean-square velocity times the turbulent resolution scale, $\propto \rho\,\lambda\sqrt{E(k_\lambda)}$ [*Leith, 1993*], ${}^{tur}k$ is the thermal (eddy-) conductivity of heat due to turbulence, and $\overset{\circ}{\overline{\overline{\mathbf{D}}}}$ is the resolved deviatoric rate-of-strain tensor (given by Eq.(A.2) in Appendix 2). The local shear production of subgrid turbulence kinetic energy is given by the eddy-viscous shear stress work, $2\ {}^{tur}\mu\ tr\left(\overset{\circ}{\overline{\overline{\mathbf{D}}}}\cdot\overset{\circ}{\overline{\overline{\mathbf{D}}}}\right) = 2\ {}^{tur}\mu\ II_{dD}$, where 'tr' is the trace operation of matrices and II_{dD} is the second invariant of $\overset{\circ}{\overline{\overline{\mathbf{D}}}}$ (Eq.(A.6)). The local production-dissipation turbulence balance condition imposes that $2^{tur}\mu II_{dD}=\rho\varepsilon_E$, or from Eq.(23), $E(k_\lambda)\propto\lambda^2\ II_{dD}$, leading to the classical formulation of the static Smagorinsky model [*Smagorinsky, 1963, 1993; Leith, 1993; Travis et al., 1998*]:

$${}^{tur}\mu \propto \rho\,\lambda^2\ \sqrt{II_{dD}} = \frac{\left(C\,\Delta\right)^2}{\sqrt{2}}\,\rho\left\|\overset{\circ}{\overline{\overline{\mathbf{D}}}}\right\| \tag{25}$$

where C is the so-called Smagorinsky "constant" (dimensionless); Δ is the geometric mean of the grid-size, hence $(C\cdot\Delta)$ is the equivalent of the Prandtl mixing length [*Nieuwstadt et al., 1991*]; $\left\|\overset{\circ}{\overline{\overline{\mathbf{D}}}}\right\| = \sqrt{II_{dD}}$ is the Euclidian norm of the deviator of the rate-of-strain. This is exactly the relationships shown in Eq.(T6.5) for the gas phase, where C_g=0.330 is taken from *Lilly* [*1983*]. In Table 6, the gas phase follows the Stokes assumption (hence viscous stress is only shear stress). From the turbulent eddy-viscosity, the eddy-heat diffusibility is given by:

$$^{tur}k = \frac{Cp}{^{tur}Pr}\ ^{tur}\mu \qquad (26)$$

where ^{tur}Pr is the turbulent Prandtl number (dimensionless and constant) and Cp is the specific heat at constant pressure. Eq.(26) is shown in Eq.(T4.9) for the gas phase and Eq.(T4.10) for the solid phase, where ^{tur}Pr is set to 0.95 for both phases.

The LES approach is very popular among atmospheric scientists [e.g., *Lilly, 1962; Smagorinsky, 1963; Deardorff, 1971; Schumann, 1975; Cotton, 1975; Cotton and Tripoli, 1978; Moeng, 1984; Nieuwstadt et al., 1991; Mason, 1989*] and has been used for more than 10 years in the PDAC2D and similar codes for modeling diluted granular flows [e.g., *Dobran et al., 1993; Neri and Macedonio, 1996; Todesco et al., 2002*] even though the SGH is strangely omitted in PDAC2D. The SGS and SGH are easily computed knowing the eddy-viscosity and the eddy-thermal conductivity of the gas phase. The major gain we have from the entrainment law used in the Lagrangian parametric model of plinian clouds [*e.g., Sparks, 1986; Carey and Sparks, 1986; Woods, 1988; Woods and Wohletz, 1991; Woods and Self, 1992; Bursik et al., 1992; Woods, 1993; Koyaguchi and Woods, 1996; Glaze and Baloga, 1996; Glaze et al., 1997; Veitch and Woods, 2000*] is that both eddy-viscosity and the eddy-thermal conductivity are not a fluid constant property but rather depends on the state of turbulence within the flow, and may vary both in space and time (as we would rather expect from turbulence). However, LES is not free of criticisms. First, there is an uncertainty regarding the exact value of the Smagorinsky coefficient (C in Eq.(25)) as it can have all the values between 0.336 and 0.0649 [*Smagorinsky, 1993*] and may not be simply constant at all [*Germano et al., 1991*]. Second, when static LES is applied to complex flows (like geophysical flows) and/or high Reynolds number flows (which is most of the time our main concern) much of the Reynolds stress lies in the unresolved scales, which makes LES very sensitive to the exact LES model chosen [*Ferziger, 1993*]. Third, and most importantly, in multiphase flow, it is questionable to neglect the modulation by the particles upon the gas phase turbulence [*Bellan, 2000*] unless the flow is highly diluted. LES model with a two-way coupling (gas phase turbulence↔dispersed phase turbulence) is beyond our current computer capability and because is not yet very well-understood within the LES framework [*Valentine, 1998*]. Therefore, approximate approaches are required to carry out the numerical analyses [*e.g., Crowe et al, 1996*]. In our view, a complete multiphase turbulence model with two-way contributions should be a priority in geophysical multiphase flow code developments within the next decade.

The turbulence in the dispersed phase is modeled with the kinetic-collisional approach seen earlier (${}^{tur}\mu_s={}^{k/c}\mu_s$ in Eq.(T6.10)). However, because we have disregarded the contribution of the gas phase turbulence into the solid phase (and vice-versa), it is expected that in the dilute limit, at high-Reynolds number in small particle-size flow, the turbulence contribution will not be approached correctly with the kinetic-collisional model. Hence, we need to account in a more semi-empirical manner for turbulence effects in the dilute limit of granular flows. *Agrawal et al.* [*2001*] noticed that, in "fluid catalytic cracking risers", coarse-grid simulations (coarse relative to the size of the grains fluctuation spatial scale) with fully turbulent flows, the dispersed phase stress induced by the mesoscale fluctuations is significantly larger than the stress induced by the kinetic-collisional model. In other words, the kinetic-collisional stress is confined and only relevant at the subgrid level, hence kinetic stress can be "encompassed" within an appropriate SGS model ("appropriate" means a subgrid model that would somehow model the effects of the unresolved mesoscale structures upon the bulk flow dynamic [*Agrawal et al., 2001*]). *Agrawal et al*. [*2001*] suggested that the turbulent closure should be empirically fitted with data obtained from high resolution simulation, which cannot be done in any practical geophysical situations. However, *Savage* [*1992*] argued that the energy spectra of turbulence of the particulate phase follows a similar Kolmogorov -5/3 power-law as seen in Eq.(23). This would suggest that the argumentation seen earlier for the gas phase would hold to define the SGS of the dispersed phase as long as the flow is very diluted and not subject to collisions (hence what rather matters is the turbulence from the gas phase and much less from the dispersed phase). Within such conditions, we have defined an eddy-viscosity of the dispersed phase in Eq.(T6.13) with the kinetic-collisional model turned off (as it is irrelevant within a very coarse grid). This subgrid model within the dispersed phase will be used in the companion paper [*Dartevelle et al., 2003*] for modeling plinian clouds only, which are assumed to be made of small particles of 50 μm, diluted ($\varepsilon_s \approx 10^{-9}$ up to $\approx 10^{-4}$, hence only turbulence in the gas phase matters, much less in the dispersed phase), highly turbulent (Re>>1000), and over coarse-grid (not smaller than 25 meters). In the companion paper, it will be shown that such relatively simple approach of subgrid stress turns out to be highly efficient and sufficient for capturing all the main features of plinian clouds (fluctuating heights with time, magnitude of adiabatic cooling of rising clouds, total altitude compared to real observations and *Morton et al*'s model [*1956*], … see *Dartevelle et al.* [*2003*]).

5. Conclusions

We have reviewed 30 years of continuous research on multiphase flows and on the development of appropriate rheology to model granular flows at any concentrations (dilute to purely frictional). In the frictional regime ($50<\varepsilon_s<64$ vol.%), we have set up a plastic-rigid model able to approach all the expected behaviors of granular matter at those high-concentrations, viz. dilatancy, contractancy and critical state. This can only be achieved in rightly acknowledging the compressibility of granular matter at high-concentrations. The yield strength of frictional granular materials is concentration and flow conditions dependent; e.g., the higher the concentration, the higher the frictional-plastic granular viscosity, the higher the yield strength. From dilute to concentrated flows ($\sim 10^{-4}< \varepsilon_s<60$ vol.%), grains kinetically fluctuate with the collisional mode becoming more and more dominant with concentration. As collisions increase, granular viscosity mostly decreases within the flow because the granular-temperature is decreased by the inelastic nature of collisions. In the highly dilute regime ($\varepsilon_s<10^{-4}$ vol.%), the gas phase turbulence mostly dominates the dynamic of the whole flow and turbulent effects may be simply approached with the means of Large Eddy Simulations models.

In a nutshell, the granular viscosity is highly nonlinear, unsteady, non-uniform, and concentration dependent. Granular viscous stress is rate-of-strain independent in the frictional case and rate-of-strain dependent in the kinetic-collisional case. These rheological models allow us to model granular flows at any concentrations as demonstrated in the companion paper [*Dartevelle et al., 2003*].

In its present state, the main shortcomings of this model are (i) only one grainsize; (ii) in the hydrodynamic model, water phase change do not occur; (iii) no-coupling between turbulence in the gas phase and turbulence in the solid phase. The challenge for geophysical multiphase flow modelers is the two-way coupling multiphase turbulence model, particularly when applied to atmospherical applications.

6. References

Agrawal, K.; P.N. Loezos; M. Syamlal; and S. Sundaresan, The role of meso-scale structures in rapid gas-solid flows, *J. Fluid Mech*., 445, 151-185, 2001.

Alder, B.J. and T.E. Wainwright, Studies in molecular dynamics. II. Behavior of a small number of elastic spheres, *J. Chem Phys*., 33, 1439-1451, 1960.

Anderson, T.B. and R. Jackson, A fluid mechanical description of fluidized bed, *I&EC Fundam.*, 6, 527-539, 1967.

Anderson, K.G., and R. Jackson, A comparison of the solutions of some proposed equations of motion of granular materials for fully developed flow down inclined planes, *J. Fluid Mech*., 241, 145-168, 1992.

Bagnold, R.A., Experiments on a gravity-free dispersion of large solid spheres in a Newtonian fluid under shear, *Proc. Royal Soc. London*, 225, 49-63, 1954.

Batchelor, G.K., A new theory of the instability of a uniform fluidized bed, *J. Fluid Mech.*, 193, 75-110, 1988

Bellan, J. Perspectives on large eddy simulations for sprays: Issues and solutions, *Atomization and Sprays*, 10, 409-425, -2000.

Besnard, D.C., and F.H. Harlow, Turbulence in multiphase flow, *Int. J. Multiphase Flow*, 14, 679-699, 1998.

Bird, R.B.; R.C. Armstrong; and O. Hassager, Dynamics of polymeric liquids. Volume 1. Fluid Mechanics, pp. 470, *John Wiley and Sons, New-York*, 1977.

Boyle, E. and M. Massoudi, Kinetic theories of granular materials with applications to fluidized beds, Technical Report, *US Dept of Energy, DOE/METC—89/4088, DE89 000977*, pp. 66, 1989.

Braney, M.J. and P.A. Kokelaar, A reappraisal of ignimbrite emplacement: progressive aggradation and changes from particulate to non-particulate flow during emplacement of high-grade ignimbrite, *Bull. Volcanol*., 54, 504-520, 1992.

Brey, J.J.; J.W. Dufty; and A. Santos, Kinetic models for granular flow, *J. Stat. Physics*, 281-322, 1999.

Bursik, M.I., R.S.J. Sparks, J.S. Gilbert, and S.N. Carey, Sedimentation of tephra by volcanic plumes: I. Theory and its comparison with a study of the Fogo A plinian deposit, Sao Miguel (Azores), *Bull. Volcanol*., 54, 329-344, 1992.

Calder, E.S.; R.S.J. Sparks; and M.C. Gardeweg, Erosion, transport and segregation of pumice and lithic clasts in pyroclastic flows inferred from ignimbrite at Lascar Volcano, Chile, *J. Volcanol. Geotherm. Res*., 104, 201-235, 2000.

Campbell, C.S., and D.G. Wang, Particle pressures in a gas-fluidized beds, *J. Fluid Mech*., 227, 495-508, 1991.

Carey, S. and R.S.J. Sparks, Quantitative models of the fallout and dispersal of tephra from volcanic eruption columns, *Bull. Volcanol*., 48, 109-125, 1986.

Carnahan, N.F. and K.E. Starling, Equations of state for non-attracting rigid spheres, *J. Chem. Phys*., 51, 635-636, 1969.

Chapman, S. and Cowling, T.G., The mathematical theory of non-uniform gases, 3rd Ed., pp. 423, *Cambridge University Press*, 1970.

Chen, M.M. and B.T. Chao, Hydrodynamics, mixing, and segregation in gas fluidized beds, Technical Progress Report, 22nd October, 1986 to 21st January, 1987, pp. 21, *Dept. Of. Energy, DOE-PETC, DOE/PC/80511-T6*, 1987.

Cotton, W.R., On parameterization of turbulent transport in cumulus clouds, *J. Atmos. Sci*., 32, 548-564, 1975.

Cotton, W.R., and G.J. Tripoli, Cumulus convection in hear flow – Three dimensional numerical experiments, *J. Atmos. Sci*., 35, 1503-1521, 1978.

Crowe, C.T.; T.R. Troutt; and J.N. Chung, Numerical models for two-phase turbulent flows, *Annu. Rev. Fluid. Mech*., 28, 11-43, 1996.

Deardorff, J.W., On the magnitude of the subgrid scale eddy coefficient, *J. Comput. Phys*., 7, 120-133, 1971.

Dartevelle, S., Numerical and granulometric approaches to geophysical granular flows, Ph.D. dissertation thesis, *Michigan Technological University, Dept. of Geological and Mining Engineering*, Houghton, Michigan, 2003.

Dartevelle, S., G.J.G. Ernst, J. Stix, and A. Bernard, Origin of the Mount Pinatubo climactic eruption cloud: Implications for volcanic hazards and atmospheric impacts, *Geology*, 30, 663-666, 2002.

Dartevelle, S.; W.I. Rose; J. Stix; K. Kelfoun; and J. Vallance, Numerical modeling of geophysical granular flows. II. Computer simulations of plinian clouds, pyroclastic flows and surges, *in review*, *G-cubed*, 2003.

Davidson, J.F. D. Harrison, and J.R.F. Guedes de Carvalho, On the liquid like behavior of fluidized beds, *Ann. Rev. Fluid Mech*., 9, 55-86, 1977.

Denlinger, R.P., and R.M. Iverson, Flow of variably fluidized granular masses across three-dimensional terrain. 2. Numerical predictions and experimental tests, *J. Geophys. Res*., 106, 553-566, 2001.

Didwania, A.K., and G.M. Homsy, Rayleigh-Taylor instabilities in fluidized beds, *I&EC Fundam*., 20, 318-323, 1981.

Ding, J. and D. Gidaspow, A bubbling fluidization model using kinetic theory of granular flow, *AIChE J*., 36, 523-538, 1990.

Dobran, F., A. Neri, and G. Macedonio, Numerical simulations of collapsing volcanic columns, *J. Geophys. Res*., 98, 4231-4259, 1993.
Drew, D.A., Mathematical modeling of two-phase flow, *Ann. Rev. Fluid Mech*., 15, 261-291, 1983.
Drucker, D.C.; and W. Prager, Soil mechanics and plastic analysis or limit design, *Quart. J. Appl. Math*., 10, 157-165, 1952.
Ennis, B.J., J. Green, and R. Davies, The legacy of neglect in the U.S., *Chem. Eng. Prog*., 90, 32-43, 1994.
Ergun, S. Fluid flow through packed columns, *Chem. Eng. Prog*., 48, 89-94, 1952.
Ferziger, J.H., Subgrid-scale modeling, in Large Eddy simulation of complex engineering and geophysical flows, B. Galperin and S.A. Orszag eds. , 37-54, *Cambridge University Press*, 1993.
Freundt, A., Formation of high-grade ignimbrites. Part II. A pyroclastic suspension current model with implications also for low-grade ignimbrites, *Bull. Volcano*., 60, 545-567, 1999.
Freundt, A., and M. Bursik, Pyroclastic flow transport mechanisms, in From Magma to Tephra, modeling Physical Processes of Explosive Volcanic Eruptions, A. Frendt and M. Rosi eds., Elsevier, 173-243, 1998.
Germano, M., U. Piomelli,, P. Moin, and W.H. Cabot, A dynamic subgrid-scale eddy viscosity model, *Phys. Fluids A*, 3, 1760-1765, 1991.
Gidaspow, D., Multiphase flow and fluidization. Continuum and kinetic theory descriptions, 467 pp., *Academic Press*, 1994.
Gidaspow, D., and B. Ettehadieh, Fluidization in two-dimensional beds with a jet. 2. Hydrodynamic modeling, *I&EC. Fundam*., 22, 193-201, 1983.
Gidaspow, D. and L. Huilin, Equation of state and radial distribution function of FCC particles in a CFB, *AIChE J*., 44, 279-293, 1998.
Glaze, L.S. and S.M. Baloga, Sensitivity of buoyant plume height to ambient atmospheric conditions: Implications for volcanic eruption columns, *J. Geophys. Res*., 101, 1529-1540, 1996.
Glaze, L.S., S.M. Baloga, and L. Wilson, Transport of atmospheric water vapor by volcanic eruption columns, *J. Geophys. Res*., 102, 6099-6108, 1997.
Goldschmidt, D., and P. Le Goff, Electrical resistance of fluidized beds – Resistance measurements of conducting grains fluidized by air – Preliminary results, *Chem Eng. Science*, 18, 805-806, 1963.
Gombosi, T.I., Gaskinetic Theory, pp. 297, *Cambridge University Press*, 1994.
Grace, J.R., The viscosity of fluidized beds, *Canadian J. Chem. Eng*., 48, 30-33, 1970.
Graham, W., and E.A. Harvey, The electrical conductivity of fluidized beds of coke and Graphite up to 1,200C, *Can. J. Chem. Eng*., 44, 17-19, 1966.
Gray, D.D., and J.M. Stiles, On the constitutive relations for frictional flow of granular materials, pp. 29, *Topical Report U.S. Dept. of Energy*, DOE/MC/21353-2584, DE88001089, 1988.
Gunn, D.J., Transfer of heat or mass to particles in fixed and fluidized beds, *Int. J. Heat Mass Transfer*, 21, 467-476, 1978.
Harlow, F.H. and A., Amsden, Numerical calculation of multiphase fluid flow, *J. Comp. Phys*., 17, 19-52, 1975.
Hill, R., The mathematical theory of plasticity, pp. 355, *Oxford University Press*, 1956.
Homsy, G.M., A survey of some results in the mathematical theory of fluidization, , *in* Theory of dispersed multiphase flow, ed. R.E. Meyer, 57-71, *Academic Press*., 1983.
Ishii, M., Thermo-fluid dynamic theory of two-phase flow, 248 pp., *Eyrolles*, 1975.
Iverson, R.M., and R.P. Denlinger, Flow of variably fluidized granular masses across three-dimensional terrain. 1. Coulomb mixture theory, *J. Geophys. Res*., 106, 537-552, 2001.
Jackson, R. Some mathematical and physical aspects of continuum models for the motion of granular materials, *in* Theory of dispersed multiphase flow, R.E. Meyer (Ed.), 291-337, *Academic Press*, 1983.
Jaeger, H.M., S.R. Nagel, and R.P. Behringer, The Physics of granular materials, *Physics Today*, 49, 32-38, 1996.
Jenkins, J.T. and S.B. Savage, A theory for the rapid flow of identical, smooth, nearly elastic, spherical particles, *J. Fluid Mech*., 130, 187-202, 1983.
Jones, A.L., and T.D. Wheelock, The electrical resistivity of fluidized carbon particles: significant parameters, *Chem. Eng. Prog. Symp. Series*, 66, 157-166, 1970.
Kashiwa, B.A., and W.B. VanderHeyden, Toward a general theory for multiphase turbulence. Part I. Development and Gauging of the model equations, *Los Alamos National Laboratory*, LA-13773-MS, pp. 88, 2000.
Knowlton, T.M., J.W. Carson, G.E. Klinzing, and W-C. Yang, The importance of storage, transfer, and collection, *Chem. Eng. Prog*., 90, 44-54, 1994.
Koch, D.L., and A.S. Sangani, Particle pressure and marginal stability limits for a homogeneous mondispersed gas-fluidized bed: Kinetic theory and numerical simulations, *J. Fluid Mechanics*, 400, 229-263, 1999.
Koyaguchi, T. and A.W. Woods, On the formation of eruption columns following explosive mixing of magma and surface-water, *J. Geophys. Res*., 101, 5561-5574, 1996.
Kuipers, J.A.M.; W. Prins; and W.P.M. van Swaaij, Numerical calculation of wall-to-bed heat transfer coefficients in gas-fluidized beds, AIChE J., 38, 1079-1091, 1992.

Kuipers, J.A.M.; K.J. Duin; F.P.H. van Beckum; and W.P.M. van Swaaij, Computer simulation of the hydrodynamics of a two-dimensional gas-fluidized bed, Computers Chem. Eng., 17, 839-858, 1993.

Lakehal, D. On the modeling of multiphase turbulent flows for environmental and hydrodynamic applications, *Int. J. multiphase Flow*, 28, 823-863, 2002.

Leith, C.E., Stochastic backscatter formulation for three-dimensional compressible flow, *in* Large Eddy simulation of complex engineering and geophysical flows, B. Galperin and S.A. Orszag eds. , 105-116, *Cambridge University Press*, 1993.

Lilly, D.K., On the numerical simulation of buoyant convection, *Tellus XIV*, 2, 148-172, 1962.

Lilly, D.K., Stratified turbulence and the mesoscale variability of the atmosphere, *J. Atmos. Sci*., 40, 749-761, 1983.

Lun, C.K.K.; S.B. Savage; D.J. Jeffrey; and N. Chepurniy, Kinetic theories for granular flows: inelastic particles in Couette flow and slightly inelastic particles in a general flow field, *J. Fluid Mech*., 140, 223-256, 1984.

Lun, C.K.K. and A.A. Bent, Numerical simulation of inelastic frictional spheres in simple shear flow, *J. Fluid Mech*., 258, 335-353, 1994.

Lyczkowski R.W.; D. Gidaspow; and C.W. Solbrig, Multiphase flow models for nuclear, fossil, and biomass energy production, *in* Advances in transport processes (A.S. Mujumdar and R.A. Mashelkar eds.), 198-351, *John Wiley & Sons, New-York*, 1982.

Moeng, C.-H., A large eddy-simulation model for the study of planetary boundary-layer turbulence, *J. Atmos. Sci*., 41, 2052-2062, 1984.

Morton, B.R., G.F.R.S. Taylor, J.S. Turner, Turbulent gravitational convection from maintained and instantaneous sources, *Proc. R. Soc. London A*, 234, 1-23, 1956.

Murray, J.D., On the viscosity of a fluidized system, *Rheologica Acta*, 6, 27-30, 1967.

Nedderman, R.M., Statics and kinematics of granular materials, pp. 352, *Cambridge Univ. Press*, 1992.

Nieuwland, J.J.; M. Van Sint Annaland; J.A.M. Kuipers; and W.P.M. van Swaaij, Hydrodynamic modeling of gas/particles flows in riser reactors, *AIChE J*., 42, 1569-1582, 1996.

Nieuwstadt, F.T.M., P.J. Mason, C.-H. Moeng, and U. Schumann, Large eddy-simulation of the convective boundary layer: A comparison of four computer codes, in Turbulent Shear Flow 8, F. Durst, R. Friedrich, B.E. Launder, F.W. Schmidt, U. Schumann, J.H. Whitelaw eds., *Springer-Verlag*, Berlin, pp. 430, 1991.

Neri, A. and G. Macedonio, Numerical simulation of collapsing volcanic columns with particles of two sizes, *J. Geophys. Res*., 101, 8153-8174, 1996.

Neri, A.; A.D. Muro; and M. Rosi, Mass partition during collapsing and transitional columns by using numerical simulations, *J. Volcanol Geotherm. Res*., 115, 1-18, 2002.

Ogawa, S.; Umemura, A.; and N. Oshima, On the equations of fully fluidized granular materials, *J. Appl. Math. Phys*., 31, 483-493, 1980.

Pigford, R.L., and T. Baron, Hydrodynamic Stability of a fluidized Bed, *I&EC*, 4, 81-87, 1965.

Pitman, E.B., and D.G. Schaeffer, Stability of time dependent compressible granular flow in two dimension, *Comm. Pure Appl. Math*., 40, 421-447, 1987.

Prosperetti, A., Some considerations on the modeling of dispersed multiphase flows by averaged equations, *J.S.M.E. Int. J*., B42 573-585, 1999.

Rampino, M.R., Volcanism, climatic change, and the geological record, Sedimentation in Volcanic Settings, *SEPM Special Publication* 45, 9-18, 1991.

Rasmussen, K., Calculation methods for the physical properties of air used in the calibration of microphones. A proposal for a unified calculation procedure to be used among European metrology laboratories, 2nd Revision, Report PL-11b, pp. 20, *Dept. Acoustic Technology, Technical University of Denmark*, 1997.

Reed, A.K., and W.M. Goldberger, Electrical behavior in fluidized beds of conducting solids, *Chem. Eng. Prog. Symp. Series*, 62, 71-75, 1966.

Rivard, W.C. and M.D. Torrey, K-FIX: A computer program for transient, two-dimensional, two-fluid flow, Los Alamos National Laboratory, LA-NUREG-6623, 1977.

Rivard, W.C. and M.D. Torrey, PERM: Corrections to the K-FIX code, Los Alamos National Laboratory, LA-NUREG-6623 Suppl., 1978.

Rivard, W.C. and M.D. Torrey, THREED: An extension of the K-FIX code for three-dimensional calculations, Los Alamos National Laboratory, LA-NUREG-6623 Suppl. II, 1979.

Robock, A., Volcanic eruption and climate, *Rev. Geophysics*, 38, 191-219, 2000.

Rodi, W., Turbulence models and their applications in hydraulics. A state-of-the-art review, 3rd ed., pp. 104, International Association for Hydraulic Research, *A.A. Belkema Publisher*, Rotterdam, 1993.

Sangani, A.S.; G. Mo; H.-K. Tsao; and D.L. Koch, Simple shear flows of dense gas-solid suspension at finite Stokes numbers, *J. Fluid Mech*., 313, 309-341, 1996.

Savage, S.B., Granular flows at high shear rates, *in* Theory of dispersed multiphase flow, ed. R.E. Meyer, 339-358, *Academic Press*, 1983.

Savage, S.B., Instability of unbounded uniform granular shear flow, *J. Fluid Mech*., 241, 109-123, 1992.

Schaeffer, D.G., Instability in the evolution equations describing incompressible granular flow, *J. Diff. Equations*, 66, 19-50, 1987.
Schofield, A. and P. Wroth, Critical state soil mechanics, pp.310, *McGraw-Hill*, 1968.
Schumann, U., Subgrid scale model for finite difference simulations of turbulent flows in plane channels annuli, *J. Comput. Phys*., 18, 376-404, 1975.
Simonin, O., P. Fevrier, and J. Lavieville, On the spatial distribution of heavy-particle velocities in turbulent flow: from continuous field to particulate chaos, *J. Turbulence*, 3, 1-18, 2002.
Smagorinsky, J., General circulation experiments with the primitive equations: I. The basic experiment, *Mon. Weather Rev*., 91, 99-164, 1963.
Smagorinsky, J., Some historical remarks of the use of nonlinear viscosities, *in* Large Eddy simulation of complex engineering and geophysical flows, B. Galperin and S.A. Orszag eds. , 3-36, *Cambridge University Press*, 1993.
Sparks, R.S.J., Grain size variations in ignimbrites and implications for the transport of pyroclastic flows, *Sedimentology*, 23, 147-188, 1976.
Sparks, R.S.J., The dimension and dynamics of volcanic eruption columns, *Bull. Volcanol*., 48, 3-15, 1986.
Sursock, J.-P., Causality violation of complex-characteristic two-phase equations, *Int. J. Multiphase Flow*, 8, 291-295, 1982.
Syamlal, M., A Review of granular stress constitutive relations, pp. 23, *Topical Report U.S. Dept. of Energy*, DOE/MC/21353-2372, DE8700649, 1987.
Syamlal, M., W. Rogers, and T.J. O'Brien, MFIX documentation. Theory Guide, pp. 49, *U.S. Dept. of Energy*, DOE/METC-94/1004, DE94000097, 1993.
Syamlal, M., MFIX documentation. User's manual, pp. 87, *U.S. Dept. of Energy*, DOE/METC-95/1013, DE95000031, 1994.
Todesco, M., A. Neri, T. Esposti Ongaro, P. Papale, G. Macedonio, R. Santacroce, and A. Longo, Pyroclastic flow hazard assessment at Vesuvius (Italy) by using numerical modeling. I. Large-scale dynamics, *Bull. Volcanol*., 64, 155-177, 2002.
Tünzün, U.; G.T. Houlsby; R.M. Nedderman; and S.B. Savage, The flow of granular materials – II. Velocity distributions in slow flow, *Chem. Eng. Sc*., 37, 1691-1709, 1982.
Valentine, G.A., Stratified flow in pyroclastic surges, *Bull. Volcanol*., 49, 616-630, 1987.
Valentine, G.A., Eruption column physics, *in* From magma to tephra. Modeling physical processes of explosive volcanic eruptions, A. Freundt and M. Rosi (eds.), pp. 318, *Elsevier*, 1998.
Valentine, G.A. and K.H. Wohletz, Numerical models of plinian eruption columns and pyroclastic flows, *J. Geophys. Res*., 94, 1867-1887, 1989.
Valentine, G.A.; K.H. Wohletz; and S. Kieffer, Sources of unsteady column dynamics in pyroclastic flow eruptions, *J. Geophys. Res*., 96, 21887-21892, 1991.
Veitch, G. and A.W. Woods, Particle recycling and oscillations of volcanic eruption columns, *J. Geophys. Res*., 105, 2829-2942, 2000.
Weigand, B., J.R. Ferguson, and M.E. Crawford, An extended Kays and Crawford turbulent Prandtl number model, *Int. J. Heat mass Transfer*, 40, 4191-4196, 1997.
Wilson, L. and J.W. Head, Morphology and rheology of pyroclastic flows and their deposits, and guidelines for future observations, *in* The 1980 eruption of Mount St. Helens, Washington, P.W. Lipman and D.R. Mullineaux (eds.), 513-524, *U.S.G.S. professional paper 1250, Washington D.C*., 1981.
Wilson, C.J.N. and G.P.L. Walker, The Taupo eruption, New Zealand. I. General Aspects, *Phil. Trans. Royal Soc. London A*, 314, 199-228,1985.
Wood, B.D., Application of thermodynamics, 2nd ed., pp. 631, *Waveland Press*, 1991.
Woods, A.W., The fluid dynamics and the thermodynamics of eruption columns, *Bull. Volcanol*., 50, 169-193, 1988.
Woods, A.W. and K. Wohletz, Dimension and dynamics of co-ignimbrite eruption columns, *Nature*, 350, 225-227, 1991.
Woods, A.W. and S. Self, Thermal disequilibrium at the top of volcanic clouds and its effect on estimates of the column height, *Nature*, 355, 628-630, 1992.
Woods, A.W., Moist convection and the injection of volcanic ash into the atmosphere, *J. Geophys. Res*., 98, 17627-17636, 1993.
Yamamoto, Y.; M. Potthoff; T. Tanaka; T. Kajishima; and Y. Tsuji, Large-eddy simulation of turbulent gas-particle flow in a vertical channel: effect of considering inter-particle collisions, *J. Fluid Mech*., 442, 303-334, 2001.
Zehner, P. and E.U. Schlunder, Warmeleiftahigkeit von Schuttungen bei maβigen Temperaturen, *Chemie-Ingenieur-Technik*, 42, 933-941, 1970.

Appendix 1: Notations, units, constants, and acronyms

Latin

A_k		dimensionless	solid to gas phase molecular thermal conductibility coefficient ratio
B_k		dimensionless	solid to gas volumetric concentration function
c		m/s	instantaneous velocity vector
$\mathbf{c}_{12}$		m/s	instantaneous relative velocity of two colliding particles
$\mathbf{C}''$		m/s	fluctuating velocity vector
C_d		dimensionless	drag coefficient
C_g	0.33	dimensionless	gas phase Smagorinsky constant
C_s	0.044	dimensionless	solid phase Smagorinsky constant
Cp		J/kg K(m^2/s^2 K)	specific heat at constant pressure
Cv		J/kg K (m^2/s^2 K)	specific heat at constant volume
d		m	particle diameter
D		1/s	rate-of-strain tensor
e	0.9	dimensionless	inelasticity restitution coefficient
$E(k_\lambda)$		m^2/s^2	specific turbulent kinetic energy of the unresolved eddies over all k_λ
E_Θ		m^2/s^2	volume averaged granular fluctuating energy
f		s^3/m^6	velocity distribution function in the phase-space **r**,**c**
F		N/kg (m/s2)	all external forces per unit of mass acting on the particles
g_0		dimensionless	radial distribution function
G		Pa^2 (kg^2/m^2 s^4)	plastic potential function
g	(0,0,-9.80665)	m/s^2	sea level gravity vector
I		dimensionless	unit tensor
k		W/m K (kg m/K s^3)	thermal conductibility coefficient
k	(1,1,1)	dimensionless	unit vector along the line of centers between two colliding particles
K		kg/m^3 s	gas-solid momentum transfer (drag) function
k_λ		1/m	wave number scale of the largest unresolved turbulent eddies
m		kg	mass of grain
M_a	28.9644	kg/kmol	Molar weight of dry air
M_w	18.0152	kg/kmol	Molar weight of water
n		$1/m^3$	number of grains per unit of volume
Nu		dimensionless	Nusselt number
P		Pa (kg/m s^2)	Pressure (isotropic normal stress)
^{mol}Pr		dimensionless	"molecular" (not induced by turbulence) Prandtl number
^{tur}Pr	0.95	dimensionless	turbulent Prandtl number
q		1/Pa s (m s/kg)	plastic multiplier
q		kg/s^3	thermal-heat flux or granular-heat flux vector
r		m	position vector
Q		W/m^3 K (kg/s^3 K)	gas-solid heat transfer function
R	8314.56	J/kmol K (kg m^2/s^2 kmol K)	universal gas constant
$\tilde{R}$		J/kg K (m^2/s^2 K)	mixture gas constant
Re		dimensionless	particle Reynolds number
S		kg/m s^3	dissipation (net loss) of granular-temperature function
t		s	time
T		K	volume averaged temperature
T		Pa (kg/m s^2)	stress tensor
u		m/s	volume averaged velocity vectors
U_x		m/s	mean mixture horizontal/radial-speed of all phases
V_y		m/s	mean mixture vertical-speed of all phases
y		dimensionless	volume averaged of gas component mass fractions
Y		Pa^2 (kg^2/m^2 s^4)	plastic yield function

Greek

Δ		m	geometric mean of the computational grid-size
$\mathbf{\Delta}$		1/s	principal rate-of-strain tensor of the solid phase
ε		dimensionless	volume averaged volumetric concentration
$^{max}\varepsilon_s$	0.64	dimensionless	maximum solid volumetric concentration
$^{min}\varepsilon_s$	0.50	dimensionless	solid volumetric concentration at which friction starts
ε_E		m^2/s^3	turbulent energy cascade rate
ϕ_s	41	^{o} (degree)	angle of internal friction of the granular material
Φ		kg/m s^3	viscous dissipation
$^1\Phi_f$		dimensionless	first-order perturbation function from the Maxwellian state
Γ_k		dimensionless	function in the molecular effective multiphase heat conduction model
Γ_{slip}		kg/m s^3	production of granular-temperature function
η	0.95	dimensionless	function of the inelasticity restitution coefficient
λ		m	resolution length scale of the largest unresolved turbulent eddies
λ_s		Pa s (kg/m s)	solid phase second coefficient of viscosity
$\Lambda(k_\lambda)$		m^3/s^2	turbulent energy density or spectrum
μ		Pa s (kg/m s)	shear viscosity
μ^b		Pa s (kg/m s)	bulk viscosity
Θ		m^2/s^2	volume averaged granular-temperature
ρ		kg/m^3	microscopic weight density
$\hat{\rho}$		kg/m^3	volume averaged macroscopic weight density
ρ_m		kg/m^3	mean mixture weight density between all phases
$\boldsymbol{\sigma}$		Pa (kg/m s^2)	frictional principal stress tensor of the solid phase
$\boldsymbol{\tau}$		Pa (kg/m s^2)	viscous stress tensor
ϖ_k	$7.26\ 10^{-3}$	dimensionless	constant in the molecular effective multiphase heat conduction model
ϖ	$0<\varpi\leq1$	dimensionless	under-relaxation factor
ξ		dimensionless	granular-temperature conductivity adjustment function
Ψ			mean mixture value of a variable between all phases (speed, temperature)
ζ		dimensionless	granular shear viscosity adjustment function

Subscripts-Superscripts

’	after collision
″	fluctuating and turbulent
a	dry air
b	bulk viscosity
bd	granular bed
c	collisional transport only
dil	diluted ideal powder behavior
f	frictional transport
g	gas phase
k	kinetic transport only
k/c	kinetic and collisional
m	mixture
mol	“molecular” (i.e., not induced by turbulence)
s	solid phase
tur	induced by turbulence
x	X-direction (radial in Cylindrical or horizontal in Cartesian)
y	Y-direction (vertical)
w	water vapor (steam)

Acronyms

CV	control volume
FOU	first order upwinding
(G)MFIX	(geophysical) multiphase flow with interphase exchange
IMF	implicit multi-field
K-FIX	Kachina with fully implicit exchange
LANL	Los Alamos National Laboratory
LES	large eddy simulation
LHS	left-hand side
MFIX	multiphase flow with interphase exchange
MPI	message passing interface
NETL	National Energy Technology Laboratory
ORNL	Oak Ridge National Laboratory
PEA	partial elimination algorithm
PF	pyroclastic-flow
PL	plinian cloud
PS	pyroclastic-surge
RHS	right-hand side
SGH	sub-grid heat (flux)
SGS	sub-grid stress (flux)
SIMPLE	semi-implicit for pressure linked equations
SOR	successive over-relaxation

Appendix 2: Operators, tensors and invariants

Operators

$\triangleq$		deviatoric part (traceless) of a symmetric tensor
$\circ$		spherical part (trace) of a symmetric tensor
:		scalar product of two tensors
.		scalar product of two vectors
$\| \ \|$		Euclidian norm of a tensor
$\langle\rangle$		ensemble average
tr		trace operation of tensors
T		transposed operation of matrices
∇	1/m	gradient operator
$\nabla\cdot$	1/m	divergence operator

Some Tensors and Invariants

Rate-of-strain tensor:

$$\mathbf{D}=-\frac{1}{2}\left[\nabla\mathbf{u}+\nabla\mathbf{u}^{T}\right] \qquad \text{(A.1)} \qquad 1/s$$

Deviator of the rate-of-strain:

$$\mathring{\mathbf{D}}=\mathbf{D}+\frac{1}{3}\nabla\cdot\mathbf{u}\,\mathbf{I} \qquad \text{(A.2)} \qquad 1/s$$

First invariant of the rate-of-strain tensor:

$$I_D=\mathrm{tr}(\mathbf{D})=\sum_{i=1}^{3}D_{ii}=-\nabla\cdot\mathbf{u} \qquad \text{(A.3)} \qquad 1/s$$

Second invariant of the rate-of-strain tensor:

$$II_D=\mathrm{tr}(\mathbf{D}\cdot\mathbf{D})=\sum_{i=1}^{3}\sum_{j=1}^{3}D_{ij}D_{ji}=D_{11}^2+D_{22}^2+D_{33}^2+2D_{12}^2+2D_{13}^2+2D_{23}^2 \qquad \text{(A.4)} \qquad 1/s^2$$

Second invariant of the deviator of the stress tensor:

$$II_{dT}=\frac{\left(\sigma_1-\sigma_2\right)^2+\left(\sigma_2-\sigma_3\right)^2+\left(\sigma_3-\sigma_1\right)^2}{6} \qquad \text{a.}$$

$$II_{dT}=\frac{\left(\sigma_1-\langle\sigma\rangle\right)^2+\left(\sigma_2-\langle\sigma\rangle\right)^2+\left(\sigma_3-\langle\sigma\rangle\right)^2}{2} \qquad \text{b.}$$

$$II_{dT}=\frac{\sigma_1^2+\sigma_2^2+\sigma_3^2-\sigma_1\sigma_2-\sigma_2\sigma_3-\sigma_1\sigma_3}{3} \qquad \text{c.}$$

$$II_{dT}=\frac{\left(T_{11}-T_{22}\right)^2+\left(T_{22}-T_{33}\right)^2+\left(T_{33}-T_{11}\right)^2}{6}+T_{12}^2+T_{13}^2+T_{23}^2 \qquad \text{d.}$$

(A.5) Pa^2 ($\mathrm{kg}^2/\mathrm{m}^2\,\mathrm{s}^4$)

Second invariant of the deviator of the rate-of-strain tensor:

$$II_{dD}=\frac{\left(D_{11}-D_{22}\right)^2+\left(D_{22}-D_{33}\right)^2+\left(D_{33}-D_{11}\right)^2}{6}+D_{12}^2+D_{13}^2+D_{23}^2 \qquad \text{(A.6)} \qquad 1/s^2$$

Table, Figure, and Annex captions

Table 1

Hydrodynamic model.

Table 2

Interphase momentum and heat transfers.

Table 3

Thermodynamic material properties.

Table 4

Heat conductivity coefficients for a multiphase mixture. When only the gas phase is present, the effective molecular gas conductivity is simply equal to the molecular gas conductivity ($k_g \rightarrow k_{g,mol}$ when $\varepsilon_g \rightarrow 1$). The molecular heat conductivity coefficients are given in Table 3.

Table 5

Granular rheological model: kinetic-collisional granular stress, granular-temperature conductivity, 3D compressible yield function and plastic potential plastic stress models.

Table 6

General stress formulation for the gas and solid phase: Large eddy-simulation model for the gas phase, and the kinetic-collisional-frictional model for the solid phase. If the dispersed phase is very diluted within a flow dominated by the gas phase turbulence and made of small particles (<< 100 μm), a simple LES model is chosen for the solid phase.

Figure 4

Transport of a quantity ϕ (mass, momentum, energy) between time t and t+dt within the dispersed phase for kinetic, collisional and kinetic, and frictional regimes.

Figure 5

Dissipation principles of energy within a fluidized granular medium. In the gas phase, viscous effects dissipate the bulk mechanical energy of the flow into heat, while in granular media, there is an intermediate state in the dissipation process: the production of granular-temperature mostly by viscous dissipation and the dissipation of granular-temperature into heat mostly by inelastic collision between grains.

Figure 6

Geometrical configuration of two colliding particles moving at velocities $\mathbf{c}_{s,1}$ and $\mathbf{c}_{s,2}$ and at position $\mathbf{r}_1$ and $\mathbf{r}_2$. Both particles have the same diameter, d. $\mathbf{k}$ is a unit vector along the line of center from particle 1 to particle 2.

Figure 7

A. Granular-temperature, Θ; **B**. granular shear viscosity; **C**. and granular pressure vs. volumetric grain concentration for different pyroclastic-flow simulations, including those shown in the companion paper [*Dartevelle et al., 2003*]. For a given concentration, the higher Θ, the higher the granular pressure and viscosities. In the very diluted limit ($\varepsilon_s << 10^{-4}$ vol.%), Θ is high owing to the large unbounded mean free path of grains. At higher concentrations, Θ decreases as inelastic collisions become more and more predominant; therefore, this effect causes a decrease of granular shear viscosities. It is interesting to note that the head of the flow (opened diamonds) generally present higher granular-temperatures than its body (closed triangles) owing to a higher rate-of-strain (by at least a factor 10), hence a higher viscous dissipation (source of Θ). Consequently, for a given granular concentration, the head of the flow has higher granular shear kinetic-collisional viscosities than its body. In the predominantly collisional regime ($1 < \varepsilon_s < 50$ vol.%), Θ drops to low values. However, the shear viscosity is barely decreased owing to g_0, which increases with ε_s; hence prevents the granular shear viscosity from going to zero (see Eq.(T5.4) and Eq.(T5.9)). At very high concentrations ($\varepsilon_s > 50$ vol.%), frictions begin, which is followed by an exponential increase of granular viscosities and pressure. At those concentrations, Θ drops to negligible values as the mean free path is reduced to zero (i.e., "frozen" granular body). For understanding this figure in terms of pyroclastic-flow and -surge dynamics, see the companion paper [*Dartevelle et al., 2003*].

Figure 8

Domain of no-deformation (rigid) and domain of plastic deformation (which is the envelope of the yield function). Theoretically, the inside domain can represent the elastic deformation, however, for most of granular materials, elastic strain is negligible, and this inner domain can be assumed as perfectly rigid. The central axis on which the principal stresses are equal represents the hydrostatic pressure. **A**. Two-dimensional Mohr-Coulomb yield lines in the principal stress plane. Plastic dilatancy deformation occurs, at yield, on those two lines. **B**. Three-dimensional extended von Mises yield surface in the principal stress space. Plastic dilatancy deformation occurs, at yield, on the surface of this cone. **C**. Three-dimensional modified von Mises yield function accounting for compressibility effects: failure (dilatancy), consolidation and critical state. One apex of this function lies at the origin (as for the extended von Mises yield function) and the second apex lies at $\langle\sigma\rangle = 2^f P$. The circle [cc'] represents the critical state domain on this yield surface where no change of volume occurs. The critical state is where the normal vector on the yield surface is orthogonal to the hydrostatic axis , whereas when the normal to the yield curve has a positive projection on the hydrostatic axis, we have a dilatancy (decrease of bulk density), and when the projection is negative a contractancy phenomenon (increase of the bulk density). Notice that in the Mohr-Coulomb (**A**.) and extended von Mises cases (**B**.), the projection is always positive upon the hydrostatic axis, hence those two yield functions only predict unbounded, continued expansion.

Annex 4

Development of constitutive equations of the effective molecular (i.e., not turbulent) heat conductivity model for interpenetrated phases from *Zehner and Schlunder* [*1970*]. Se also Table 4.

Table 1:

Continuity

Gas

$$\frac{\partial \hat{\rho}_g}{\partial t} = -\nabla \cdot \hat{\rho}_g \mathbf{u}_g \tag{T1.1}$$

Gas species dry-air: $$\frac{\partial y_a \hat{\rho}_g}{\partial t} = -\nabla \cdot y_a \hat{\rho}_g \mathbf{u}_g \tag{T1.2}$$

Gas species water vapor: $$\frac{\partial y_w \hat{\rho}_g}{\partial t} = -\nabla \cdot y_w \hat{\rho}_g \mathbf{u}_g \tag{T1.3}$$

Solid

$$\frac{\partial \hat{\rho}_s}{\partial t} = -\nabla \cdot \hat{\rho}_s \mathbf{u}_s \tag{T1.4}$$

Momentum

Gas

$$\frac{\partial \hat{\rho}_g \mathbf{u}_g}{\partial t} + \nabla \cdot \left(\hat{\rho}_g \mathbf{u}_g \mathbf{u}_g \right) = -K \left(\mathbf{u}_g - \mathbf{u}_s \right) - \varepsilon_g \nabla P_g - \nabla \cdot \left(\varepsilon_g \boldsymbol{\tau}_g \right) + \hat{\rho}_g \mathbf{g} \tag{T1.5}$$

Solid

$$\frac{\partial \hat{\rho}_s \mathbf{u}_s}{\partial t} + \nabla \cdot \left(\hat{\rho}_s \mathbf{u}_s \mathbf{u}_s \right) = +K \left(\mathbf{u}_g - \mathbf{u}_s \right) - \varepsilon_s \nabla P_s - \nabla \cdot \left(\varepsilon_s \boldsymbol{\tau}_s \right) + \varepsilon_s \left(\rho_s - \rho_g \right) \mathbf{g} \tag{T1.6}$$

Energy

Gas

$$\hat{\rho}_g C v_g \left[\frac{\partial T_g}{\partial t} + \mathbf{u}_g \cdot \nabla T_g \right] = -\nabla \cdot \mathbf{q}_{g,\,eff} + Q \left(T_s - T_g \right) + K \left(\mathbf{u}_g - \mathbf{u}_s \right)^2 - P_g \left[\frac{\partial \varepsilon_g}{\partial t} + \nabla \cdot \varepsilon_g \mathbf{u}_g \right] \tag{T1.7}$$

Solid

$$\hat{\rho}_s C v_s \left[\frac{\partial T_s}{\partial t} + \mathbf{u}_s \cdot \nabla T_s \right] = -\nabla \cdot \mathbf{q}_{s,\,eff} - Q \left(T_s - T_g \right) \tag{T1.8}$$

Granular-temperature (fluctuating energy)

$$\left[\frac{\partial \hat{\rho}_s E_\Theta}{\partial t} + \nabla \cdot \hat{\rho}_s E_\Theta \mathbf{u}_s \right] = \Phi - P_s \nabla \cdot \mathbf{u}_s - \nabla \cdot \mathbf{q}_\Theta + \Gamma_{slip} - S_{coll} - S_{drag} \tag{T1.9}$$

Table 2:

Momentum Interphase Transfer Coefficients

Drag for dilute suspension ($\varepsilon_g > 0.8$)	Drag for concentrated suspension ($\varepsilon_g \le 0.8$)
$K = \frac{3}{4}\frac{\varepsilon_s}{\varepsilon_g} C_d \frac{\hat{\rho}_g \left\lvert \mathbf{u}_g - \mathbf{u}_s \right\rvert}{d} \varepsilon_g^{-2.65}$ (T2.1)	$K = \frac{\varepsilon_s}{\varepsilon_g}\left[150 \frac{\varepsilon_s}{\varepsilon_g} \frac{{}^{mol}\mu_g}{d^2} + \frac{7}{4} C_d \rho_g \frac{\left\lvert \mathbf{u}_g - \mathbf{u}_s \right\rvert}{d} \right]$ (T2.2)

Drag coefficient

$$C_d = \frac{24}{Re}\left[1 + 0.15\,Re^{0.687}\right] \quad \text{for } Re < 1000$$
$$C_d = 0.44 \quad \text{for } Re \ge 1000 \qquad \text{(T2.3)}$$

Heat Interphase Transfer Coefficients

$$Q = \frac{6\,\varepsilon_s\,{}^{mol}k_g}{d^2} Nu \qquad \text{(T2.4)}$$

Particle Reynolds number

$$Re = \frac{\hat{\rho}_g d \left\lvert \mathbf{u}_g - \mathbf{u}_s \right\rvert}{{}^{mol}\mu_g} \qquad \text{(T2.5)}$$

Nusselt Number Nu

$$Nu = \left(7 - 10\,\varepsilon_g + 5\,\varepsilon_g^2\right)\left(1 + \frac{7}{10} Re^{7/10}\,{}^{mol}Pr^{1/3}\right) + \left(1.33 - 2.4\,\varepsilon_g + 1.2\,\varepsilon_g^2\right) Re^{7/10}\,{}^{mol}Pr^{1/3} \qquad \text{(T2.6)}$$

"Molecular" Prandtl Number

$${}^{mol}Pr = \frac{C_{pg}\,{}^{mol}\mu_g}{{}^{mol}k_g} \qquad \text{(T2.7)}$$

Table 3:

Specific heat of dry air and water at constant pressure

Cp_a $4183.9\left(0.251625-9.2525\times10^{-5}T_g+2.1334\times10^{-7}T_g^2-1.0043\times10^{-10}T_g^3\right)$ (T3.1)

Cp_w $4183.9\left(0.452219-1.29224\times10^{-4}T_g+4.17008\times10^{-7}T_g^2-2.00401\times10^{-10}T_g^3\right)$ (T3.2)

Specific heat of solid at constant volume

Cv_s 954 (T3.3)

Molecular conductivity coefficient of gas and solid phases

$^{mol}k_g$ $1\times10^{-10}\left(60054+1846\,T_g+2\times10^{-6}\,T_g^2\right)$ (T3.4)

$^{mol}k_s$ 2.2 (T3.5)

Table 4:

Effective heat conduction

Gas phase	Solid phase
$\mathbf{q}_{g,\,eff} = -\left({}^{mol}k_{g,eff} + {}^{tur}k_g \right) \nabla T_g$ (T4.1)	$\mathbf{q}_{s,\,eff} = -\left({}^{mol}k_{s,eff} + {}^{tur}k_s \right) \nabla T_s$ (T4.2)

Molecular heat conduction

Molecular effective conductivity	Granular effective conductivity
${}^{mol}k_{g,eff} = \left(1 - \sqrt{\varepsilon_s}\right) {}^{mol}k_g$ (T4.3)	${}^{mol}k_{s,eff} = \sqrt{\varepsilon_s} \left[\omega_k A_k + \left(1 - \omega_k\right) \Gamma_k \right] {}^{mol}k_g$ (T4.4)

$$\Gamma_k = -\frac{2}{\left(1 - \frac{B_k}{A_k}\right)} \left[\frac{A_k - 1}{\left(1 - \frac{B_k}{A_k}\right)^2} \frac{B_k}{A_k} \ln\left(\frac{B_k}{A_k}\right) + \frac{B_k - 1}{\left(1 - \frac{B_k}{A_k}\right)} + \frac{B_k + 1}{2} \right] \quad \text{(T4.5)}$$

$$A_k = \frac{{}^{mol}k_s}{{}^{mol}k_g} \quad \text{(T4.6)}$$

$$B_k = \frac{5}{4} \left(\frac{\varepsilon_s}{\varepsilon_g} \right)^{10/9} \quad \text{(T4.7)}$$

$$\omega_k = 7.26\ 10^{-3} \quad \text{(T4.8)}$$

Turbulent heat conduction

Turbulent conductivity	Turbulent conductivity
${}^{tur}k_g = \varepsilon_g \frac{Cp_g}{{}^{tur}Pr} {}^{tur}\mu_g$ (T4.9)	${}^{tur}k_s = \varepsilon_s \frac{Cp_g}{{}^{tur}Pr} {}^{tur}\mu_s$ (T4.10)

Table 5:

Granular kinetic-collisional stress

Total kinetic-collisional stress tensor

$$ {}^{k/c}\mathbf{T} = {}^{k}\mathbf{T} + {}^{c}\mathbf{T} = {}^{k/c}\mathrm{P}\,\mathbf{I} + {}^{k/c}\boldsymbol{\tau} \tag{T5.1} $$

Kinetic-collisional pressure

$$ {}^{k/c}\mathrm{P} = \hat{\rho}_s \Theta \left(1 + 4\varepsilon_s g_0 \eta\right) \tag{T5.2} $$

Kinetic -collisional viscous stress tensor

$$ {}^{k/c}\boldsymbol{\tau} = -{}^{c}\mu^{b}\, \nabla \cdot \mathbf{u}_s\, \mathbf{I} + 2\ {}^{k/c}\mu\ \stackrel{\circ}{=}{\mathbf{D}}_s \tag{T5.3} $$

Kinetic-collisional shear viscosity

$$ {}^{k/c}\mu = \frac{\zeta}{\eta\left(2-\eta\right)}\mu^{dil} \tag{T5.4} $$

Collisional bulk viscosity

$$ {}^{c}\mu^{b} = \frac{256}{5\pi}\eta\,\varepsilon_s^2\, g_0\, \mu^{dil} = \frac{8}{3\sqrt{\pi}}\,d\,\rho_s\,\varepsilon_s^2\, g_0\,\eta\sqrt{\Theta} \tag{T5.5} $$

Dilute ideal powder viscosity

$$ \mu^{dil} = \frac{5\sqrt{\pi}}{96}\,d\,\rho_s\,\sqrt{\Theta} \tag{T5.6} $$

Granular-temperature conduction

Total kinetic-collisional granular-temperature conduction

$$ \mathbf{q}_\Theta = -\left({}^{k}\kappa_\Theta + {}^{c}\kappa_\Theta\right)\nabla\Theta = -{}^{k/c}\kappa_\Theta \nabla\Theta \tag{T5.7} $$

Kinetic -collisional granular-temperature conductivity coefficient

$$ {}^{k/c}\kappa_\Theta = \frac{30\ \xi}{\eta\left(41-33\eta\right)}\mu_s^{dil} \tag{T5.8} $$

Table 5 (cont.)

Granular kinetic-collisional functions

Granular shear viscosity adjustment function

$$\zeta = \frac{1}{g_0} + \frac{8\eta\varepsilon_s}{5}\left(3\eta - 1\right) + \frac{64}{25\pi}\eta^2\,\varepsilon_s^2\,g_0\left[3\eta\left(\pi - 4\right) + 2\left(12 - \pi\right)\right] \tag{T5.9}$$

Granular-temperature conductivity adjustment function

$$\xi = \frac{1}{g_0} + \frac{12\eta\varepsilon_s}{5}\left[\left(2\eta - 1\right)^2 + \eta\right] + \frac{48}{25}\eta^2\,\varepsilon_s^2\,g_0\left[3\eta\left(4\eta - 3\right) + \frac{4}{3\pi}\left(41 - 33\eta\right)\right] \tag{T5.10}$$

Kinetic-collisional viscous dissipation

$$\Phi = 2\,{}^{k/c}\mu\,\mathrm{tr}(\mathbf{D}_s \cdot \mathbf{D}_s) + {}^{k/c}\lambda_s\,\mathrm{tr}^2(\mathbf{D}_s) \tag{T5.11}$$

Granular-temperature production through the slip

$$\Gamma_{slip} = \frac{81\,\varepsilon_g{}^{mol}\mu_g^2\left|\mathbf{u}_g - \mathbf{u}_s\right|^2}{g_0\,\rho_s\,d^3\sqrt{\pi\,\Theta}} \tag{T5.12}$$

Granular-temperature dissipation through inelastic collisions

$$S_{coll} = \frac{48\,\eta\,\varepsilon_s\,\hat{\rho}_s\,g_0\,\sqrt{\pi}}{\pi\,d}\left(1 - \eta\right)\sqrt{\Theta^3} \tag{T5.13}$$

Granular-temperature dissipation through the drag

$$S_{drag} = 3\,K\,\Theta \tag{T5.14}$$

Inelastic function

$$\eta = \frac{1 + e}{2} \tag{T5.15}$$

2nd coefficient of viscosity

$${}^{k/c}\lambda_s = {}^{c}\mu^{b} - \frac{2}{3}\,{}^{k/c}\mu \tag{T5.16}$$

Table 5 (cont.)

Visco-plastic model

Frictional stress

$$ {}^{f}\mathbf{T} = {}^{f}P\mathbf{I} + {}^{f}\boldsymbol{\tau} = {}^{f}P\mathbf{I} + \left[-{}^{f}\mu^{b}\ \nabla\cdot\mathbf{u}_{s}\,\mathbf{I} + 2\ {}^{f}\mu\ \overset{\circ}{\underline{\underline{\mathbf{D}}}}_{s} \right] \tag{T5.17} $$

Yield function

$$ Y \equiv II_{dT} + \left(\left\langle \sigma \right\rangle^{2} - 2\ \left\langle \sigma \right\rangle\ P \right)\ \sin^{2}\ \phi_{s} = 0 \tag{T5.18} $$

Normal plastic pressure (EOS of frictional granular materials)

$$ {}^{f}P = 1000\,\frac{\left(\varepsilon_{s} - {}^{min}\varepsilon_{s} \right)^{3}}{\left({}^{max}\varepsilon_{s} - \varepsilon_{s} \right)^{3}} \tag{T5.19} $$

Frictional shear viscosity

$$ {}^{f}\mu = \frac{{}^{f}P\ \sin^{2}\ \phi_{s}}{\sqrt{4\ \sin^{2}\ \phi_{s}\ \ II_{dD} + \left(\nabla\cdot\mathbf{u}_{s} \right)^{2}}} \tag{T5.20} $$

Frictional bulk viscosity

$$ {}^{f}\mu^{b} = \frac{{}^{f}P}{\sqrt{4\ \sin^{2}\ \phi_{s}\ \ II_{dD} + \left(\nabla\cdot\mathbf{u}_{s} \right)^{2}}} \tag{T5.21} $$

Frictional volumetric concentration range

From ${}^{min}\varepsilon_{s}$=0.5 to ${}^{max}\varepsilon_{s}$=0.64

Table 6:

Gas stress

Total gas stress tensor

$$\mathbf{T}_g = P_g \mathbf{I} + \boldsymbol{\tau}_g \tag{T6.1}$$

Molecular and turbulent Stress (shear only)

$$\boldsymbol{\tau}_g = 2\,\mu_{g,\mathrm{eff}}\,\overset{\circ}{\underline{\underline{\mathbf{D}}}}_g = 2\,\mu_{g,\mathrm{eff}}\left[\mathbf{D}_g + \frac{1}{3}\left(\nabla\cdot\mathbf{u}_g\right)\mathbf{I}\right] \tag{T6.2}$$

Effective gas viscosity

$$\mu_{g,\mathrm{eff}} = {}^{\mathrm{mol}}\mu_g + {}^{\mathrm{tur}}\mu_g \tag{T6.3}$$

Molecular gas viscosity

$${}^{\mathrm{mol}}\mu_g = 1.7\times10^{-5}\left[\left(\frac{T_g}{273}\right)^{1.5}\frac{383}{T_g+110}\right] \tag{T6.4}$$

Turbulent gas viscosity (Static LES model)

$${}^{\mathrm{tur}}\mu_g = \frac{\left(C_g\,\Delta\right)^2}{\sqrt{2}}\rho_g\left\|\overset{\circ}{\underline{\underline{\mathbf{D}}}}_g\right\| \tag{T6.5}$$

Solid stress

Total solid stress tensor

$$\mathbf{T}_s = P_s\,\mathbf{I} + \boldsymbol{\tau}_s \tag{T6.6}$$

Total viscous solid stress

$$\boldsymbol{\tau}_s = -\mu_s^b\,\nabla\cdot\mathbf{u}_s\,\mathbf{I} + 2\,\mu_s\,\overset{\circ}{\underline{\underline{\mathbf{D}}}}_s \tag{T6.7}$$

$10^{-4}<\varepsilon_s<64$ vol.%	$\varepsilon_s<10^{-3}$ vol.%
Pyroclastic-flows and -surges	Plinian clouds
$P_s = {}^{k/c}P + {}^{f}P$ (T6.8)	$P_s = 0$ (T6.11)
$\mu_s^b = {}^{k/c}\mu^b + {}^{f}\mu^b$ (T6.9)	$\mu_s^b = 0$ (T6.12)
$\mu_s = {}^{\mathrm{tur}}\mu_s + {}^{f}\mu = {}^{k/c}\mu + {}^{f}\mu$ (T6.10)	$\mu_s = {}^{\mathrm{tur}}\mu_s = \frac{\left(C_s\,\Delta\right)^2}{\sqrt{2}}\rho_s\left\|\overset{\circ}{\underline{\underline{\mathbf{D}}}}_s\right\|$ (T6.13)

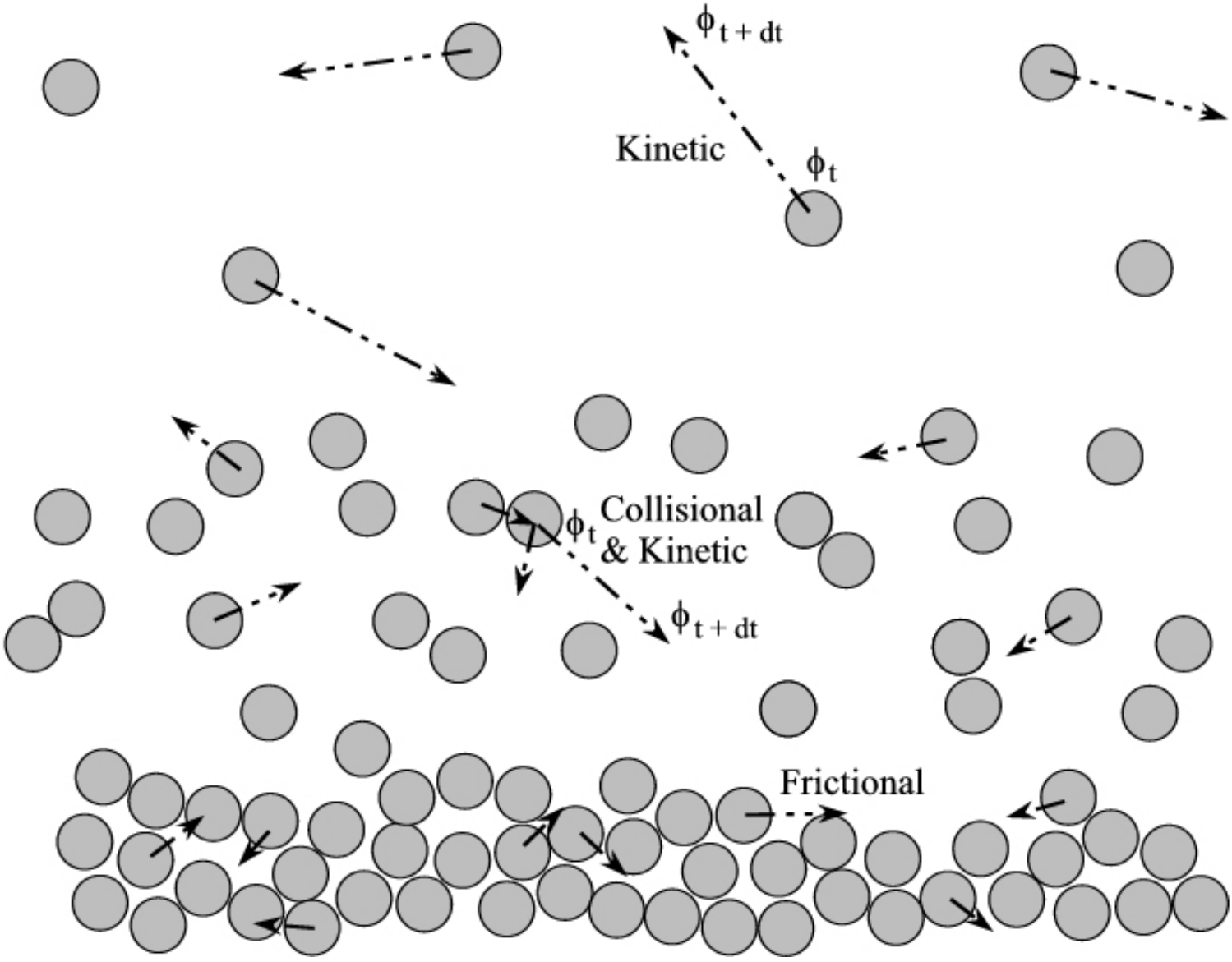
ϕ_{t+dt}
Kinetic
ϕ_t
ϕ_t
Collisional
& Kinetic
ϕ_{t+dt}
Frictional

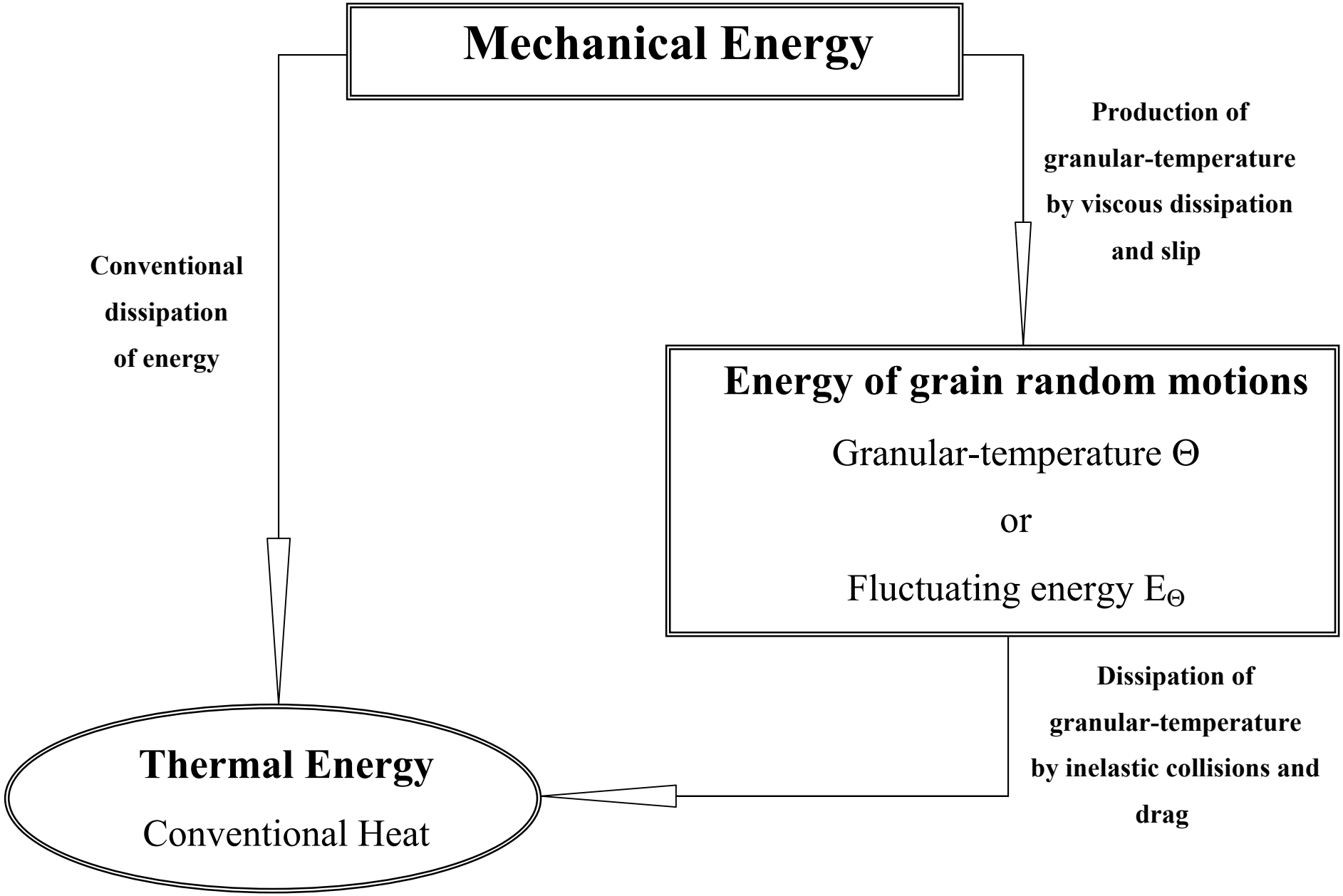
Mechanical Energy
Production of granular-temperature by viscous dissipation and slip
Conventional dissipation of energy
Energy of grain random motions
Granular-temperature Θ
or
Fluctuating energy E_Θ
Dissipation of granular-temperature by inelastic collisions and drag
Thermal Energy
Conventional Heat

Chapter 2 - Figure 6

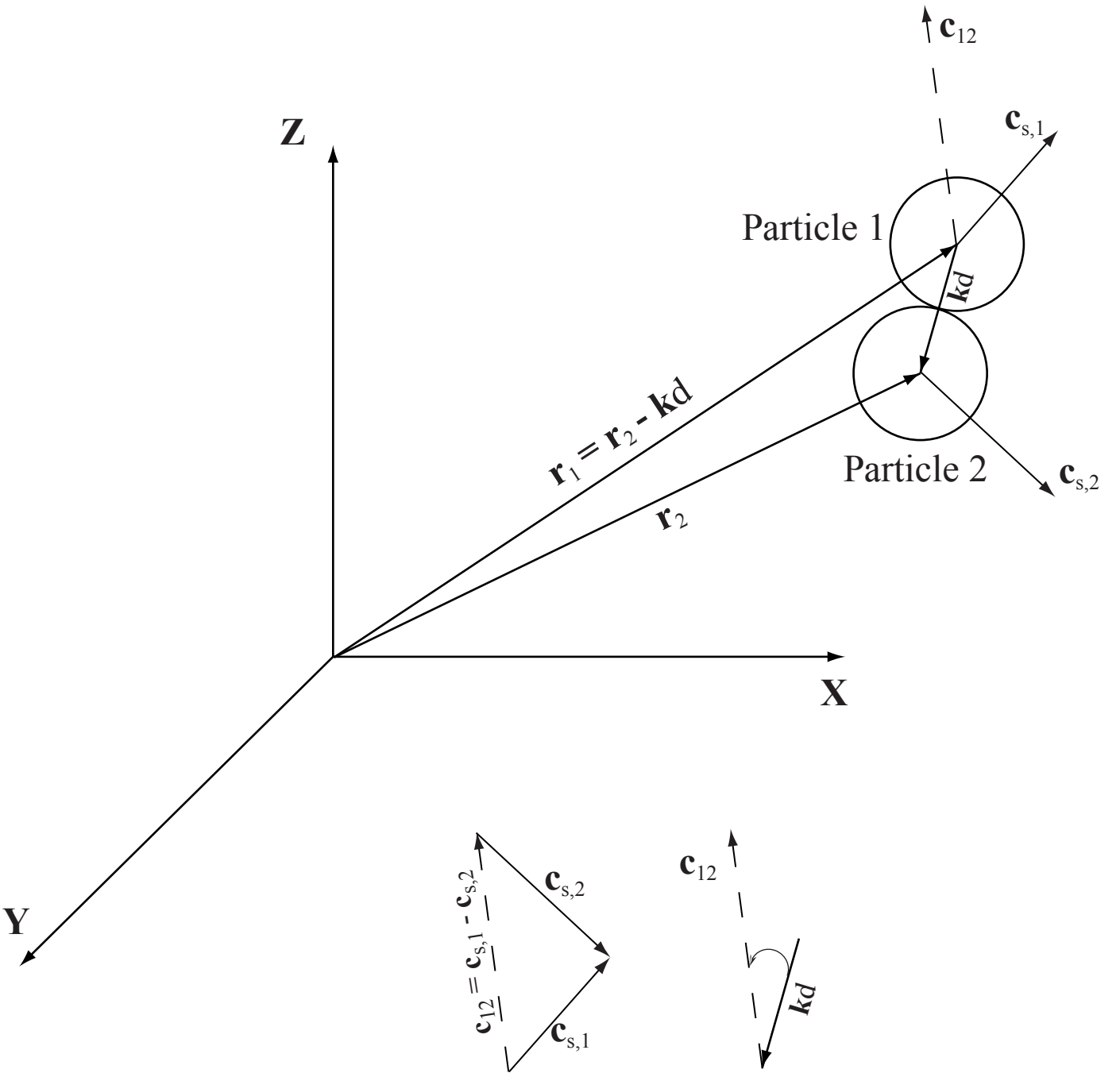

▲ = within the body of the flow (10s - 480s)

◇ = head of the flow (10s - 100s)

Chapter 2 - Figure 7

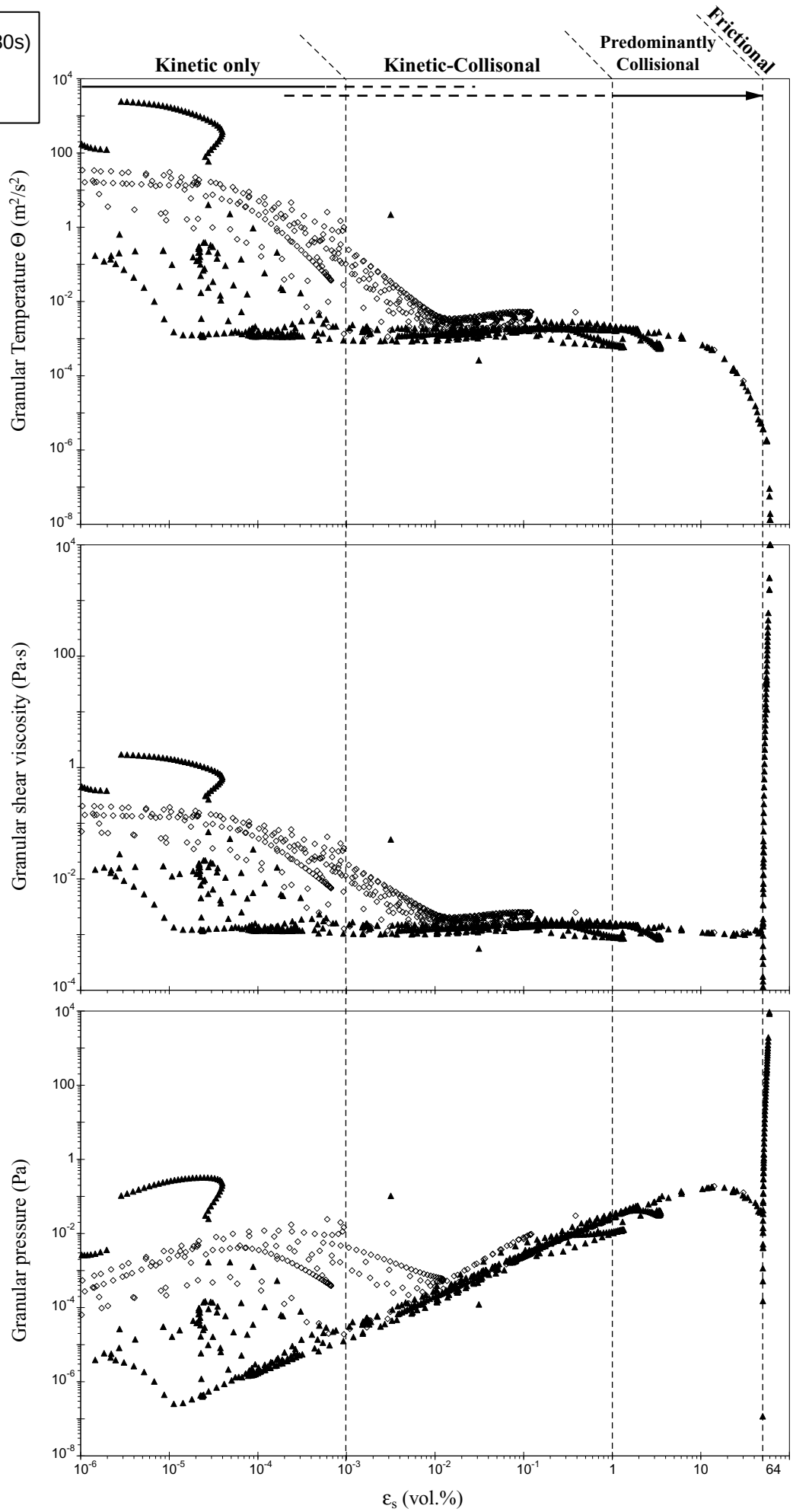

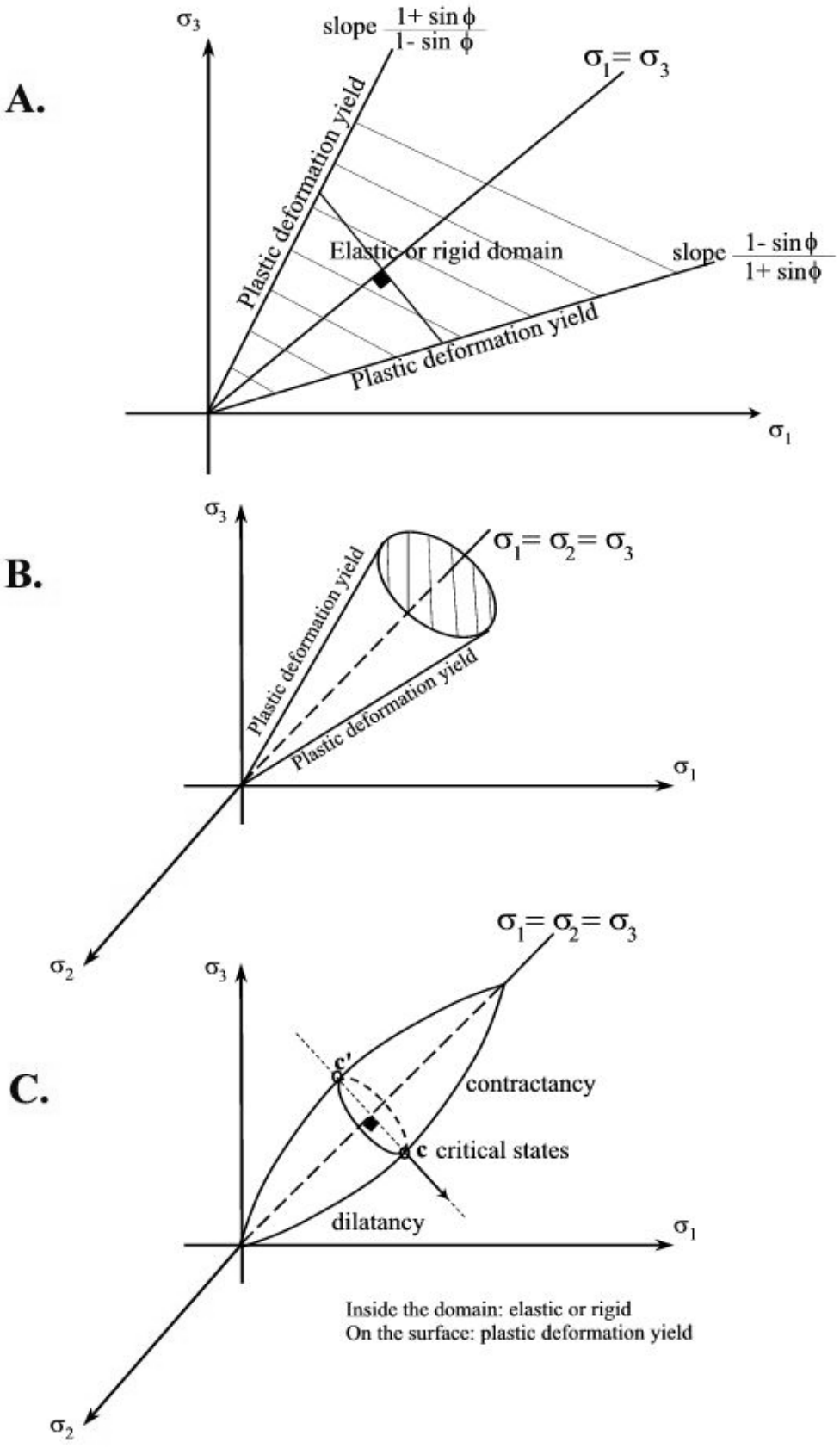
A.
σ3
slope 1+ sin ϕ / 1- sin ϕ
σ1= σ3
Plastic deformation yield
Elastic or rigid domain
slope 1- sin ϕ / 1+ sin ϕ
Plastic deformation yield
σ1
B.
σ3
σ1= σ2= σ3
Plastic deformation yield
Plastic deformation yield
σ1
σ2
C.
σ1= σ2= σ3
σ3
c'
contractancy
c critical states
dilatancy
σ1
σ2
Inside the domain: elastic or rigid
On the surface: plastic deformation yield

Chapter 2 – Annex 4:

Specification of the effective molecular (non-turbulent) heat conductivities for an interpenetrated multiphase system

The *Zehner and Schlunder* [*1970*]'s heat conductivity model was initially developed for estimating the effective radial thermal conductivity in packed granular bed, but can be generalized to fluidized bed as well [e.g., *Kuipers et al, 1992*]. According to this model, the radial thermal bed conductivity coefficient (k_{bd}) can be expressed as a contribution due to the gas phase only ($k_{bd,g}$), and a contribution due to a combination of the gas and solid phases ($k_{bd,g/s}$):

$$\mathbf{q}_{bd} = -k_{bd}\,\nabla T_{bd} = -(k_{bd,g} + k_{bd,g/s})\,\nabla T_{bd} \tag{1}$$

where $\mathbf{q}_{bd}$ is the heat vector flux of the bulk bed temperature (T_{bd}), and

$$\begin{aligned} k_{bd,g} &= \left(1-\sqrt{\varepsilon_s}\right)\,{}^{mol}k_g \\ k_{bd,g/s} &= \sqrt{\varepsilon_s}\left[\varpi_k A_k + \left(1-\varpi_k\right)\Gamma_k\right]\,{}^{mol}k_g \end{aligned} \tag{2}$$

ω_k, A_k, given in Table 4, are for spherical particles only [*Zehner and Schlunder, 1970; Kuipers et al, 1992*], see Table 3 for the molecular conductivities and Table 4 for the Γ_k function.

According to Eq.(2), if $\varepsilon_s \to 0$ (no grain, only gas), then $k_{bd,g} \to {}^{mol}k_g$ and $k_{bd,g/s} \to 0$ as expected. Defining the total "molecular" (i.e., not induced by turbulence) effective multiphase (mixture) conductivity as:

$${}^{mol}\mathbf{q}_{tot} = {}^{mol}\mathbf{q}_g + {}^{mol}\mathbf{q}_s = -\left({}^{mol}k_{g,eff}\,\nabla T_g + {}^{mol}k_{s,eff}\,\nabla T_s\right) \tag{3}$$

Eq.(1) and Eq.(3) can be solved together to find a solution for both ${}^{mol}k_{g,eff}$ and ${}^{mol}k_{s,eff}$ at $T_{bd}=T_g=T_s$ [*Kuipers et al, 1992*]:

$$k_{bd} = {}^{mol}k_{g,eff} + {}^{mol}k_{s,eff} \tag{4}$$

and comparing Eq.(1) with Eq.(4), we can find the effective thermal conductivities for the gas and solid phases:

$$^{mol}k_{g,eff} = \left(1 - \sqrt{\varepsilon_s}\right)\, ^{mol}k_g \tag{5}$$

$$^{mol}k_{s,eff} = \sqrt{\varepsilon_s}\, \left[\omega_k A_k + \left(1 - \omega_k\right)\Gamma_k\right]\, ^{mol}k_g \tag{6}$$

where $^{mol}k_{s,eff} \rightarrow 0$ and $^{mol}k_{g,eff} \rightarrow ^{mol}k_g$ whenever $\varepsilon_s \rightarrow 0$ (only gas phase) and $^{mol}k_{s,eff} << ^{mol}k_s$ for any ε_s. Hence this model properly modifies the thermal conductivity in accounting for the presence of more than one phase.

Chapter 3.

Numerical Modeling of Geophysical Granular Flows: Part II. Computer Simulations of Plinian Clouds, Pyroclastic Flows and Surges

Keywords: Plinian cloud, granular gravity currents, pyroclastic-surge, pyroclastic-flow, granular rheology, kinetic, collisional, frictional, plastic.

"*Thinking is more interesting than knowing,*
but less interesting than looking."

Johan Wolfgang von Goethe (1749-1832).

Abstract

Geophysical granular flows display complex nonlinear, non-uniform, and unsteady rheologies depending on the volumetric grain concentration within the flow: kinetic, kinetic-collisional, and frictional. To account for the whole spectrum of granular rheologies (hence concentrations), we have used and further developed for geophysical-atmospherical applications a multiphase computer model initially developed by U.S. Department of Energy laboratories: (**G**eophysical) **M**ultiphase **F**low with **I**nterphase e**X**change. As demonstrated in this manuscript, (G)MFIX can successfully simulate a large span of pyroclastic phenomena and related processes: plinian clouds, pyroclastic-flows, -surges, flow transformations and depositional processes. Plinian cloud simulations agree well with classical plume theory and historical eruptions in the upper altitude of the cloud (H_T) vs. mass flux diagram. For high mass flux ($>10^7$ kg/s), plinian clouds pulsate periodically with time because of the vertical propagations of acoustic-gravity waves within the clouds. The lowest undercooled temperature anomalies measured within the upper part of the column can be as low as -18 K, which agrees well with El Chichón and Mt. St. Helens eruptions. Vertical- and horizontal-speed profiles within the plinian cloud compare well with those inferred from simple plume models and from umbrella experiments. Pyroclastic-flow and -surge simulations show that both end-member are closely tight together, e.g., an initially diluted flow may generate a denser basal underflow which will eventually outrun the expanded head of the flow. We further illustrate evidences of vertical and lateral flow transformation processes between diluted and concentrated flows, particularly laterally from a turbulent "maintained over-time fluidized zone" near source. Our comprehensive granular rheological model and our simulations demonstrate that the main depositional process is mainly a progressive vertical aggradation fed from either overlying surges or from upstream concentrated (frictional) pyroclastic-flows. In this manuscript, we further develop the concepts of pyroclastic-flows and surges in the lights of classical granular rheologies.

1. Introduction

In the companion paper, *Dartevelle* [*2003b*] has shown that it is possible to mathematically formulate granular viscous dissipation effects due to the turbulent kinetic motions of grains (i.e., free flights), inelastic collisions between grains of same size, and frictions. Two granular rheological models are used: a rate-of-strain dependent for the kinetic and kinetic-collisional behavior (i.e., fluidized granular flows) and a rate-of-strain independent for high concentration frictional-plastic granular flows. Both models are unified through a unique stress tensor for the granular phase [*Dartevelle, 2003b*]. As demonstrated herewith, multiphase flow models within the Implicit MultiField formalism [e.g., *Harlow and Amsden, 1975; Ishii, 1975; Rivard and Torrey, 1977*] and with the granular model from *Dartevelle* [*2003b*] can successfully simulate a large spectrum of pyroclastic phenomena (e.g., plinian and coignimbrite clouds, pyroclastic-surges, -flows, and -deposits), flow transformation processes, and depositional processes.

The objectives of this manuscript are threefold. First, we introduce a multiphase computer code, (G)MFIX, able to solve the hydrodynamic model presented in the companion paper and used herewith to simulate pyroclastic phenomena. Second, we present and discuss three plinian cloud simulations which are compared with previous observations and plume theory. Third, we present three pyroclastic-surge and -flow simulations formed by fountain collapse and discuss those simulations in terms of flow transformations and depositional processes.

Overall, we focus on multiphase aspects not yet modeled previously and currently subject to debates in volcanology, which are abridged as follow:

1- Are numerical multiphase models able to simulate a complete and stable plinian cloud (i.e., column and umbrella) over a long period of time into the atmosphere [e.g., *Sparks et al., 1997*]? This task is difficult as it requires powerful computers able to work in parallel with *ad hoc* parallelized codes. The ability to properly simulate plinian clouds also depends on the global resolution (i.e., grid-size) and the exact turbulence formulation. Our plinian cloud simulations compare well with the classical *Morton et al.*'s theory [*1956*] and with real observations [e.g., *Wilson et al., 1978; Holasek et al., 1995; Holasek et al., 1996*]. We also focus on the growth of plinian clouds into the atmosphere and demonstrate a well-known unsteady pulsating behavior of the plume. This pulsating behavior is compared in terms of temperature anomalies at the top of the cloud. We discuss further the implications in terms of fallout deposits and remote-sensing techniques.

2- Are pyroclastic-flows expanded or concentrated? In other words, how do pyroclastic-flows move [e.g., *Cas and Wright, 1988; Druitt, 1998; Freundt and Bursik, 1998; Calder et al., 2000*]? This question has never been answered by previous theoretical models as they only consider one end-member of the concentration spectrum at the time (dilute or concentrated), hence imposing *a priori* the concentration to be expected in the flow. Since (G)MFIX has a complete granular rheological model that can deal with any possible grain volumetric concentrations, we revisit in the light of classical granular theories the concepts of "pyroclastic-surges", "-flows", "expanded" or "diluted", "concentrated", and "deflation zone". We show that even though pyroclastic-flows cover a large span of grain concentrations (between ~1 vol.% which is still fluidized to ~60 vol.%) they display only two granular behaviors: predominantly collisional (low viscosity) and frictional (high viscosity).

3- What is the main depositional process of pyroclastic-flows (i.e., *en masse* or progressive aggradation) [e.g., *Cas and Wright, 1988; Druitt, 1998; Freundt and Bursik, 1998*]? Classically, if pyroclastic-flows move as high concentration plug flows, then they deposit their material by *en masse* freezing and the transport and deposit are essentially the same. Alternatively, if the flow is diluted and fluidized, then, as the particles rain down to form a basal flow, it progressively freeze from bottom to up. In this latter case, the whole flow is stratified, subject to sharp concentration gradients, and the deposit is diachronous. Our results tend to demonstrate that the main depositional process is a progressive aggradation with a supply of sediments either by sedimentation from overlying surges, or by lateral transport from an upstream frictional flow, or both.

4- Is there a continuum between pyroclastic-flows and -surges [e.g., *Cas and Wright, 1988*]? And, how does flow transformation occur? As explained in §4, pyroclastic-surges and -flows significantly overlap each other in terms of granular regime (i.e., they have in common the collisional regime) and in terms of the granular rheology (i.e., they have in common a rate-dependent rheology). Thus from the granular theory standpoint there is a continuum. However, all our simulations show that the flow, from bottom to top, is subject to sharp decreasing concentration gradient. This suggests there is no-continuum between the pyroclastic-flow at the bottom and the overlying surge. In terms of flow transformations, our simulations show that surges and flows have a intertwined common history. For instance, pyroclastic-surges generate, by sedimentation, a denser basal pyroclastic-flows that will eventually outrun the expanded head of the flow [e.g., *Calder et al., 2000*] or a fluidized flows, near source, laterally generate overlying diluted surges further downstream.

This manuscript is organized as follow. First, we present the numerical methodology, viz., the computer codes (G)MFIX (§2.1) and the initial and boundary conditions for all our simulations (§2.2). Second, we discuss the plinian cloud simulations, emphasizing on the validation aspect and compare with various remote-sensing data (§3). Third, we discuss the pyroclastic-flow and surge simulations in the light of the granular rheological model (§4). Computer generated movies of all the simulations can be watched on the web at http://www.granular.org/partIImovies/. All the symbols and equations in this manuscript have been thoroughly defined in the companions paper (Appendix 1 and Appendix 2 of *Dartevelle* [*2003b*]).

2. Numerical Methodology

2.1. Numerical technique

MFIX (**M**ultiphase **F**low with **I**nterphase e**X**change) is a FORTRAN 90 general purpose computer code developed at the National Energy Technology Laboratory (NETL) and Oak Ridge National Laboratory (ORNL) for describing the hydrodynamics, heat transfer and chemical reactions in fluid-solid systems [*Syamlal et al., 1993; Syamlal, 1994; Syamlal, 1998*]. Initially, MFIX has been adapted from the Los Alamos National Laboratory's K-FIX codes (**K**achina with **F**ully **I**mplicit e**X**change) used to model the interaction of water and steam in a nuclear reactor [*Rivard and Torrey, 1977; Rivard and Torrey, 1978; Rivard and Torrey, 1979*]. We have adapted MFIX into a **G**eophysical version, (G)MFIX, in keeping all the capabilities of MFIX and adding new ones for typical geophysical-atmospherical applications (work associated with volumetric variations of the gas phase, atmospheric profiles, static *Smagorinsky*'s Large Eddy Simulation turbulence model [*1963, 1993*], *Zehner and Schlunder* model [*1970*], Sub-Grid turbulent Heat flux).

The historical relationship between MFIX, (G)MFIX, K-FIX, PDAC2D, DASH and other multiphase codes is shown on Figure 9. The "FIX" family codes have been used many times in volcanology in the past with success [e.g., *Valentine and Wohletz, 1989; Valentine et al., 1991; Dobran et al., 1993; Neri and Macedonio, 1996; Neri et al., 2002; Todesco et al., 2002*]. The IMF formalism adopted by the "FIX" family codes permits all degrees of coupling between the fields from very loose coupling as occurs in separated flows to very high coupling as occurs in true dispersed flows [*Harlow and Amsden, 1975; Ishii, 1975; Rivard and Torrey, 1977; Lakehal, 2002*]. Scalar quantities (e.g., mass, temperature, granular-temperature) are computed at the cell

center, whereas velocity components are computed on a staggered grid coinciding with the cell boundaries [*Patankar, 1980*].

The discretization of the hydrodynamic equations uses a finite volume method, which divides the physical domain into discrete 3D control volumes (i.e., cells) and then formally integrates the governing equations over them. This integration step ensures global conservation of mass, momentum, and energy independence of the grid-size [*Patankar, 1980*]. (G)MFIX uses an implicit backward Euler method of time discretization and includes various first-order (e.g., FOU) and second-order (e.g., Superbee, Smart, Minmod) accurate schemes for discretizing the convection terms [*Syamlal, 1998*]. We have favored FOU (First-Order Upwinding) for its stability, better convergence, and because we have not seen any significant differences in our geophysical simulations with the second-order schemes. The discretized equations are linearized with the Patankar and Spalding's SIMPLE algorithm (**S**emi-**IM**plicit for **P**ressure **L**inked **E**quations) [*Patankar, 1980; Spalding, 1981, 1983*; *Patankar et al., 1998; O'Rourke et al., 1998; Syamlal, 1998; Pannala et al., 2003*]. The interequation coupling between phases of the momentum and energy equations is dealt with the **P**artial **E**limination **A**lgorithm (PEA) of *Spalding* [*1981*] (see also *Syamlal* [*1998*], and Annex 6 in *Dartevelle* [*2003a*]). Within the SIMPLE algorithm, (G)MFIX solves the discretized equation using a linear solver iterative method such as the SOR (successive over-relaxation, an improved version of the Gauss-Seidel iterative method; e.g., see *Kapitza and Eppel* [*1987*]) and a more stable variant of the biorthogonal-conjugate gradient method (BI-CGSTAB; *van der Vorst* [1*992*]). (G)MFIX uses an automatic time-step adjustment to reduce the total run-time in achieving the best time step/number of iteration needed for convergence ratio at any given simulation time [*Syamlal, 1998*]. The code uses portable OPEN-MP (for shared memory multi-processors) and MPI (for distributed memory parallel computers) in an unified source code [Annex 6 in *Dartevelle, 2003a*].

Last but not least, MFIX has been extensively validated over the past years [e.g., *Boyle et al., 1998*] and grid-independence has been established for both MFIX in Fluid Cracking Catalytic risers [e.g., *Guenther and Syamlal, 2001*] and (G)MFIX for plinian column simulations [see Annex 5 in *Dartevelle, 2003a*].

All numerical data at each grid-point of the physical domain were post-processed by MATLAB® with interpolation functions to generate graphical results (snapshots and animation movies). Data sampling at specific locations within the data file were exported to spreadsheets to generate all the graphs shown in the next sections.

2.2. Initial and boundary conditions

Plinian cloud simulations (PL-group) were carried out in 2D Cylindrical geometry, where the axis of symmetry is a vertical free-slip reflector (next to the vent, Figure 10A). The pyroclastic-surge (PS) and -flow (PF) simulations (PSF-group) were done a 2D Cartesian geometry where the left-side vertical wall next to the vent is a free slip wall (Figure 10B). We have favored the Cartesian geometry because, in all of our simulations, PF and PS are small events which cannot be reconciled with an axisymmetric geometry: they tend not to spread all around the volcano but they are rather channeled and they rather flow down drainages [e.g., *Druitt, 1998*]; i.e., they flow in a specific direction. This is also the case in more important eruptions (e.g., Mt. St. Helens) and in analog experiments [*Woods and Caulfield, 1992; Sparks et al., 1997*]. The ground is a no-slip wall.

Table 7A details the boundary and initial conditions for all simulations. At the vent, all simulations are carried out with (i) a discharge gas pressure balanced with the local atmospheric pressure, (ii) thermodynamic equilibrium between gas and pyroclasts, (iii) only water vapor in the erupting mixture, (iv) constant mass flux at the vent throughout the whole simulation time (i.e., 1 hour for the PL-group and 8 minutes for the PSF-group), (v) within the same atmospheric environment assumed to be a dry, quiet and temperate standard atmosphere (Table 7B), and (vi), for the PSF-group, a nil granular-temperature as an initial condition (the end-result is insensitive of the initial value chosen for the granular-temperature). "Vent diameter or vent-length" must be understood as the diameter/length measured exactly where the mixture is not bounded anymore by a vertical wall. For instance, in PL_3 simulation (Table 7A), the large diameter of 800 m can be interpreted as the one of a large crater as seen in the 1990 Lascar eruption (which had a 1200 m diameter) [*Sparks et al., 1997*].

From Table 7A, the only difference between the simulation of a given group is the initial mass flux at the vent. Within the PL-group, there is about a factor of ten between each plinian simulation, while within the PSF-group, there is a factor two between PF_1 and PF_2 simulation. In order to compare the benefits of a comprehensive granular rheological model, we have performed a simulation (PF_3) in which the granular phase is assumed to be inviscid and compared with an identical simulation (PF_1, same initial/boundary conditions) which has a full kinetic-collisional-plastic formulation.

These grid-size configurations was mostly prescribed by our available computer resources. For the PL-group, the overall size of the computational domain has been chosen to ensure that the

whole plinian flow would remain inside the domain in order to capture the entire plinian activity (column, umbrella, shape, temperature anomalies) and to capture, with the best possible resolution, the column, its edges, and the transition between the column and the umbrella. The grid-size is uniform along the vertical direction and slowly increases radially away from the axis of symmetry. For the PSF simulations, the grid-size is thoroughly non-uniform over the whole computational domain with the highest horizontal resolutions on the left-side (10 m over a horizontal distance of 9 km) and the highest vertical resolutions at the ground (2.5 m over an height of 100 m). This resolution configuration has been chosen to enable us to capture flow transformations, sedimentation, depositional processes and to capture they exact relationship between PF and PS.

We do not claim to comprehensively simulate "real" plinian clouds or pyroclastic-flows and -surges with this limited set of initial and boundary conditions and with the limitation of our mathematical model [*Dartevelle, 2003b*]. Instead, we humbly aim -at this stage- to reproduce some of the known or expected physics of those volcanic events. Specifically, in this manuscript, we would like to demonstrate the importance of granular rheologies to capture some well-known features of PF and PS (e,g., formation of the deposit, outrun of the dilute part of flow by a more concentrated PF, lateral and vertical flow transformation processes) and demonstrate that multiphase flow models can simulate some of the well-known features of plinian clouds (column and umbrella).

We have carried out all our simulations with only one particle size because we wanted to keep the complexity of the model as "low" as possible in order to capture only the fundamental physics of our rheological model (more grainsizes would have implied supplementary assumptions and constitutive equations). Of course, natural granular flows are multi-sized which may have important effects upon flow dynamics [e.g., *Neri and Macedonio, 1996*]. Yet such supplementary complexity would have obscured the underlying physics behind granular rheologies. In the long run, supplementary particle-sizes may be introduced in our model. In the same vein, the boundary condition at the ground is a flat surface because 2D topography would not have added anything relevant to our current modeling objectives.

3. Plinian cloud modeling

Figure 11 represents various snapshots of the logarithm of the volumetric grain concentration, $\log_{10}(\varepsilon_s)$ (from 10^{-2} to 10^{-9}), taken at different times (from 300 s to 3600 s) for three plinian simulations. Figure 12 represents the altitude of the top (H_T) of the plinian column vs. time. The

following description is also based on the computer-generated movies of three plinian simulations (Movie 1 to Movie 3 for simulation PL_1 to PL_3 respectively). Before starting descriptions, we define the mean mixture value of a given variable (Ψ) such as speed (U_x or V_y) or temperature (T_m) and the mean mixture density (ρ_m) [*Valentine and Wohletz, 1989; Dobran et al., 1993*]:

$$\Psi = \frac{\varepsilon_s \rho_s \psi_s + \varepsilon_g \rho_g \psi_g}{\rho_m} \quad (1)$$

$$\rho_m = \varepsilon_s \rho_s + \varepsilon_g \rho_g \quad (2)$$

where ψ_s and ψ_g are the corresponding variable of a given phase (all other symbols are defined in the Appendix 1 of *Dartevelle* [*2003b*]).

3.1. General descriptions

First, let us describe simulation PL_1 ("weak" eruption, ~10^6 kg/s). The jet part is quickly decelerated to an altitude of about 1 km from which a rising buoyant convective plume develops. At 200 s (see Figure 12), the plume has reached an altitude of 4.5 km. At that time, a partial collapse of the system occurs at the transition between the jet and lower part of the plume, forming small pyroclastic-flows (Movie 1). Figure 12 shows the plume growth rate in the atmosphere has significantly decreased. Once the system is relieved from this excess of materials (400 s), the plume regains enough buoyancy to move upwards to higher altitudes (Figure 12). At about 900 s, the column has reached a maximal altitude of about 12 km. At 1300 s, the center at the top of the column starts to partially collapse downwards (Movie 1). As it falls down toward higher atmospheric pressure, the column adiabatically warms and regains positive buoyancy (1500 s) and then starts to spread radially at an altitude of 5 km. In Movie 1, the umbrella between 5 and 6 km is formed by expelling sideward all the material coming from below and above. At 2400 s, the whole plinian system stabilizes over time and gently spreads radially with no noticeable change of H_T. Within an hour, H_T is about 13.5 km and the maximal radial distance is about 12 km. The umbrella is clearly sheared as the mixture mean radial speed (U_x) shows very complex back- and forwards profiles (Figure 13). For instance, at a radial distance of 6 km from source at 3600 s, backwards currents are well-developed at altitudes of 6, 9, 10 km, which

explains this fingering shape. Also, note the systematic backwards current at the bottom of the umbrella.

From Movie 1, turbulence and eddy developments are the most active between a radial distance of 1 and 2 km, i.e., within the transitional zone between the column and the umbrella. This explains the complex radial speed profiles at a distance of 1 km in Figure 13 where an important entrainment of air in the column between an altitude of 2 and 3.8 km and reentrainment of pyroclastic materials to the column at higher altitudes occurs (e.g., at altitudes of 4.4, 5.5 km, and between 8.5 and 10 km). These radial speed profiles, the backward currents within the umbrella, and the multi-layered umbrellas are in a qualitative agreement with the experimental observations of *Holasek et al*. [*1996*]. However, in PL_1 simulation, it can be seen from Figure 11 and Movie 1 that multi-umbrellas are formed very early as the column rises in the atmosphere. In addition, their development is strongly dependent on the exact state of turbulence and eddies within the clouds. Hence the multi-layered umbrellas are caused by the chaotic nonlinear dynamics within the clouds and cannot solely be attributed to a secondary sedimentation of particles along the edges of the column from another, higher up, preexisting umbrella as suggested by *Holasek et al*. [*1996*].

Second, we describe PL_3 ("strong" eruption, ~10^8 kg/s), which has a mass flux ~100 times higher than the PL_1 simulation. Because the jet suffers strong deceleration while "pushing" against the atmosphere, it converts nearly all its initial kinetic energy into heat. Hence the top of the jet is characterized by much higher pressure than the ambient (e.g., after 3600s, it has an excess of 15 hPa at 2.4 km) [*Vallentine and Wohletz, 1989*]. Above the over-pressurized top zone of the jet, the plume drastically expands and accelerates outward (altitude 4 km on Figure 11C). It therefore reduces its density and becomes positively buoyant (e.g., note the "bulgy" shape of the column above the jet between 4 and 6 km in Figure 11C). At 300 s, the plume has reached an altitude of ~17 km (see Figure 12) and starts to spread laterally to form an umbrella. However, the plume is still moving upwards to an altitude of 22 km owing to its inertia. In Figure 11C (600 s), the top of the column is therefore 5 km higher (i.e., 21 km) than the top of the umbrella which is between 12 and 16 km. Once the momentum is exhausted (700 s), the column drops to 19.6 km, pushing materials downward and most importantly sideward forming a second "umbrella mass flow" between 15 and 20 km above the first umbrella. Afterwards, the column will continuously grow to higher altitudes with the formation of secondary diluted clouds topping the column itself (see Figure 11C at 2400 s and Movie 3). After one hour, the plinian column has reached a maximum altitude of about 29 km and a radial distance of about 52 km.

Figure 14 represents radial speed profiles along the vertical direction within the PL_3 cloud measured at different positions at 3600 s. Again, the umbrella is clearly sheared. It has a well-developed positive radial speed of 26 m/s at 10 km decreasing to less than 10 m/s at 40 km away from source. U_x tends to be maximum in the central part of the umbrella and to be negative at the top and bottom where friction with the atmosphere is maximum. Because of the active turbulent area between the column and umbrella (e.g., at a radial position of 5 km), U_x shows complex back and forth speed profiles with an important entrainment of fresh air at the bottom of the column, specially where it expands the most (between 4 and 7 km of altitude). Figure 15 shows V_y profiles at different heights within the PL_3 cloud at 3600 s. At an altitude of 1 km within the jet, V_y has a classical Gaussian shape profile where V_y is maximum at the center of the column and exponentially decreases towards the edges of the jet. At 4 km, at about the transition between the jet-plume, V_y tends to be minimal at the center of the column but is maximal at the edges of the column where entrainment is the most active. This is consistent with negative U_x profile at the bottom just next to the column as in Figure 14. At 6 km, V_y is positive along the whole radial direction (from center to edges) owing to the expansion and the active entrainment of fresh air between an altitude of 4 and 5 km. At higher altitude vertical speed profiles tend to show more classical Gaussian shape profiles, although disturbed by turbulence, reentrainment, and the formation of vertical convective super-cells between the plume and the umbrella. Note that those speed profiles only represent the situation at time 3600 s.

As noted by *Dobran et al*. [*1993*] and as seen in Figure 16, it is difficult to determine exactly the transition between the strongly thrusting jet and the buoyant plume itself. Figure 16 shows the variation along the vertical direction inside the plinian column PL_3, at time 3600 s, of the averaged mixture temperature (Figure 16A), the pressure anomaly relative the ambient (Figure 16B), the averaged mixture vertical speed (Figure 16C), and the density differences relative to the ambient (Figure 16D) of the macroscopic gas phase density ($\Delta\rho_g$, dashed curve) and the macroscopic solid phase density ($\Delta\rho_s$, plain curve) of the column. Just above the vent (80 m), the jet is overpressured relative to the ambient (+ 59 hPa, not seen on Figure 16B) which is also shown by a slight decrease in V_y owing to the conversion of kinetic energy into pressure. Higher up the jet tends to reequilibrate with the ambient showing a sharp decrease in ΔP_g (down to +0.96 hP) and a slight increase in V_y. The thrusting decelerating jet into the atmosphere causes a second pressure maximum (+15 hPa) at an height of 2.4 km suggesting a classical flaring characteristics or diamond-like structure of overpressured jets [*Valentine and Wohletz, 1989*] as seen in Figure

16B. At 3.9 km, ΔP_g decreases to a negative value (decompression) down to -12 hPa, hence the column expands, which drastically reduces the density of the system in making the solid phase positively buoyant relative to the ambient (Figure 16D). The expansion of the system also reduces the temperature by nearly 200 K (Figure 16A), hence causing a slight decrease in buoyancy of the gas phase (Figure 16D). Owing to the inertia of the jet, at an height of 3.9 km, V_y is minimum at the center of the column while at its edges, V_y is ~+73 m/s (Figure 15). The radially fast expanding system and the sharp increase of buoyancy cause the system to reaccelerate up- and out-wards from slightly less than 0 m/s to 80 m/s at 6.4 km causing a reincrease in ΔP_g (third maximum in pressure at ~9.8 km). Clearly, between the top of the thrusting jet and the fully buoyant plume, there is a transitional zone which extends between the second maximum in pressure (altitude 2.4 km) and the altitude of full positive buoyancy (i.e., 3.9 km). As we have previously suggested, Figure 16 only represents the situations within the jet-column for the time 3600 s and, in no case, represents a static situation.

The intermediate plinian simulation (PL_2) presents very similar features as PL_3 (see Movie 2 and Figure 11B). The transition between the jet and the plume is at about 2 km with a well developed "swelling" at the top of the jet owing to the expansion of the plume. At 1200 s (Figure 11B), the column starts to develop multi-layered "umbrella" mass flows which will eventually merge together into a one umbrella flow at 2000 s (yet it should be born in mind that the radial resolution decrease away from source, hence this seemingly "merging" may be due to the poor resolution further downstream in our simulations).

Both PL_2 and PL_3 simulations clearly show a pulsating behavior with time (see Movie 2, Movie 3 and Figure 12).

3.2. Discussion

3.2.1 Top altitude vs. Mass flux

Plinian column upper-heights (H_T) have been often related to the mass flux at the vent because this flux represents the amount of energy released and available to the plinian column. Figure 17 represents H_T of the plinian column vs. the inferred mass flux at the vent for different historical eruptions and our plinian simulations (PL_1, PL_2, and PL_3) where H_T is measured at 3600 s. Also shown on Figure 17, the best fit curve between the past eruptions [*Wilson et al., 1978; Settle, 1978; Sparks et al. 1997*] and two curves from *Morton et al*.'s theory [*1956*] for two temperatures at the vent [from *Wilson et al*., *1978*]. Knowing the uncertainties to infer the exact

H_T and, most importantly, the mass flux at the vent for historical eruptions, H_T predicted by our model is in excellent agreement with past eruptions and quite surprisingly with *Morton et al* [*1956*] theory which was developed for plume within the troposphere for a constant temperature gradient [*Sparks, 1986*]. From Figure 17, we may conclude that (G)MFIX model can accurately be compared with classical plume theory [e.g., *Morton et al., 1956*; *Wilson et al, 1978; Sparks, 1986*] and most importantly real observations.

3.2.2 Temperature anomalies

Temperature anomalies at the top of the column are an important features to capture as they can easily be measured by satellite remote sensors, hence this provides a supplementary way to compare with real data. Figure 18 and Movie 4 show the temperature anomalies relative to the ambient (ΔT) vs. time for the simulation PL_3. In Figure 18, we match H_T variation with ΔT measured at the "tip of the top" of the plinian column. During the early stages, the column rises into the atmosphere where the ambient pressure decreases, hence the column expands which causes a sharp decrease of temperature at the top of the column: at 500 s and an height of 22 km, the top of the column is undercooled relative to the ambient by 11 K. As the column drops (to 19.6 km at 700 s), the column contracts and adiabatically warms up (+ 19 K). Since the column PL_3 has a natural tendency to pulsate, H_T changes with time, so does ΔT (Figure 18). From Movie 4 temperature anomalies can be seen throughout the plinian PL_3 cloud. In particular, vertical convective super-cells are developed between the column and the umbrella where the down- and up- draughts are warmer and colder respectively than the ambient.

In Figure 18, we have sampled our numerical data every 100 s within a one-hour span, hence it is rather difficult to compare with remote-sensing data only taken every hour or so. We nevertheless note that *Holasek and Self* [*1995*] have measured temperature anomalies between -6 K to -15 K in Mt. St. Helens plume and, for El Chichón, *Woods and Self* [*1992*] have inferred temperature anomalies as low as -20 K. Those data match very well with the -11 K measured at the "tip of top" of our simulated plinian column (PL_2 and PL_3), but also with the temperature anomalies deeper inside the PL_3 column which are as low as -18 K (not shown on Figure 18). Simulation PL_2 shows the same trend of ΔT variations at the top of the column but within a smaller temperature span (-9 K and +15 K). Simulation PL_1 only shows small temperature anomalies as it rises in the atmosphere (-10 K) and after 500 s, the top of the cloud has the same temperature as the ambient.

3.2.3 Non-uniform clouds and remote sensors

A close inspection of the umbrellas in Figure 11, Movie 1, Movie 2, and Movie 3 suggests that plinian clouds are very heterogeneous in terms of the volumetric solid concentrations both in time and space (vertical and lateral variations), even far away from the column. This is an important result for remote-sensing techniques which assume the cloud is somehow homogenous within the pixel where measurement is carried out. For instance, the retrieval of sizes and particle burden within volcanic clouds with the AVHRR band 4 and 5 [*Wen and Rose, 1994*] relies on a well-defined homogenous single layer umbrella which is not the case in Figure 11A (multi-layered umbrellas), or Figure 11B and Figure 11C which show complex concentration profiles within the 10 to 20 first kilometers from source. The retrieval of cloud temperature with the brightness temperature method relies on a fully opaque homogenous clouds, hence retrieves temperature where it is very dense [*Sparks et al., 1997*]. However, it is well-known [*Sparks et al., 1997*] that plumes present at their tops low ash concentrations regions, which is fully confirmed by our numerical models (Figure 11 for all three plinian simulations). Hence temperature measured by remote-sensors corresponds to a (unknown) depth within the plume at the point where the plume becomes opaque and not necessarily correspond to the "tip of the top" of the plume as we have measured in Figure 18. Hopefully, in a near future, multiphase flow modeling will provide further useful hints about the non-uniformity of plinian clouds which may eventually help for the development of better and more accurate retrieval algorithm.

3.2.4 Unsteady clouds

Strong plinian columns tend to be highly unsteady and pulsate with time [*Rose et al*., *1995; Zurn and Widmer, 1996; Tahira et al., 1996; Johnson, 2003*]. This unsteady behavior is also well known by field volcanologists who have observed that many plinian fall deposits exhibit variation in particle size as a function of the stratigraphic height. Usually, reverse grading is more common and is interpreted as due to an increasing eruption intensity with time [*Cas and Wright, 1988; Sparks et al., 1997*]. That is exactly what is shown for PL_3 in Figure 12 and Figure 18 where, at 700 s, the altitude is 19.8 km and within the next 2900 s the altitude increases to about 29 km. It is even possible that PL_3 cloud has not yet reached its maximum altitude after one hour of simulation. We speculate that such important increase of height over nearly one hour may be the cause of reverse grading in the fallout deposits.

Another interesting feature of plinian simulations PL_2 and PL_3 are the small vertical bursts and pulsations of the column with altitude variations of about ±1 to 3 km and with a periodicity

of about 5 minutes (Figure 12, Figure 18, and Movie 2 to Movie 4). *Rose et al*. [*1995*], using real-time radar observations, showed that the altitude of Crater Peak September 12, 1992 eruption column fluctuated within ±2 km, which is consistent with our simulations. Such vertical gravity-acoustic waves as seen in Movie 2 and Movie 3 are also well-confirmed by measurement of acoustic and world-wide Rayleigh waves generated by powerful eruptions [*e.g., Zurn and Widmer, 1996; Tahira et al., 1996; Johnson, 2003*]. Typically in the cases of strong eruptions such as Mt. St. Helens. [*Mikumo and Bolt, 1985*] and Mt. Pinatubo [*Tahira et al., 1996; Zurn and Widmer, 1996*] more than 10 hPa of pressure anomalies with a periodicity of a few minutes have been measured. The magnitude of those measured pressure anomalies are also confirmed by our simulations as seen in Figure 16B. Those vertical acoustic-gravity waves are recognized as a positive feedback, self-organized, and self-excited natural oscillator [*Zurn and Widmer, 1996*]. For instance, the rising and expansion of the plume within the atmosphere excites a large spectrum of acoustic and gravity waves (i.e., plume forcing of the atmosphere). On the other hand, the plume experiences harmonically varying buoyancy forces which makes the plume fluctuate in height (i.e., atmosphere forcing of the plume). This latter forcing is caused by harmonic pressure fluctuation within the plume and by the difference between compressibility of the atmosphere and the plume [*Zurn and Widmer, 1996*]. In addition, such an effect may be enhanced by the unsteadiness and non-uniform compressibility of the plume. These harmonic variation of the plume will again trigger new acoustic and gravity waves (positive feedback).

Our simulations suggest that these periodic fluctuations as well as the global progressive increase in altitude of the column should not be *ipso facto* interpreted as variations at the vent level (e.g., widening of the vent, V_y or mass flux variations) but should rather be seen as a inner, nonlinear, and chaotic feature of strong plinian clouds. In all our simulations, the vent conditions were maintained constant over the whole simulation-time. Clearly, from Movie 3, it can be seen that the trigger mechanism of the gravity-acoustic waves is the pressure anomalies between the jet and the plume and not any oscillating phenomena inside the volcano. Our results are in complete agreement with the observation of *Zurn and Widmer* [*1996*] for the 1991 climactic eruption of Mt. Pinatubo.

This is a new aspect of the physics of the plinian cloud dynamics, which has never been modeled before. It also confirms the significance of pressure anomalies for the control of the dynamic of the plinian cloud and therefore confirms the importance of including such phenomenon in an *ad hoc* mathematical model [*Valentine and Wohletz, 1989*].

4. Pyroclastic flow and surge modeling

Before all, we must clarify the exact meanings of pyroclastic "-flows" and "-surges" in the light of granular theories (kinetic-collisional-frictional). In the companion paper (Figure 7), *Dartevelle* [*2003b*] has shown that the granular rheological behavior and coupling with the gas phase turbulence are deeply dependent on the volumetric grain concentrations (ε_s). It is possible to recognize different regimes which overlap each other. First, the *purely kinetic regime* for very dilute suspension ($\varepsilon_s<\sim10^{-3}$ vol.%) where collisions do not occur, the granular-temperature tends to be maximized, and so does the granular shear viscosity. Second, the *transitional kinetic-collisional regime*, $10^{-3}<\varepsilon_s<1$ vol.%, collisions progressively become more and more important so that the granular-temperature is decreased, and so is the shear viscosity. Third, the *predominantly collisional regime*, $1<\varepsilon_s<50$ vol.%, collisions are predominant so that the granular-temperature is decreased to negligible values (because of inelastic collisions), and the granular shear viscosity has reached a minimum. Fourth, the *frictional regime*, $\varepsilon_s>50$ vol.%, the plastic behavior becomes more and more predominant, hence shear frictional viscosity asymptotically goes to infinity, so does the strength of the granular material, and at ~64 wt.% (the maximum possible volumetric concentration for a randomly packed structures), the granular "flow" freezes (i.e., granular deposit). Hence, in this view, friction only acts as a physical process between the collisional flowing regime and a static deposit.

Following *Sparks et al*. [*1997*], the pyroclastic-surges belong in the kinetic and kinetic-collisional regime (i.e., $\varepsilon_s<<1$ vol.%), where the random chaotic kinetic motion of grains is the dominant mechanism of momentum and energy transfer between sheared layers. Pyroclastic-flows would belong to the predominantly collisional and plastic-frictional regime ($1<\varepsilon_s<60$ vol.%). Hence, pyroclastic-flows cover a quite appreciable range of volumetric grain concentrations and can be still seen as partially fluidized flows in their low concentration range. According to this rheological model, there is a continuum within the kinetic-collisional regime (rate-of-strain dependent) and a sharp discontinuity between the collisional and the plastic regimes (which is rate-of-strain independent) [*Dartevelle*, *2003b*]. However, in volcanology, the concept of continuum between expanded and concentrated flows is rather defined in terms of concentration gradients within the flow. In this view, we will demonstrate that there is little evidences of continuum between pyroclastic-flows and -surges.

In the interpretation of our numerical results (PF_1, PF_2, and PF_3), we will only focus on four themes: (i) relative dynamic behavior between PS and PF and flow transformation, (ii)

formation of a deposit, (iii) dynamics close to the source, (iv) the relevance of a nonlinear rheological model for granular flows (viscous or inviscid). Figure 19 and Figure 20 show the development of PF/PS over 8 minutes between 30 s and 480 s for simulation PF_1 and PF_2 respectively. Each curve represents a solid volumetric iso-concentration contour line between 10^{-9} and 10^{-1}. Movie 5 and Movie 6 show respectively the development of PF_1 and PF_2 simulation. Figure 21 (PF_1) and Figure 22 (PF_2) show the height variation of granular volumetric concentration, average mixture horizontal speed, granular-temperature, and granular shear viscosity taken at different positions and different times.

4.1. General descriptions

Simulation PF_1 (Figure 19, Movie 5, and Figure 21A). After 30 s, the flow has reached a distance of 1.4 km with a well-developed head about 400 m high and ε_s ranging from $9x10^{-5}$ vol.% at the base to $\sim10^{-2}$ vol.% higher up (Figure 21A). The horizontal speed of the head is 9 m/s at the base and 34 m/s at a height of 20 m. The head has a well-developed overhang (nose) because the base is much more diluted and slower, the overhang acting as a funnel for air (preferential entrainment at the base) and the much higher granular shear viscosities ($\sim5x10^{-2}$ Pa·s, while $\sim2x10^{-3}$ Pa·s higher up within the head). According to our classification scheme, this head has all the properties of a surge (predominately kinetic and mildly collisional). At 80 s, the head is 3.7 km away from source and has so much entrained fresh air that its concentration has decreased by a factor 10^3 (e.g., at 20 m high, $\varepsilon_s\sim10^{-5}$ vol.%). Such drop in concentration has drastically decreased the horizontal momentum (e.g., at 20 m high, $U_x\sim13$ m/s). The granular shear viscosity has increased and is uniform throughout the whole head ~0.2 Pa·s. At 100 s, the front of the flow is at a distance of 4.3 km with a basal collisional pyroclastic-flow outrunning what remains of the dissipated head (see Figure 21A and Figure 19 at 80s, 100s, 120s). The basal pyroclastic-flows has a concentration of ~30 vol.% and travels at a maximum horizontal speed of ~45 m/s. Because this basal undercurrent lies in the purely collisional regime its granular-temperature and granular shear-viscosity are very low ($<<10^{-4}$ m^2/s^2 and $\sim10^{-3}$ Pa·s respectively, see Figure 21A). The other striking feature is that within a height of 5 m the volumetric concentration decreases from 30 to 0.1 vol.%, suggesting a sharp concentration gradient between the basal PF and the overlying PS. In other words, there is no progressive transition between the basal dense PF (purely collisional regime) and the overlying diluted PS (kinetic regime); hence the overall flow is strongly stratified. We will explain below how and where this basal concentrated flow is formed (§4.2.1). At 180 s, the basal PF has outrun the rest of the flow and

has traveled 7.2 km. In the body of the flow, closer to source, phoenix clouds start to form because the flow system is losing its horizontal momentum which leads to sedimentation on the ground and dilutes of the upper part of the flow which becomes positively buoyant [*Dobran et al., 1993*]. At 240 s, the flow front is detached from the rest of the flow system, and because it is not fed anymore, it progressively becomes more and more dilute until it comes to rest at about 300 s and 8.8 km. Secondary minor thin PF/PS flows (i.e., 5 to 7 meters high) are formed from the main flow system upstream and can travel downstream up to 9 km. Those low-energy secondary flows are quickly stopped by inward winds [*Valentine and Wohletz, 1989*]. Note that at the end of the simulation, there are clear draughts towards the base of the rising phoenix cloud (between 3.5 and 6 km) which produces an inwards necking effect of the fast rising coignimbrite cloud [*Dobran et al., 1993*] as seen for instance during co-ignimbrite ashcloud development in the 1991 Mt. Pinatubo eruption [*Woods and Wohletz, 1991; Sparks et al., 1997*]. At 480 s, the system forms a granular deposit (ε_s~60 vol.%) between 3.6 and 5.4 km with a thickness as high as 12.5 m and a second minor deposit between 6.6 and 7 km with a thickness of about 7.5 m. The base of the flow has a frictional behavior ($50<\varepsilon_s<64$ vol.%) between 2.47 and 7.76 km. Close to source, the flow has a collisional behavior ($\varepsilon_s<10$ vol.%) between 80m and 500 m and further away between 500m and 2.4 km a predominantly collisional behavior ($10<\varepsilon_s<50$ vol.%). This suggests the existence of a maintained "deflation" zone next to the source [*Sparks and Walker, 1977; Sparks et al., 1978; Walker, 1985*]. However we will discuss below the exact meaning of "deflation" in this context.

Simulation PF_2 (Figure 20, Movie 6, and Figure 22A). After 10 s, the head of the flow is well formed but more dilute, smaller, and slower than in PF_1: 80 m high, with concentration $2x10^{-5}$ vol.% at the base, and 10^{-3} vol.% at the nose level, traveling with horizontal speed of 5 m/s at the base and 12 m/s at the nose level. It has much higher and homogenous granular-temperature (~10 m^2/s^2 at the base) and granular shear viscosity (~0.1 Pa·s) than PF_1 simulation. This head will eventually be outrun by a denser basal pyroclastic-flow but much quicker than PF_1: at 40 s, this basal underflow has a concentration of 15 vol.% with a maximum horizontal speed of 39 m/s, and granular shear viscosity of $2x10^{-3}$ Pa·s. The shear viscosity has decreased relative to the head because collisions dissipate the granular-temperature; from ~1 m^2/s^2 at 30 s (PS) down to ~10^{-3} m^2/s^2 at 40 s (PF). This undercurrent will eventually travel to 8 km (300 s), then be detached from the main system and as it is progressively diluted, it will be halted by inward winds at 9 km. In the meantime, the system starts to develop a phoenix cloud at 1.5 km

from the source (much closer than PF_1 owing to the lower initial momentum). Secondary minor phoenix clouds are developed at a distance of about 4.8 km at 210 s and at 6 km at 480 s. Note that those phoenix clouds are much less vigorous than in PF_1 and tend to bend inward and even slide backwards pushed by draughts (Movie 6). At 480 s, the system forms a granular deposit (ε_s>60 vol.%) between 3.5 and 4.7 km with thickness of up to 10 m. The frictional behavior (ε_s>50 vol.%), at the base of the flow, lies between 2.3 and 5.3 km and also 7.5 and 7.9 km. We also note a "deflation zone" close to source but more concentrated than in PF_1: with a predominant collisional behavior (10<ε_s<50 vol.%) within the first 2.3 km from source.

The simulation PF_2 produces the same kind of results as PF_1 but much earlier in the time sequence (deposit, basal PF outrunning the head of the flow, …), more concentrated ("deflation" zone), a slower (head, PF) with a deposit having a smaller extent. Owing to the lower horizontal momentum of the PF_2 basal undercurrent, it is detached from the flow system at a later time (300 vs. 240 s).

4.2. Discussions

4.2.1 Proximal deflation zone and flow transformations (lateral and vertical)

From previous descriptions, a denser (predominantly collisional PF) basal underflow systematically outran downstream the initially more diluted suspension current (purely kinetic PS). This is well documented in various eruptions, e.g., in Montserrat, Katmai, Mount Pinatubo, Lascar [*Druitt, 1998; Calder et al., 2000*]. We speculate that the initial highly diluted head may deposit a thin layer, often named "ground-layer", "ground-surges", or "layer-1" found at the bottom of pyroclastic-flow deposits (hence deposited first, see discussion in *Cas and Wright* [*1988*]). In our simulations, this ground-layer deposit cannot be seen owing to the lack of vertical resolution. In the context of those simulations, the question is therefore where is this collisional undercurrent formed? *Sparks and Walker* [*1977*], *Sparks et al.,* [*1978*], and *Walker* [*1985*] have suggested the existence of a "deflation zone" near the vent where denser pyroclastic-flows are selectively segregating from a highly turbulent, diluted, expanded low-concentration flow (see also the discussion in *Valentine and Wohletz* [*1989*]). Figure 21B (simulation PF_1) and Figure 22B (simulation PF_2) show ε_s and U_x within the flow sampled at different times 250 m from source, while Figure 21C and Figure 22C show the same variable sampling within the same time frame but 2.5 km from source. For both simulations, at 250 m from source, the concentrations (~0.1 to ~12 vol.%) and U_x (~13 to ~33 m/s) do not change significantly with time suggesting a

fluidization zone maintained over-time next to the vent. At 2.5 km, the situation is different as the concentration at the bottom of the flow increases with time (e.g., for PL_1 at 2.5 km: 32 vol.% at 60 s to ~50 vol.% at 480s) and U_x values are much higher than at 250 m from source (i.e., for PF_1: between 40 to 58 m/s and for PF_2: 28 to 36 m/s). Hence, from this observation, we may conclude that the denser basal PF has been partially segregated from an upstream source.

The second important feature is the relationship between the overlying PS and the basal PF. For instance, in Figure 21C, there is a sharp decrease of ε_s along the vertical direction within 5 m (at 480s, from 50 vol.% at the base to less 0.1 vol.% at an height of 30 m) which shows the presence in this simulation of an active dilute suspension flow (a kinetic-collisional pyroclastic-surge moving as fast as 50 m/s) over a basal underflow (predominantly collisional, slightly frictional moving at 40 m/s). This indicates that overlying dilute suspensions may also have an important role in the grain "feeding" of the basal PF. Yet, in simulation PF_2 (Figure 22C, Movie 6), there is no obvious overlying surge further downstream than 2 km, which would suggest, in this case, that the denser basal PF is solely laterally segregated from the "deflation zone".

The term "deflation" zone deserves to be clarified in this context. As previously noted by *Valentine and Wohletz* [*1989*], the concentrations in the "deflation" zone can be much higher than further downstream. For instance, simulation PF_1 (Figure 21B and C), at 480 s, 40 m high, ε_s~5 vol.% which is a predominantly a collisional regime (i.e. a maintained fluidized PF) and, at 2.5 km downstream, $\varepsilon_s \sim 10^{-2}$ vol.%, which is a kinetic-collisional regime (i.e., a dilute PS). Simulation PF_2 shows even sharper trends: at 480 s, 5 m high, at 250 m away from source, ε_s~3 vol.% (Figure 22B) and, at 2.5 km from source, $\varepsilon_s \sim 10^{-3}$ vol.% (Figure 22C). Hence the deflation zone is not necessarily where the particle-laden flow is the most dilute. Nevertheless, it is certainly where basal concentrated pyroclastic-flows start to laterally segregate. It also indicates that higher up in the flow, there is a lateral transformation from a fluidized, collisional PF (near source) to a much more diluted and kinetic PS further downstream. We would rather suggest renaming "deflation zone" to "maintained fluidized zone" as the former term would be synonym of "dilute" in the volcanological context.

4.2.2 Progressive aggradation vs. en masse deposition

For many decades volcanologists have debated whether pyroclastic-flows and other geophysical granular gravity currents are deposited *en masse* (i.e., the flow suddenly and as a whole "freezes") or by progressive vertical aggradation (i.e., by a sustained sedimentation from a more diluted overlying current) [e.g., *Branney and Kokelaar, 1992; Druitt, 1998; Calder et al.,*

2000]. In the former case, the thickness of the flow unit and the parent flow are essentially the same, while in the latter, it implies a continuous sediment feeding from a more dilute current above the deposit. Any stratification within the aggradational deposit would reflect changes in flow steadiness, in the materials supplied at the source, or sedimentation time-break [e.g., *Branney and Kokelaar, 1992; Druitt, 1998*]. Since our model specifically links together granular shear viscosity, yield strength of the granular flow, and its concentration through the plastic potential and critical state theories [*Dartevelle, 2003b*], our simulations may shed light on the exact nature of the depositional process.

Figure 21D (PF_1) and Figure 22D (PF_2) show at a fixed position (4 and 3.7 km respectively) the volumetric grain concentration, averaged mixture horizontal speed, granular-temperature, and granular shear viscosity of the flow sampled at different times. PF_1 has, at 100 s, a basal concentration of 44 vol.% and is flowing with an horizontal speed of ~40 m/s. This collisional pyroclastic-flow has low granular-temperature ($\sim 10^{-5}$ m^2/s^2) and low granular viscosity ($\sim 10^{-3}$ Pa·s). At 180 s, the flow shows plastic-frictional behavior (ε_s~55 vol.%) with U_x at the base reduced to 26 m/s, and granular shear viscosity increased by a factor of ten thousand (~10 Pa·s). At 300 s, the basal part of the flow has reached a concentration of ~60 vol.% over an height of 7.5 meters and, at 480 s, over an height of 12.5 meters. At those concentrations, at the base of the flow, U_x~0 m/s, granular-temperature is negligible and shear granular viscosity is $\sim 10^4$ Pa·s (the maximum allowed in our model). Simulation PF_2 shows the same trends, however slower and more progressive, at a distance of 3.7 km: at the base, at 200s, ε_s~51 vol.%; at 360 s, ε_s~58 vol.% (not shown on Figure 22D), and at 480 s, ε_s~60 vol.% over an height of 7.5 m (which is quasi-idle: U_x~0 m/s).

From these figures, with time, the overall deposit is progressively building upwards which supports a progressive aggradation mechanism as main depositional process. At any given location, the deposit as a whole is diachronous [*Druitt, 1998*]. The base is formed from sediments deposited much earlier from either above or from upstream locations. While, progressively upwards in the deposit sequence, sediments are deposited from later and upstream parts of the flow. This is demonstrated by the progressive reduction of U_x with time and at any given height within the flow and, also, by the reduction of U_x from bottom to top for a given time (e.g., Figure 21D).

It should be also mentioned that PF_1 and PF_2 have an important differences in the nature of the overlying surges: these are dilute and quasi non-existent at further distances than 2 km for

PF_2 (Figure 22D), while active, fast, and moving further downstream for PF_1 (Figure 21D). Hence vertical aggradation and formation of a subsequent deposit are the result of two processes for PF_1: (i) sedimentation from the overlying surge and (ii) supply of fresh granular materials by frictional flow coming from upstream. For PF_2, the major source of sediments is mainly from what is brought by frictional flow coming from upstream locations. In all the cases, these plastic-frictional flows are initially generated from the "maintained fluidized zone", near source, following this lateral flow transformation:

Collisional fluidized PF (near source)→kinetic PS→collisional PF→frictional PF→deposit.

This implies that -at any given height within the deposit sequence- an elementary flow unit stops when its yield strength becomes infinite, hence when its concentration is close to $\sim^{max}\varepsilon_s \sim 64$ vol.%. Therefore, our mathematical model fundamentally generates a deposit by *en masse* freezing of an elementary flow unit when concentrations reaches ~64 vol.%. Each flow unit is built with fresh sediment brought either from upstream sources (lateral accumulation by plastic-frictional flows) or -if any- from overlying surges (vertical accumulation by sedimentation). Our model implies that *en masse* freezing is not at all antagonistic with vertical aggradation; the former acts on an elementary flow unit, the latter acts over the whole deposit sequence as seen on Figure 21D and Figure 22D. Our model and numerical results are consistent with field observations [e.g., *Calder et al., 2000*] and naturally reconciles opposing views of depositional processes.

4.2.3 Pyroclastic flow and surge relationships

A close inspection of Figure 21 and Figure 22 demonstrates that both pyroclastic-flows and surges have an intertwined history. As an initial conditions, the flow was diluted at the source (see Table 7) and eventually segregates into a denser basal pyroclastic-flows and into a more dilute suspension above it. By sedimentation and by continuous feeding from upstream the bottom of the flow will eventually come to rest. In the previous section, we have seen a lateral flow transformation occurs from PF close to source into PS further downstream. In addition, by sedimentation, the overriding PS current looses its momentum and becomes sufficiently dilute to loft and form phoenix clouds as seen in Figure 19 (e.g., 180 s) and Figure 20 (e.g., 100 s). These coignimbrite clouds may afterward feed the system with new fallouts as they are pushed back and forth by in- and out-ward draughts.

We note that deposits are the result of frictional flows as the plastic behavior acts as transitional regime between collisional flow and idle granular deposit. Hence deposits only

represent the concentrated part of the flow. Therefore, any flow unit may give very little evidence about the presence of active overlying expanded currents or evidences of stratifications of the overall flow system.

From Figure 21 and Figure 22, any properties of the flow (concentration, velocities, so forth) sharply change with time (unsteadiness) and space (non-uniformity, both vertically and horizontally) [*Freundt and Bursik, 1998*]. Globally, it is difficult to see the whole pyroclastic phenomenon with only one of the end-members (i.e., either dilute or concentrated), which justifies a multiphase model approach, able to model the whole spectrum of volumetric grain concentrations provided that a comprehensive rheological model is implemented in the code (see next section).

4.2.4 Viscous vs. inviscid flow

As mentioned in the companion paper [*Dartevelle, 2003b*], a vast array of granular viscosities have been measured in chemical engineering, fluid dynamics, and volcanology. For instance, after the 1980 eruptions of Mt. St. Helens, *Wilson and Head* [*1981*] measured, in the newly deposited pyroclastic-flows, viscosities in the range $\mathcal{O}(10)$ to $\mathcal{O}(10^4)$ Pa·s from which they rightly suggested that concentrated pyroclastic-flows may behave plastically. It is worth noting that in our simulations when the pyroclastic-flows reaches a volumetric grain concentration of 60 vol.%, our calculated granular shear viscosities are in the same range as those measured by *Wilson and Head* [*1981*] (e.g., see Figure 21, Figure 22, and also Figure 7 in *Dartevelle* [*2003b*]). However, to date, most current numerical models of pyroclastic-flows and -surges assume either empirical low-viscosity linear rheologies (e.g., Newtonian, Bingham) or inviscid.

To compare our model with an inviscid model, we have computed simulation PL_1 assuming that there is no kinetic-collisional-plastic behavior and by systematically setting granular shear, bulk viscosities and granular plastic pressure to zero. However, it is still necessary to use the normal component of the solid stress to prevent the particles from reaching impossible high values [e.g., *Bouillard et al., 1991; Gidapsow, 1994; Neri and Macedonio, 1996; Todesco et al., 2002*]. Since we have now turned off the plastic formulation of ${}^{f}P$ [Eq.(T5.19) in *Dartevelle, 2003b*], we will use the same empirical formulation as in PDAC2D codes to roughly estimate the solid pressure [e.g., *Neri and Macedonio, 1996; Todesco et al., 2002*]:

$$\nabla P_s \approx G(\varepsilon_s)\,\nabla\varepsilon_s = 10^{-3.33+8.76\varepsilon_s}\,\nabla\varepsilon_s \qquad (3)$$

where the "compressibility modulus", $G(\varepsilon_s)$ in Pa, is an empirical best fit -among many others- of chemical engineering fluidization data [*Bouillard et al., 1991*]. $G(\varepsilon_s)$ is sometimes named "elastic modulus" and the whole expression given by Eq.(3) is named "Coulombic component" [e.g., *Neri and Macedonio*, *1996*; *Todesco et al*., *2002*], which is a misleading terminology because $G(\varepsilon_s)$ is only empirical and not related to any elasto-plastic model. Besides preventing over-compaction, $G(\varepsilon_s)$ also helps to stabilize a system of quasi-linear differential equations in which gas pressure gradient are set in both solid and gas phase momentum equations, which otherwise would lack of hyperbolicity and be ill-posed as an initial value-problem [*Lyczkowski et al., 1982; Bouillard et al., 1991; Gidapsow, 1994; Dartevelle, 2003b*]. With this in mind, it is easy to implement ∇P_s given by Eq.(3) into the momentum equations of the solid phase (Eq.(T1.6) in *Dartevelle* [*2003b*]).

Figure 23 shows the solid volumetric concentration and averaged mixture horizontal speed vs. the height at a location of 5.2 km from source for time 300 and 480 s. The full rheological model (right-side of Figure 23) shows a vertical aggradation (~64 vol.% over an height of 5 m) and a sharp decrease of U_x to nil value (i.e., deposit). The full inviscid model (left-side of Figure 23) shows no deposition and no vertical aggradation at all. Even though ε_s is as high as 66 vol.% on the ground with the inviscid model, the horizontal speed is still as high as 40 m/s, which is physically questionable for such a high concentration. Note also the very different velocity and concentration profiles higher up in the dilute part of the flow. The inviscid model makes the dilute part of the flow strongly sensitive to inward draughts, i.e., surges and co-ignimbrite flows cannot move on their own as they cannot offer any rate-of-strain "resistance" imposed by draughts, hence they "fly" along the main draught directions. The runout distance of the flow is only imposed by the severity of the counter-drafts.

5. Conclusions

We have performed plinian cloud, pyroclastic-surge and -flow simulations in order to validate and compare our numerical results with remote sensing data, historical eruptions, classical plume theories and field observations and, also, to shed new light on some of the most debated issues in volcanology about the nature and dynamic of pyroclastic-flows.

Our plinian column simulations correlate well with *Morton et al*. plume theory [*1956*] and historical eruptions in the top altitude of the cloud (H_T) vs. mass flux diagram. The high mass

flux eruption columns (>10^7 kg/s) are highly nonlinear, chaotic and subject to quasi-periodic vertical acoustic-gravity waves generated at the transition jet-plume area. H_T fluctuates with time over one-hour, hence temperature anomalies at "the tip of the top" of the cloud range between -11 K and +20 K. These results compare well with Mt. Pinatubo, El Chichón and Mt. St. Helens eruptions. The largest plinian simulation shows the development of important convective super-cell in phase with the vertical propagation of acoustic-gravity waves. The plinian simulations show complex, unsteady, and heterogeneous velocity and solid volumetric concentration profiles within the clouds (in the column and in the umbrella). To our the best of our knowledge, to date, (G)MFIX is the first multiphase model able to simulate complete plinian clouds.

The pyroclastic-flow and -surge simulations display nonlinear and highly viscous behavior. Our simulations show complex lateral flow transformation processes (pyroclastic-surges↔pyroclastic-flows). The head of the flow is diluted and has all the properties of a pyroclastic-surge, which is eventually outrun by a collisional, denser basal undercurrent pyroclastic-flow. Our simulations suggest that the depositional process is mostly gradual with materials supplied either by downstream currents or/and by sedimentation from overlying surges. However, it is shown that gradual deposition is not incompatible with *en masse* deposition. The subsequent deposit is diachronous from base to top. Deposition does not occur uniformly everywhere, e.g., our simulations show the presence of "maintained fluidized zone" near source.

In the long run, these multiphase simulations suggest that the Large Eddy Simulation (LES) should be the ideal mathematical and physical framework to further develop multiphase turbulence models in accounting for the coupling between phasic turbulence effects and in accounting for possible mass transfers between phases (e.g., Sub-Grid Mass flux for water phase change).

6. References

Agrawal, K.; P.N. Loezos; M. Syamlal; and S. Sundaresan, The role of meso-scale structures in rapid gas-solid flows, *J. Fluid Mech*., 445, 151-185, 2001.

Bouillard, J.X.; D. Gidaspow; and R.W. Lyczkowski, Hydrodynamics of fluidization: fast-bubble simulation in a two-dimensional fluidized bed, *Powder Technology*, 66, 107-118, 1991.

Boyle, E.J.; Sams, W.N.; and S.M. Cho, MFIX validation studies: December 1994 to January 1995, *DOE/FETC-97/1042 (DE97002161)*, CRADA No. PC94-026, 1998.

Braney, M.J. and P.A. Kokelaar, A reappraisal of ignimbrite emplacement: progressive aggradation and changes from particulate to non-particulate flow during emplacement of high-grade ignimbrite, *Bull. Volcanol*., 54, 504-520, 1992.

Calder, E.S.; R.S.J. Sparks; and M.C. Gardeweg, Erosion, transport and segregation of pumice and lithic clasts in pyroclastic flows inferred from ignimbrite at Lascar Volcano, Chile, *J. Volcanol. Geotherm. Res*., 104, 201-235, 2000.

Cas, R.A.F. and J.V. Wright, Volcanic Successions. Modern and Ancient, pp. 528, *Unwin Hyman, London*, 1988.

Dartevelle, S., Numerical and granulometric approaches to geophysical granular flows, Ph.D. dissertation thesis, *Michigan Technological University, Dept. of Geological and Mining Engineering*, Houghton, Michigan, 2003a.

Dartevelle, S., Numerical modeling of geophysical granular flows. I. A Review of multiphase flow model and granular rheologies, *in preparation*, *G-cubed*, 2003b.

D'Azevedo, E.; P. Sreekanth; M. Syamlal; A. Gel; M. Prinkley; and T. O'Brien, Parallelization of MFIX: A multiphase CFD code for modeling fluidized beds, *Tenth SIAM Conference on Parallel Processing for Scientific Computing Proceedings*, Portsmouth, Virginia, 2001.

Degrez, G., Implicit time-dependent methods for inviscid and viscous compressible flows, with a discussion of the concept of numerical dissipation, in Computational Fluid Dynamics. An Introduction, J.F. Wendt (ed.), 181-229, *von Karmán Institute of Fluid Dynamic, Springer*, Berlin, 1996.

Dobran, F., A. Neri, and G. Macedonio, Numerical simulations of collapsing volcanic columns, *J. Geophys. Res*., 98, 4231-4259, 1993.

Druitt, T.H., Pyroclastic density currents, in The Physics of explosive Volcanic Eruptions, J.S. Sparks and R.S.J. Sparks, eds., Geological Society, London, Special Publications, 145, 145-182, 1998.

Freundt, A., and M. Bursik, Pyroclastic flow transport mechanisms, *in* From Magma to Tephra, modeling Physical Processes of Explosive Volcanic Eruptions, A. Frendt and M. Rosi (eds.), *Elsevier*, 173-243, 1998.

Gidaspow, D., Hydrodynamics of fluidization and heat transfer: Supercomputer modeling, *Appl. Mech. Rev*., 39, 1-23, 1986.

Gidaspow, D., Multiphase flow and fluidization. Continuum and kinetic theory descriptions, 467 pp., *Academic Press*, 1994.

Guenther, C. and M. Syamlal, The effect of numerical diffusion on isolated bubbles in a gas-solid fluidized bed, Powder Technology, 116, 142-154, 2001.

Harlow, F.H. and A., Amsden, Numerical calculation of multiphase fluid flow, *J. Comp. Phys*., 17, 19-52, 1975.

Holasek, R.E. and S. Self, GOES weather satellite observations and measurements of the May 18, 1980, Mount St. Helens eruption, *J. Geophys. Res*., 100, 27,8469-8487, 1995.

Holasek, R.E.; A.W. Woods; and S. Self, Experiments on gas-ash separation processes in volcanic umbrella plumes, *J. Volcanol. Geotherm. Res*., 70, 169-181, 1996.

Ishii, M., Thermo-fluid dynamic theory of two-phase flow, 248 pp., *Eyrolles*, 1975.

Johnson, J.B., Generation and propagation of infrasonic airwaves from volcanic explosions, *J. Volcanol Geotherm. Res*., 121, 1-14, 2003.

Kapitza, H. and D. Eppel, A 3-D Poison solver based on conjugate gradients compared to standard iterative methods and its performance on vector computer, *J. Comput. Physics*, 68, 474-484, 1987.

Koch, D.L., and A.S. Sangani, Particle pressure and marginal stability limits for a homogeneous mondispersed gas-fluidized bed: Kinetic theory and numerical simulations, *J. Fluid Mechanics*, 400, 229-263, 1999.

Lakehal, D. On the modeling of multiphase turbulent flows for environmental and hydrodynamic applications, *Int. J. multiphase Flow*, 28, 823-863, 2002.

Lyczkowski R.W.; D. Gidaspow; and C.W. Solbrig, Multiphase flow models for nuclear, fossil, and biomass energy production, *in* Advances in transport processes (A.S. Mujumdar and R.A. Mashelkar eds.), 198-351, *John Wiley & Sons, New-York*, 1982.

Mikumo, T. and B.A. Bolt, Excitation mechanism of atmospheric pressure waves from the 1980 Mount St. Helens eruption, *Geophys. J. R. astr. Soc*., 81, 445-461, 1985.

Morton, B.R., G.F.R.S. Taylor, J.S. Turner, Turbulent gravitational convection from maintained and instantaneous sources, *Proc. R. Soc. London A*, 234, 1-23, 1956.

Neri, A. and G. Macedonio, Numerical simulation of collapsing volcanic columns with particles of two sizes, *J. Geophys. Res*., 101, 8153-8174, 1996.

Neri, A.; A.D. Muro; and M. Rosi, Mass partition during collapsing and transitional columns by using numerical simulations, *J. Volcanol Geotherm. Res*., 115, 1-18, 2002.

O'Rourke, P.J.; D.C. Haworth; and R. Ranganathan, Three-dimensional computational fluid dynamic, *Los Alamos National Laboratory*, LA-13427-MS, 1998.

Pannala, S.; E. D'Azevedo; M. Syamlal; T. O'Brien, Hybrid (OpenMP and MPI) Parallelization of MFIX: a multiphase CFD code for modeling fluidized beds, proceedings of ACM SAC 2003, Melbourne, Florida, 2003.

Patankar, S., Numerical heat transfer and fluid flow, pp. 197, *Hemisphere Publishing, New-York*, 1980.

Patankar, S.; K.C. Karki; and K.M. Kelkar, Finite volume method, in The Handbook of Fluid Dynamics, R.W. Johnson ed., 27-1-27-26, *CRC Press, Boca Raton*, 1998.

Press, W.H; B.P. Flannery; S.A. Teukolsky; and W.T. Vetterling, Numerical Recipes. The art of scientific computing, pp. 818, *Cambridge University Press, Cambridge*, 1986.

Rivard, W.C. and M.D. Torrey, K-FIX: A computer program for transient, two-dimensional, two-fluid flow, Los Alamos National Laboratory, LA-NUREG-6623, 1977.

Rivard, W.C. and M.D. Torrey, PERM: Corrections to the K-FIX code, Los Alamos National Laboratory, LA-NUREG-6623 Suppl., 1978.

Rivard, W.C. and M.D. Torrey, THREED: An extension of the K-FIX code for three-dimensional calculations, Los Alamos National Laboratory, LA-NUREG-6623 Suppl. II, 1979.

Rose, W.I.; A.B. Kostinski; and L. Kelley, Real-time C-band radar observations of 1992 eruption clouds from Crater Peak, Mount Spurr Volcano, Alaska, *in* The 1992 eruption of Crater Peak vent, Mount Spurr volcano, Alaska, T.E.C. Keith (Ed.), *USGS Bulletin 2139*, Washington, 19-26, 1995.

Saad, Y. and M.H. Schultz, GMRES: A generalized minimal residual algorithm for solving nonsymmetric linear systems, *SIAM J. Sci. Stat. Comput*., 7, 856-869, 1986.

Settle, M., Volcanic eruptions clouds and the thermal power output of explosive eruptions, *J. Volcanol Geotherm. Res*., 3, 309-324, 1978.

Smagorinsky, J., General circulation experiments with the primitive equations: I. The basic experiment, *Mon. Weather Rev*., 91, 99-164, 1963.

Smagorinsky, J., Some historical remarks of the use of nonlinear viscosities, *in* Large Eddy simulation of complex engineering and geophysical flows, B. Galperin and S.A. Orszag eds. , 3-36, *Cambridge University Press*, 1993.

Spalding, D.B., Numerical computation of multiphase fluid flow and heat transfer, *in* Numerical computation of multi-phase flows, J.M. Buchlin and D.B. Spalding (eds.), Lecture Series 1981-2, *von Karmán Institute for Fluid Dynamics, Rhode-Saint-Genèse, Belgium*, 1981.

Spalding, D.B., Developments in the IPSA procedure for numerical computation of Multiphase-flow phenomena with interphase slip, unequal, temperature, etc., in Numerical properties and methodologies in heat transfer, *Proc. 2nd National Symp.*, T.M. Shih (ed.), 421-436, *Hemisphere Publishing Corp., Washington*, 1983.

Sparks, R.S.J., The dimension and dynamics of volcanic eruption columns, *Bull. Volcanol*., 48, 3-15, 1986.

Sparks, R.S.J. and G.P.L. Walker, The significance of vitric-enriched air-fall ashes associated with crystal-enriched ignimbrites, *J. Volcanol. Geotherm. Res*., 2, 329-341, 1977.

Sparks, R.S.J.; L. Wilson; and G. Hulmes, Theoretical modeling of the generation, movement and emplacement of pyroclastic flows by column collapse, *J. Geophsys. Res*., 83, 1727-1739, 1978.

Sparks, R.S.J.; M.I. Bursik; S.N. Carey; J.S. Gilbert; L.S. Glaze; H. Sigurdson; and A.W. Woods, Volcanic plumes, *John Wiley and Sons, Chichester*, pp. 574, 1997.

Syamlal, M., W. Rogers, and T.J. O'Brien, MFIX documentation. Theory Guide, pp. 49, *U.S. Dept. of Energy*, DOE/METC-94/1004, DE94000097, 1993.

Syamlal, M., MFIX documentation. User's manual, pp. 87, *U.S. Dept. of Energy*, DOE/METC-95/1013, DE95000031, 1994.

Syamlal, M., MFIX documentation. Numerical Technique, pp. 80, *U.S. Dept. of Energy*, DOE/MC/31346-5824, DE98002029, 1998.

Tahira, M.; M. Nomura; Y. Sawada; and K. Kamo, Infrasonic and acoustic-gravity waves generated by the Mount Pinatubo eruption of June15, 1991, *in* Fire and Mud, Eruptions and lahars of Mount Pinatubo, Philippines, C.G. Newhall and R.S. Punonybanan (eds.), *PHIVOLCS-USGS*, Quezon City, Seattle, 601-613, 1996.

Todesco, M., A. Neri, T. Esposti Ongaro, P. Papale, G. Macedonio, R. Santacroce, and A. Longo, Pyroclastic flow hazard assessment at Vesuvius (Italy) by using numerical modeling. I. Large-scale dynamics, *Bull. Volcanol*., 64, 155-177, 2002.

Valentine, G.A. and K.H. Wohletz, Numerical models of plinian eruption columns and pyroclastic flows, *J. Geophys. Res*., 94, 1867-1887, 1989.

Valentine, G.A.; K.H. Wohletz; and S. Kieffer, Sources of unsteady column dynamics in pyroclastic flow eruptions, *J. Geophys. Res*., 96, 21887-21892, 1991.

Van der Vorst, H.A., BI-CGSTAB: A fast and smoothly converging variant of BI-CG for the solution of nonsymmetric linear systems, *SIAM J. Sci. Stat. Comput*., 13, 631-644, 1992.

Walker, G.P.L., Origin of coarse lithic breccias near ignimbrite source vents, *J. Volcanol. Geotherm. Res*., 25, 157-171, 1985.

Wilson, L., R.S.J. Sparks, T.C. Huang, and N.D. Watkins, The control of volcanic column heights by eruption energetic and dynamics, *J. Geophys. Res*., 83, 1829-1836, 1978.

Wilson, L. and J.W. Head, Morphology and rheology of pyroclastic flows and their deposits, and guidelines for future observations, *in* The 1980 eruption of Mount St. Helens, Washington, P.W. Lipman and D.R. Mullineaux (eds.), 513-524, *U.S.G.S. professional paper 1250, Washington D.C*., 1981.

Woods, A.W. and K. Wohletz, Dimensions and dynamics of co-ignimbrite eruptions columns, *Nature*, 350, 225-227.

Woods, A.W. and C.-C. P. Caulfield, A laboratory study of explosive volcanic eruptions, *J. Geophys. Res*., 97, 6699-6712, 1992.

Wen, S. and W.I. Rose, Retrieval of sizes and total masses of particles in volcanic clouds using AVHRR band 4 and 5, *J. Geophys. Res*., 99, 5421-5431, 1994.

Woods, A.W. and S. Self, Thermal disequilibrium at the top of volcanic clouds and its effect on estimates of the column height, *Nature*, 355, 628-630, 1992.

Zehner, P. and E.U. Schlunder, Warmeleiftahigkeit von Schuttungen bei maβigen Temperaturen, *Chemie-Ingenieur-Technik*, 42, 933-941, 1970.

Zurn, W. And R. Widmer, Worlwide observation of bichromatic long-period Rayleigh waves excited during the June 15, 1991, eruption of Mount Pinatubo, *in* Fire and Mud, Eruptions and lahars of Mount Pinatubo, Philippines, C.G. Newhall and R.S. Punonybanan (eds.), *PHIVOLCS-USGS*, Quezon City, Seattle, 615-624, 1996.

Table, Figure, Movie, and Annex captions

Table 7

A. Geometry, Initial and boundary conditions, and various physical properties used for all the simulations (see also Figure 10). In Cylindrical geometry, the mass flux at the vent is calculated by $\pi.r^2.V_y.\rho_m$, where V_y is defined by Eq.(1) and ρ_m by Eq.(2). In Cartesian geometry, the mass flux is calculated by $r^2.V_y.\rho_m$, where r^2 is the surface area made by the dimension of a fissure-like vent along the X- and Z-directions (i.e., 100 m in both directions). The third dimension (Z-direction) is made of only one cell, hence there is no discretization of the differential equations along Z. The length in the Z-direction is 100 m in Cartesian geometry and is equal to arctg(1)·X in Cylindrical geometry, where X is the length of the domain along the X-direction. **B**. Identical atmospheric conditions for all simulations, i.e., a temperate, dry, idle standard atmosphere.

Figure 9

History of the "FIX" family computer codes used in chemical engineering, nuclear reactor dynamic, and geophysics-volcanology. For K-FIX codes, see *Rivard and Torrey* [*1977*], *Rivard and Torrey* [*1978*] and *Rivard and Torrey* [*1979*] and its use in volcanology (DASH code), e.g., see *Valentine and Wohletz* [*1989*] and *Valentine et al.,* [*1991*]; for PDAC2D codes and its earlier versions in volcanology, e.g., see *Dobran et al.* [*1993*], *Neri and Macedonio* [*1996*], *Neri et al.* [*2002*] and *Todesco et al.* [*2002*]; for IIT and related codes, e.g., see *Gidaspow* [*1986*], for NIMPF and MFIX codes, e.g., see *Syamlal et al.* [*1993*], *Syamlal* [*1994*], *Syamlal* [*1998*], *D'Azevedo et al.* [*2001*], *Pannala et al.* [*2003*], and *Dartevelle* [*2003a*]. The exact relationship between DASH and K-FIX is simplified as some intermediary codes may be involved (K. Wohletz, Los Alamos National Laboratory, personal communication, 2003).

Figure 10

A. Axisymmetric (Cylindrical) geometry for plinian cloud simulations (PL-group). **B.** Cartesian geometry for pyroclastic-surge and -flow simulations (PSF-group). For both group, the vent is next to the free-slip left side vertical wall. See Table 7A for the dimension of the computational domain. δx, δy, and δz represent the elemental length of a computational cell in the X-, Y-, and Z-direction respectively. As shown on these figures all simulations are in 2D, which means there is no discretization along the Z-direction (i.e., Z-length = δz).

Figure 11

Time sequence over one hour of three plinian clouds. The color code represents the logarithm of the volumetric solid concentration ($\log_{10}\varepsilon_s$): the redder, the more concentrated, the bluer the more diluted (the blue atmosphere has initially no grains). **A**. Simulation PL_1 (3.15×10^6 kg/s). **B**. Simulation PL_2 (2.41×10^7 kg/s). **C**. Simulation PL_3 (1.39×10^8 kg/s). It is worth noting the heterogeneity in grain volumetric concentration throughout the whole plinian flow (column and umbrella) and the very low grain concentration veil at the top of the plinian column and surrounding its umbrella.

Figure 12

Variation of the top altitude of the column (H_T) with time (between 0 and 3600 s) for the three plinian column simulations. Note the fluctuating and pulsating behavior of PL_2 and PL_3 clouds with time.

Figure 13

Radial speed profiles (U_x in m/s) along the vertical direction (between 0 and 14 km) at different radial positions within the plinian cloud for simulation PL_1. The gray background color of the cloud represents the intensity of volumetric solid concentration gradient in any direction (the steeper the gradient, the darker). Note backwards radial draughts shearing the umbrella and explaining its finger-like morphology.

Figure 14

Radial speed profiles (U_x in m/s) along the vertical direction (between 0 and 30 km) at different radial positions within the plinian cloud for simulation PL_3. Same gray background color as in Figure 13.

Figure 15

Vertical speed profiles (V_y in m/s) along the radial direction (between 0 and 10 km) at different altitudes within the plinian cloud for simulation PL_3. Same gray background color as in Figure 13.

Figure 16

Vertical profiles within the plinian column PL_3 taken at 3600 s. **A**. Averaged mixture temperature (T_m in K) calculated by Eq.(1). **B**. Acoustic pressure: difference between the gas pressure inside the column and the undisturbed atmospheric pressure ($\Delta P_g=P_g-P_{atm}$ in daPa where 100 daPa=1000 Pa=10 hPa). **C**. Averaged mixture vertical speed (V_y in m/s). **D**. Density anomalies: difference between the atmospheric density and the gas macroscopic density within the column ($\Delta\rho_g=1-\varepsilon_g\rho_g/\rho_{atm}$) or the solid macroscopic density ($\Delta\rho_s=1-\varepsilon_s\rho_s/\rho_{atm}$) within the plinian column (in %). Note at 3.9 km, where the system is expanding the most, the sharp decrease in temperature (by nearly 200 K), hence the slight decrease in buoyancy of the gas phase but the dramatic increase of buoyancy of the solid phase (dilution).

Figure 17

Top altitude of the plinian cloud (H_T in km) vs. mass flux at the volcanic vent (kg/s). Triangle are for historical eruptions from which H_T and the mass flux has been inferred from field studies and remote sensing observations (i.e., not inferred by some previous modeling) [data from *Wilson et al., 1978; Settle, 1978; Sparks et al. 1997*]; dash-curve is the best regression fit between these historical eruption data; plain curve are from *Morton et al*. [*1956*] theory calculated for two initial magma temperatures at the vent (600 K and 1200 K); and circles are for (G)MFIX's three plinian simulations. Knowing all the uncertainties of historical eruptions for determining the mass flux at the vent and H_T, we may conclude that there is an excellent agreement between (G)MFIX's simulations and past historical eruptions.

Figure 18

Top height of the PL_3 cloud (H_T, left vertical axis) and temperature anomalies at the top of the cloud relative to the ambient ($\Delta T=T_m-T_{atm}$, right vertical axis) vs. time (between 0 and 3600 s). The horizontal line represents $\Delta T=0$ K.

Figure 19

Time sequence over 8 minutes of simulation PF_1 ($1.78x10^7$ kg/s). **A**. Time between 30 and 180 s. **B**. Time between 210 and 480 s. The curves represent the logarithm of the volumetric solid concentration ($\log_{10}\varepsilon_s$) between -1 and -9 (the atmosphere has initially no grain). Size of the domain: 10 km (radial) x 2.5 km (height). The computational domain is initially much bigger but beyond 10 km and 2.5 km the grid resolution is so poor that it has no practical interest to be shown. The poor grid resolution to higher altitudes explains why the co-ignimbrite (phoenix) clouds have such a vertical elongated shape.

Figure 20

Time sequence over 8 minutes of simulation PF_2 ($8.89x10^6$ kg/s). **A**. Time between 30 and 180 s. **B**. Time between 210 and 480 s. Same volumetric concentration curves, domain size and comments as in Figure 19.

Figure 21

Various time and space sampling along an height of 100 m within the flow PF_1. **A**. Sampling at different position and time within the head of the flow; from left to right: volumetric grain concentration (ε_s in vol.%), mean mixture horizontal speed (U_x in m/s), granular-temperature (Θ in m^2/s^2), and granular shear viscosity (in Pa·s). **B**. Sampling of ε_s and U_x at a fixed position 250 m from source at different time (60, 100, 180, 480 s). **C**. Same sampling as in Figure 21B but at 2.5 km from source. **D**. Sampling of ε_s, U_x, Θ, and granular shear viscosity at a fixed position 5 km from source for different time (100, 180, 300, 480 s).

Figure 22

Various time and space sampling along an height of 100 m within the flow PF_2. **A**. Sampling at different position and time within the head of the flow; from left to right: volumetric grain concentration (ε_s in vol.%), mean mixture horizontal speed (U_x in m/s), granular-temperature (Θ in m^2/s^2), and granular shear viscosity (in Pa·s). **B**. Sampling of ε_s and U_x at a fixed position 250 m from source at different time (60, 100, 180, 480 s). **C**. Same sampling as in Figure 22B but at 2.5 km from source for time 100, 180, and 480 s. **D**. Sampling of ε_s, U_x, Θ, and granular shear viscosity at a fixed position 3.7 km from source for different time (200, 300, 480 s).

Figure 23

Comparison of numerical results from a fully inviscid model (left-side) and a full rheological granular model (right-side) involving kinetic-collisional and plastic formulations as in *Dartevelle* [*2003b*]. Sampling at a fixed distance of 5.2 km from source at two different times (300 and 480 s). **A**. Volumetric grain concentration vs. height in the flow. **B**. Averaged mixture horizontal speed vs. height. The inviscid model is unable to build up a deposit (no vertical aggradation) and to stop. i.e., the horizontal speed is higher than 40 m/s for concentrations as high as 66 vol.%.

Movie 1

One hour development of the plinian column PL_1 ($3.15x10^6$ kg/s). The color bar represents the logarithm of the solid volumetric concentration ($\log_{10}\varepsilon_s$) between 10^{-2} and 10^{-9}: the redder, the more concentrated, the bluer the more diluted. Size of the domain: 20 km (radial) x 18 km (height).

Movie 2

One hour development of the plinian column PL_2 (2.41×10^7 kg/s). Same color bar as in Movie 1. Size of the domain: 40 km (radial) x 25 km (height).

Movie 3

One hour development of the plinian column PL_3 (1.39×10^8 kg/s). Same color bar as in Movie 1. Size of the domain: 60 km (radial) x 36 km (height).

Movie 4

One hour development of temperature anomalies within the plinian cloud PL_3 (1.39×10^8 kg/s). We have only mapped the temperature anomalies between -15 K and +15 K for better rendering; hence any ΔT below -15 K is made equal to -15 K and any value higher than +15 K is made equal to +15 K. Size of the domain: 60 km (radial) x 36 km (height).

Movie 5

8 minutes development of simulation PF_1 (2.26×10^7 kg/s). The color bar represents the logarithm of the solid volumetric concentration ($\log_{10}\varepsilon_s$) between 0.64 and 10^{-9}: the redder, the more concentrated, the bluer the more diluted. Size of the domain: 10 km (radial) x 2.5 km (height). The computational domain is initially much bigger but beyond 10 km and 2.5 km the grid resolution is so poor that it has no practical interest to be shown. The poor grid resolution at higher altitudes explains why the co-ignimbrite (phoenix) clouds have such a vertical elongated shape.

Movie 6

8 minutes development of simulation PF_2 (1.13×10^7 kg/s). Same color bar, domain size and comments as in Movie 5.

Annex 5

Grid-size independence study for two plinian column simulations.

Annex 6

Overview of the numerical schemes used in MFIX and (G)MFIX: SIMPLE algorithm, Partial Elimination Algorithm, automatic time-stepping adjustment, and parallel features. Table 9 decomposes the SIMPLE algorithm for each equations and shows its relationship with the PEA and linear equations solvers used in this project.

Table 7A:

Eruption	Plinian PL-group			Pyroclastic-flows and -surges PSF-group		
	PL_1	**PL_2**	**PL_3**	**PF_1**	**PF_2**	**PF_3** (inviscid)
Geometry	Cylindrical			Cartesian		
Radial/Horizontal length X (km)	20	40	60	18	18	18
Radial/Horizontal resolution ΔX (m)	30 to 1000	50 to 1000	80 to 1000	10 to 800	10 to 800	10 to 800
Number of grid-points in the X-direction	145	168	150	950	950	950
Vertical length Y (km)	18	25	36	10	10	10
Vertical resolution ΔY (m)	30	50	80	2.5 to 1000	2.5 to 1000	2.5 to 1000
Number of grid-points in the Y-direction	601	501	401	95	95	95
Vent diameter/length r (m)	120	400	800	100	100	100
Mixture vertical speed V_y (m/s)	110	110	160	50	25	50
Volumetric solid concentration ε_s (vol.%)	0.1	0.1	0.1	3.0	3.0	3.0
Grain diameter d (μm)	50	50	50	250	250	250
Grain microscopic density ρ_s (kg/m^3)	1500	1500	1500	2500	2500	2500
Mixture temperature at the vent T_m (K)	900	900	900	900	900	900
Gas pressure at the vent P_g (Pa)	10^5	10^5	10^5	10^5	10^5	10^5
Mass fraction of water vapor at the vent	1.0	1.0	1.0	1.0	1.0	1.0
Calculated mixture density ρ_m (kg/m^3)	1.74	1.74	1.74	45.2	45.2	45.2
Calculated mass flux (kg/s)	$3.15\text{x}10^6$	$2.41\text{x}10^7$	$1.39\text{x}10^8$	$2.26\text{x}10^7$	$1.13\text{x}10^7$	$2.26\text{x}10^7$

Table 7B:

Atmospheric properties	
Pressure at vent level	10^5 Pa
Temperature at vent level	298 K
Calculated gas density at vent level	1.169 kg/m^3
Vapor mixing ratio at vent level	0 (dry atmosphere)
Tropospheric temperature gradient (0 – 11 km)	-7 K/km (temperate atmosphere)
Lower stratospheric temperature gradient (19 – 32 km)	+1.8 K/km
Upper stratospheric temperature gradient (32 – 47 km)	+2.8 K/km
Tropopause	11 – 19 km

Chapter 3 - Figure 9

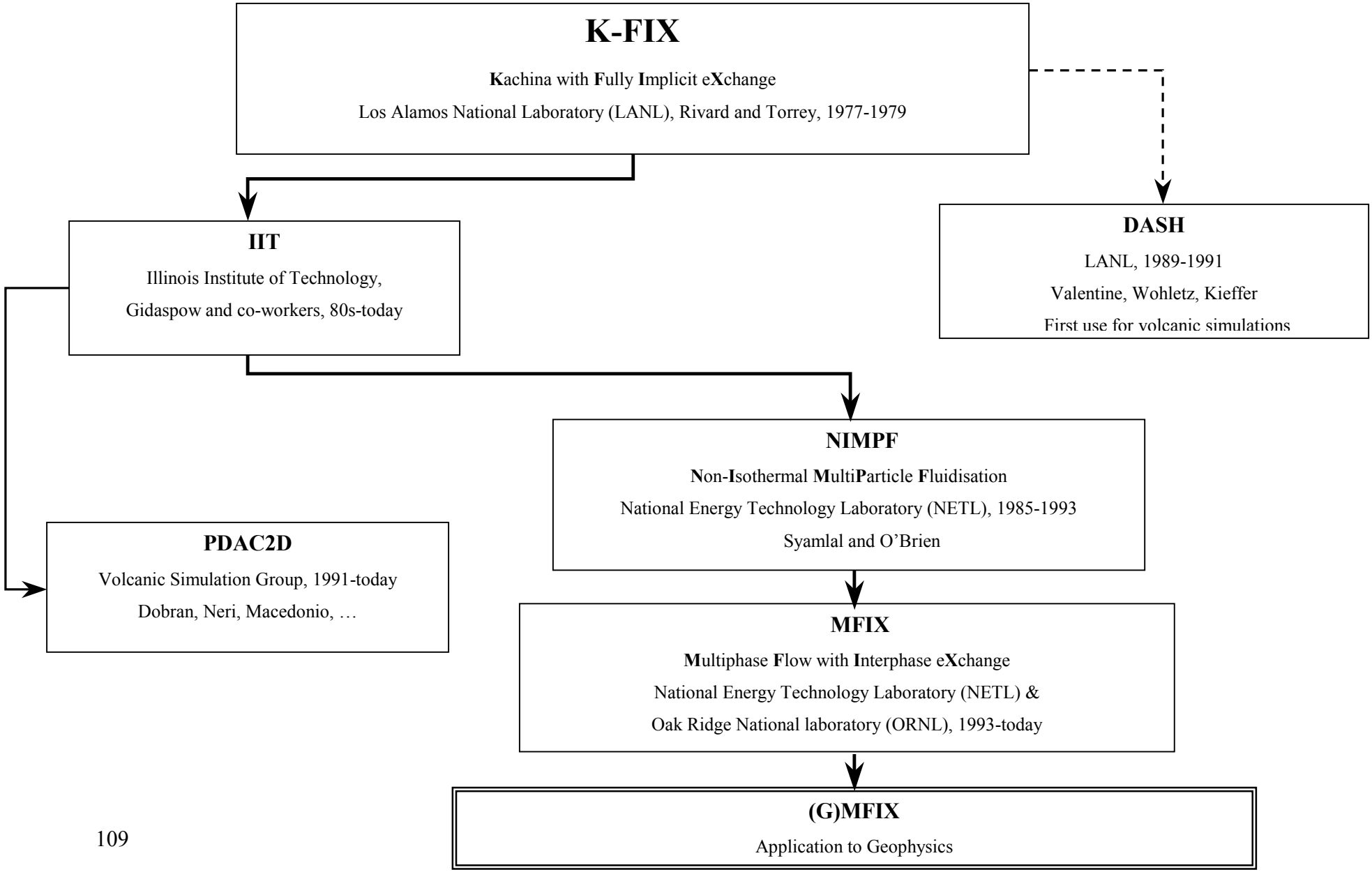

Chapter 3 - Figure 10

A.

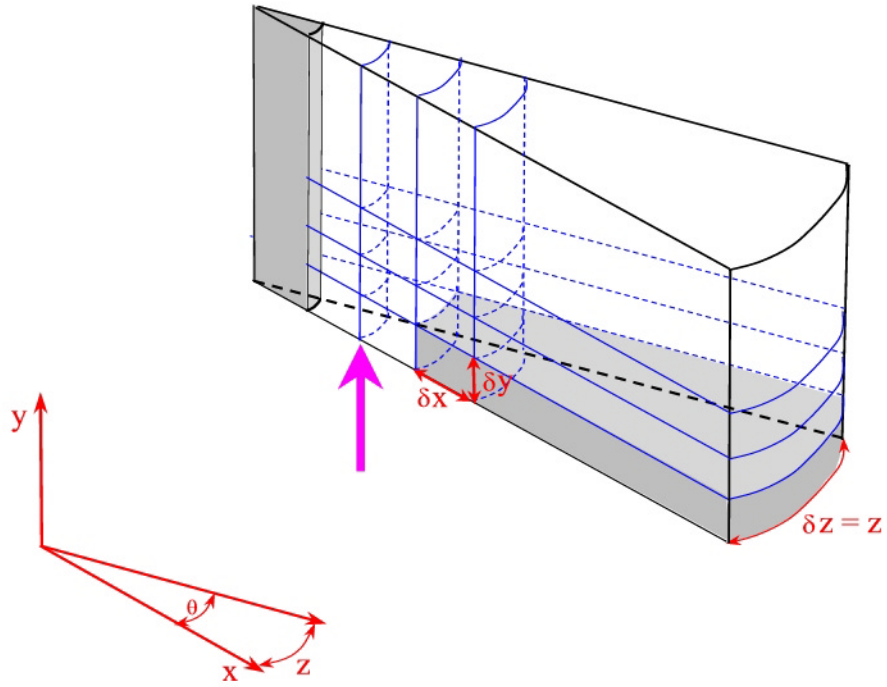

B.

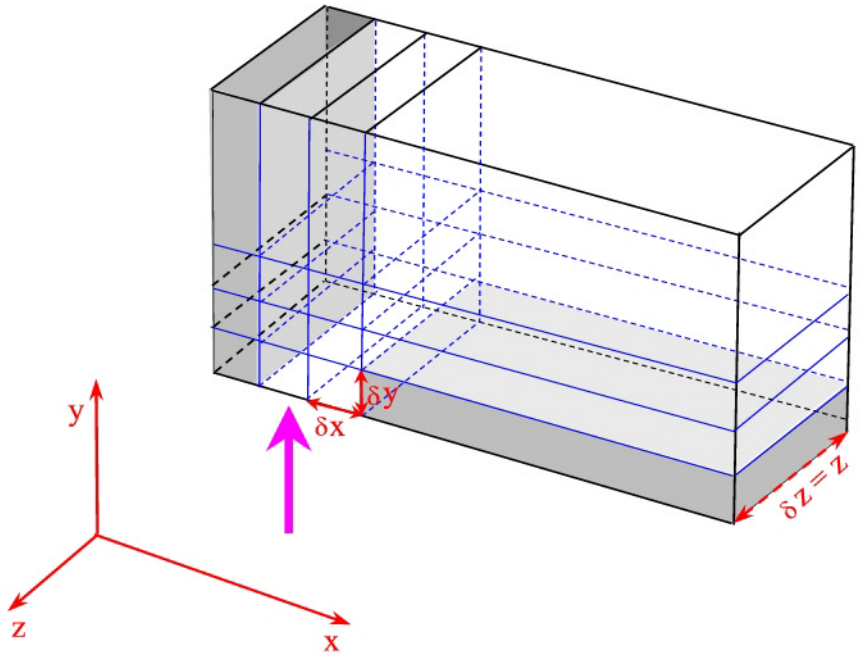

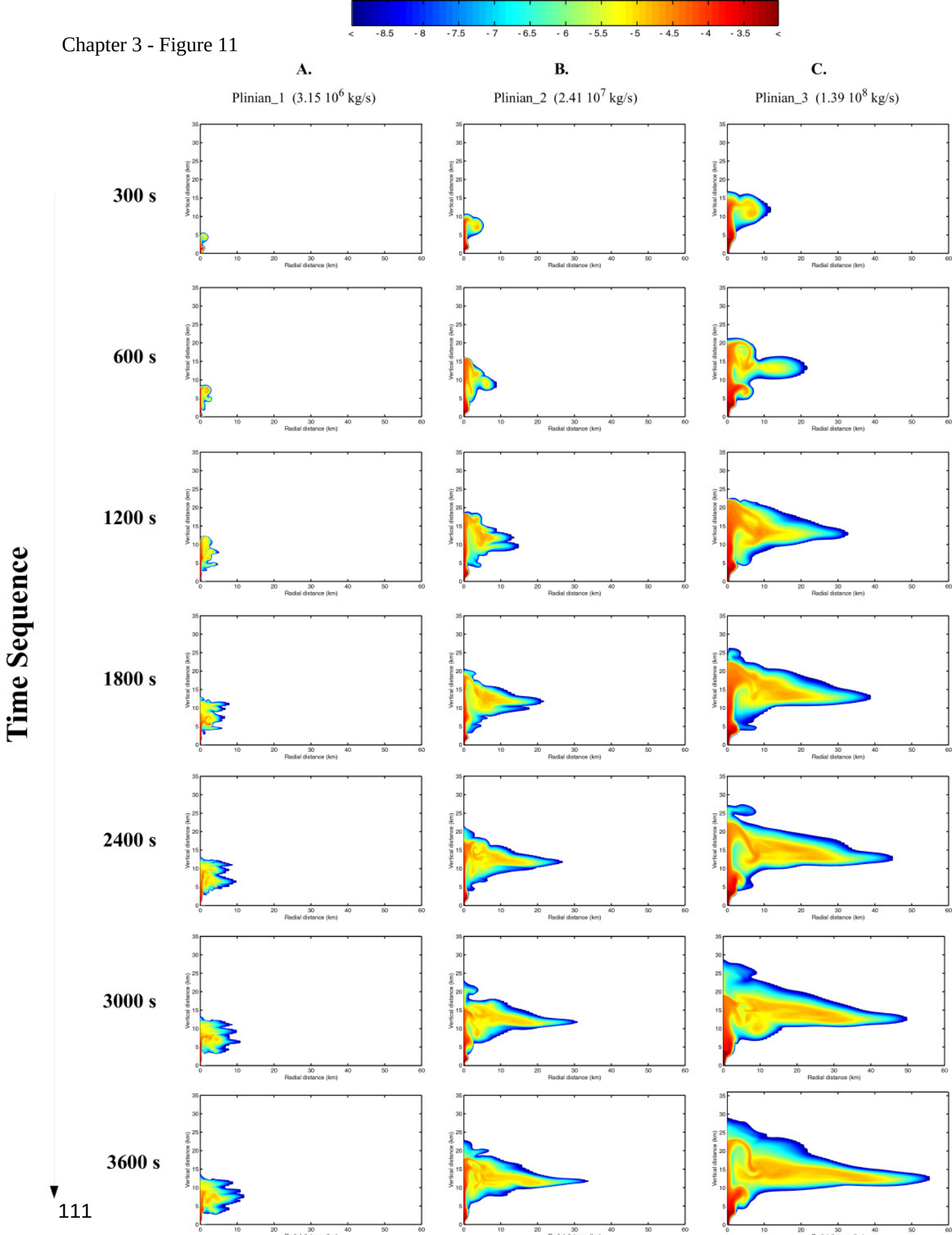
< -8.5 -8 -7.5 -7 -6.5 -6 -5.5 -5 -4.5 -4 -3.5 <
A.
B.
C.
Plinian_1 (3.15 10^6 kg/s)
Plinian_2 (2.41 10^7 kg/s)
Plinian_3 (1.39 10^8 kg/s)
300 s
600 s
1200 s
1800 s
2400 s
3000 s
3600 s
Time Sequence
Vertical distance (km)
Radial distance (km)

Chapter 3 - Figure 12

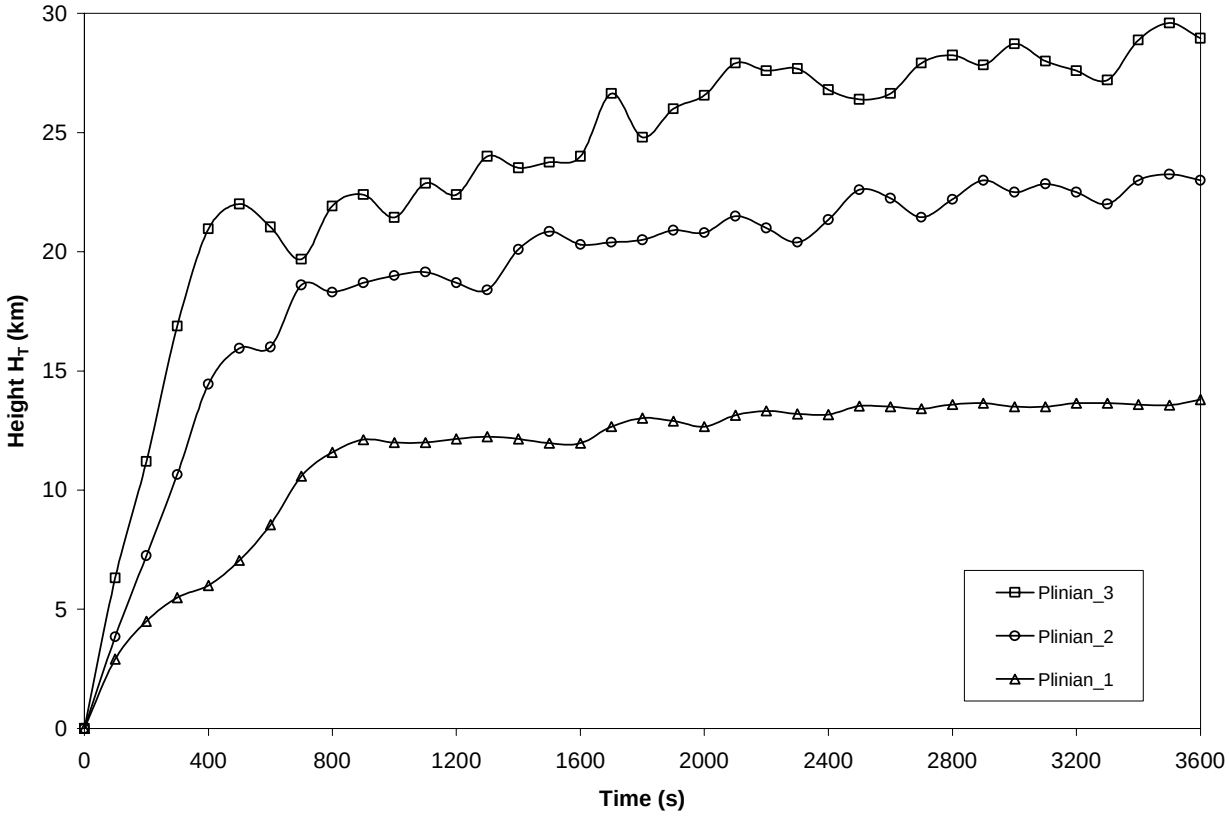

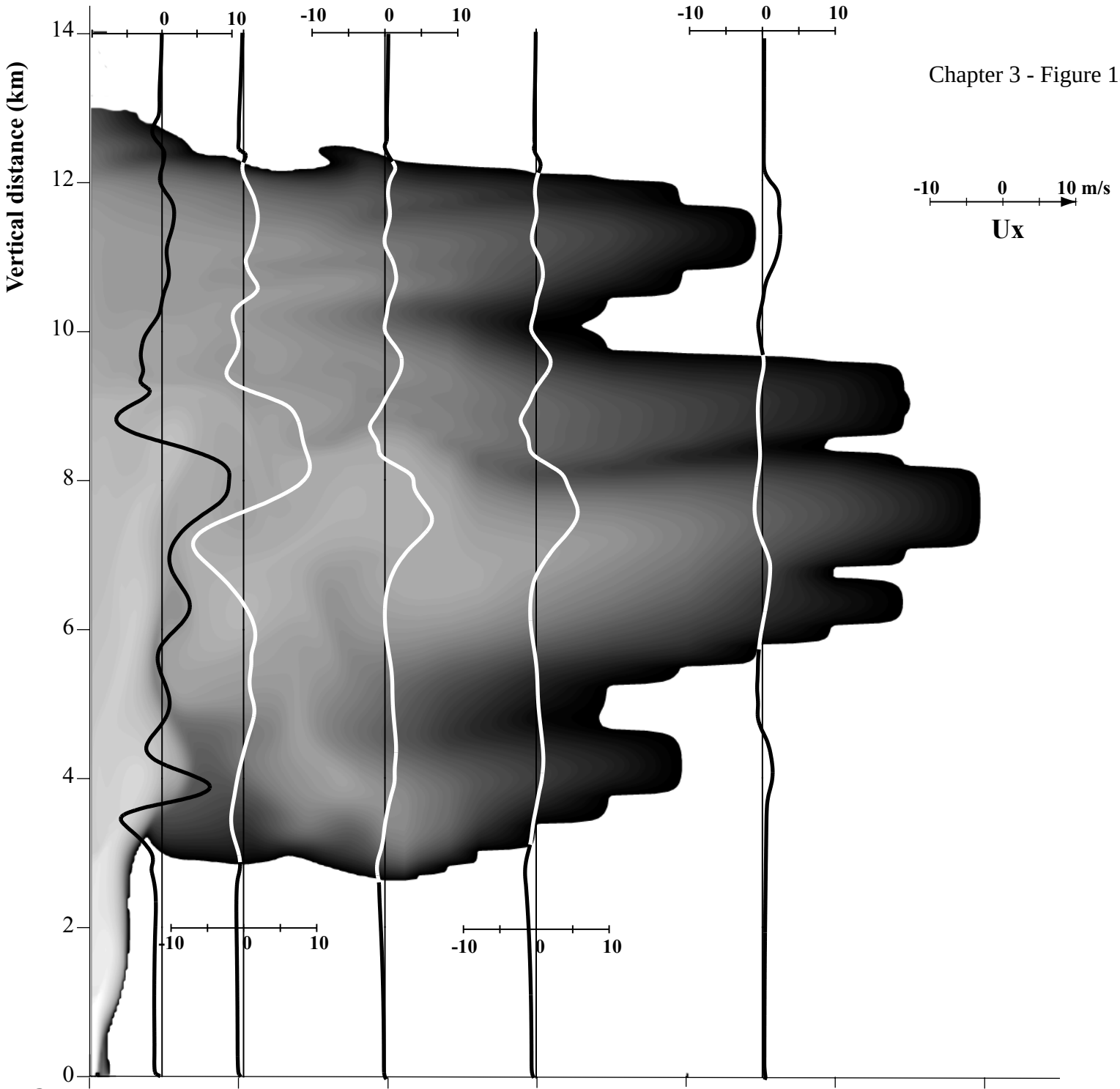
Vertical distance (km)
Radial distance (km)
Ux
-10 0 10 m/s
0
2
4
6
8
10
12
14

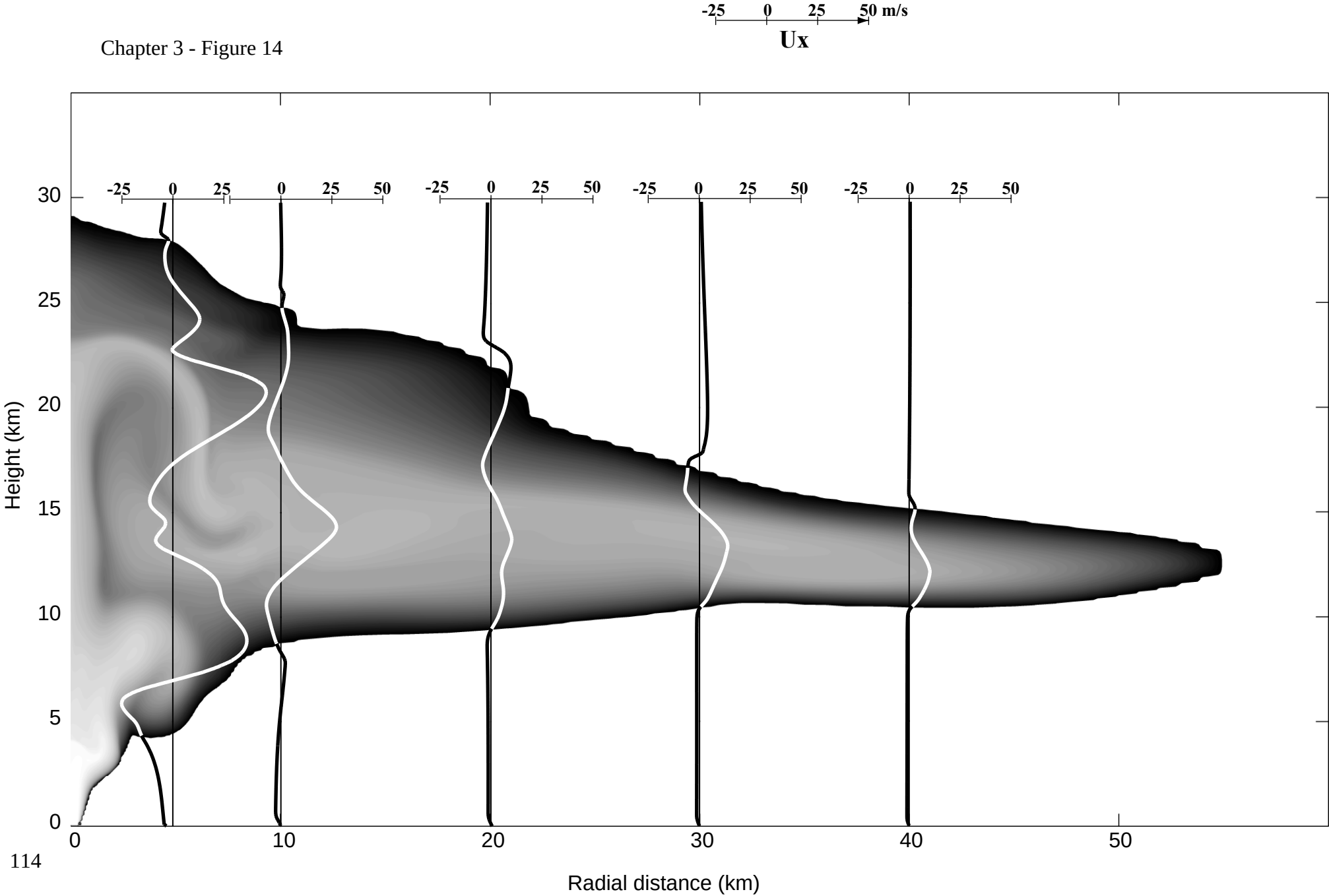
-25 0 25 50 m/s
Ux
-25 0 25 0 25 50 -25 0 25 50 -25 0 25 50 -25 0 25 50
Height (km)
0
5
10
15
20
25
30
0
10
20
30
40
50
Radial distance (km)

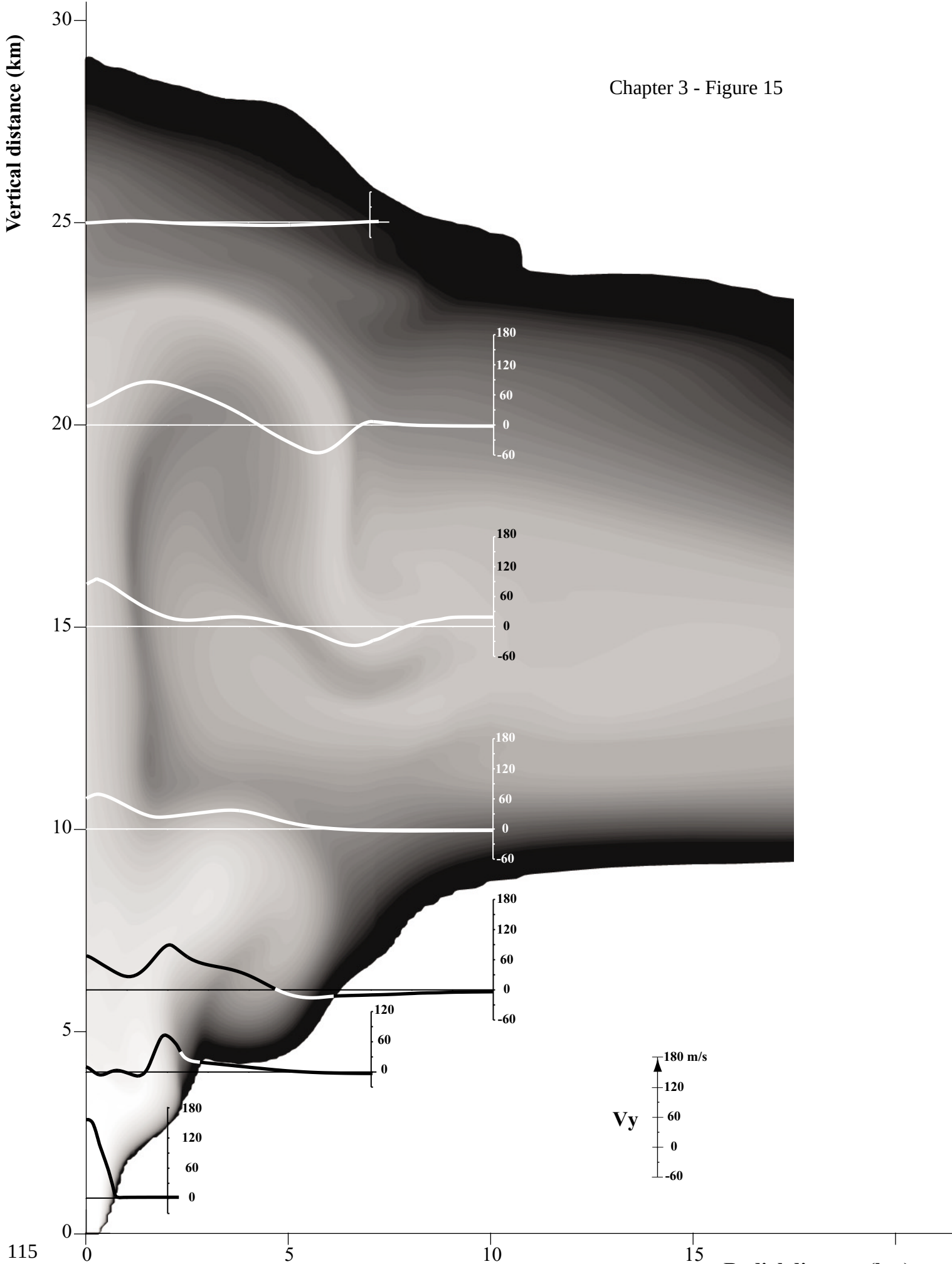
Vertical distance (km)
30
25
20
15
10
5
0
180
120
60
0
-60
Vy
180 m/s
0
5
10
15
Radial distance (km)

Profiles in the plinian column PL_3 at 3600 s

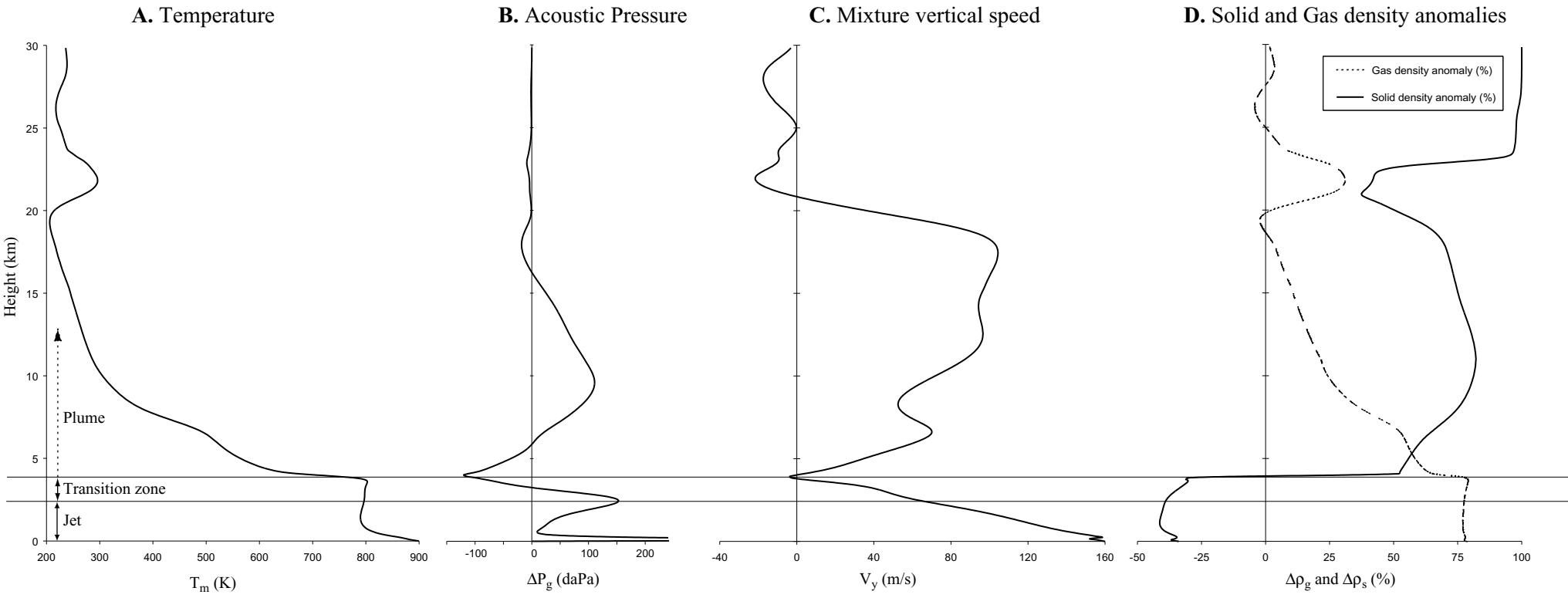

Chapter 3 - Figure 17

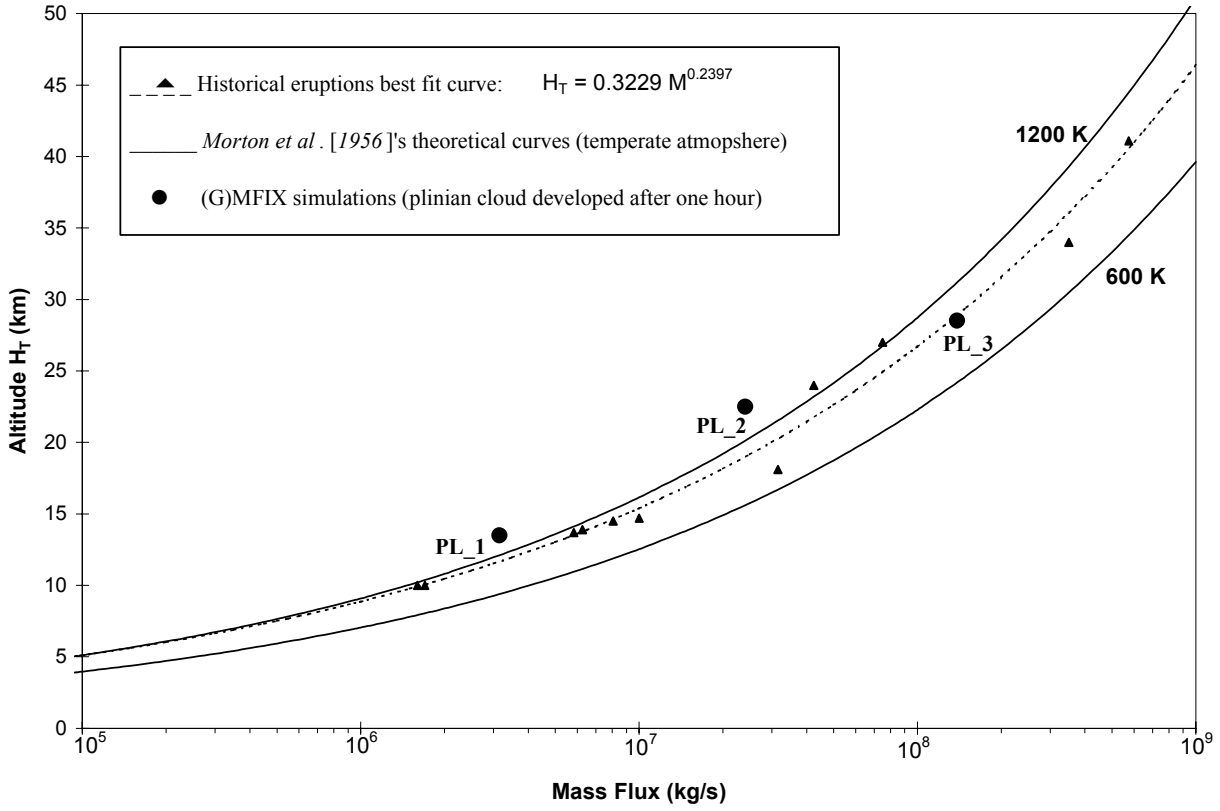

Chapter 3 - Figure 18

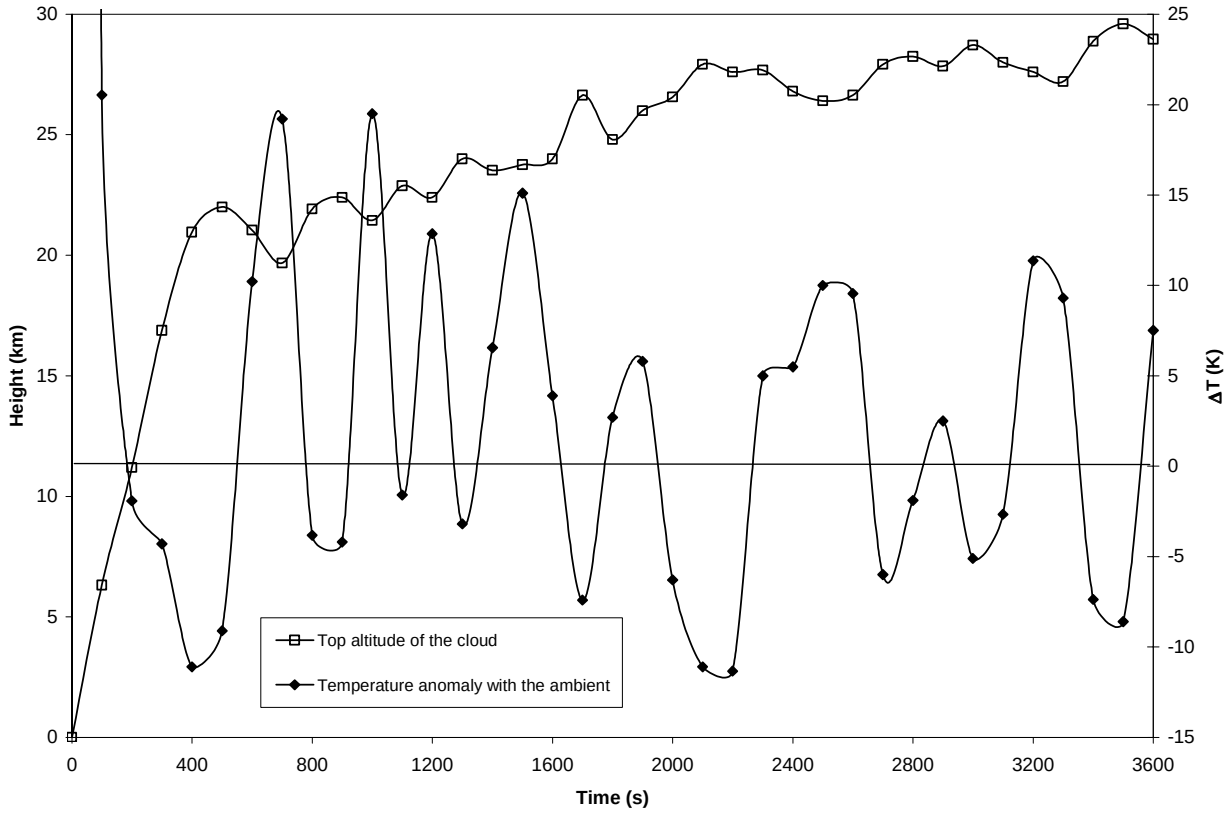

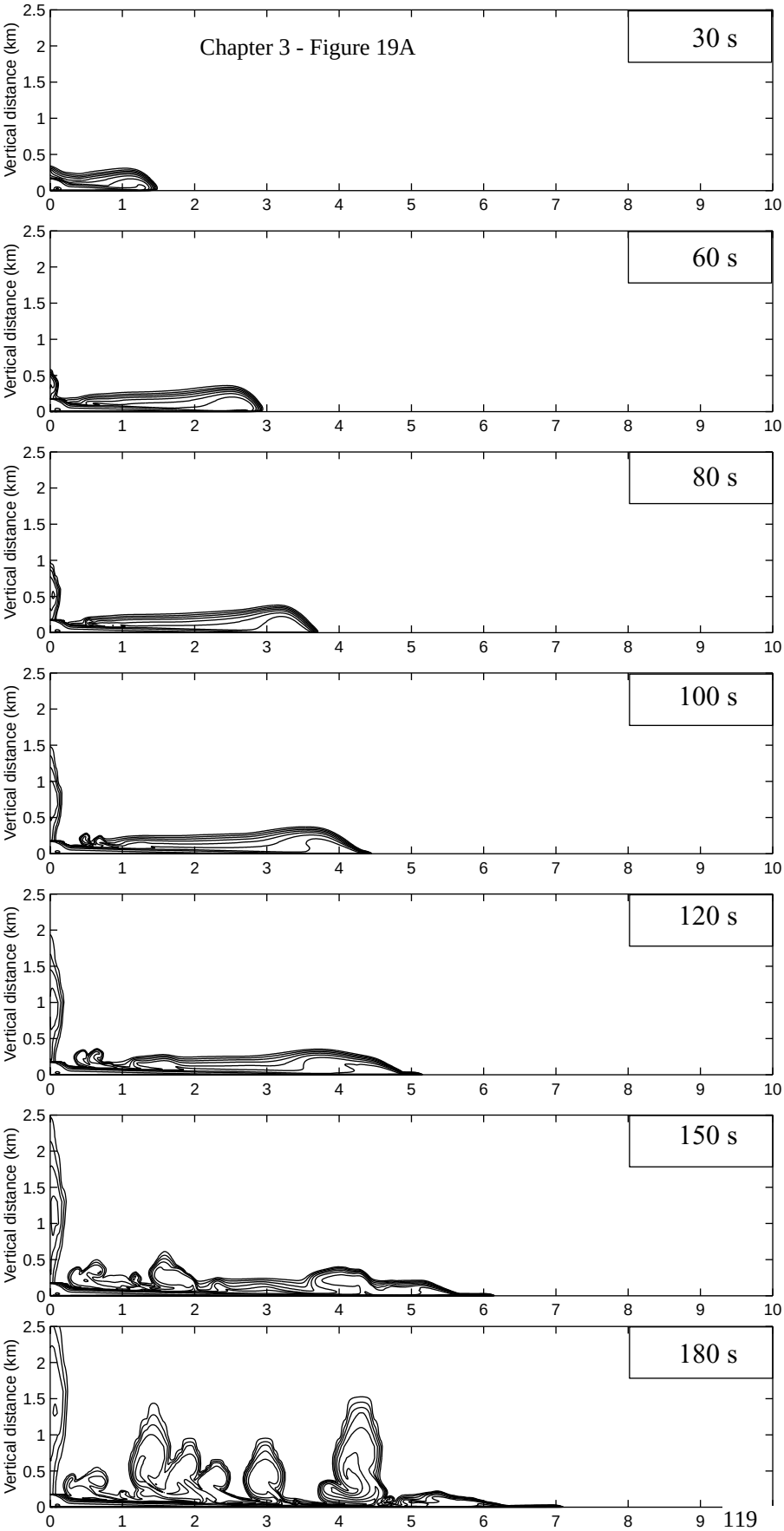
Chapter 3 - Figure 19A
30 s
60 s
80 s
100 s
120 s
150 s
180 s
Vertical distance (km)
Radial distance (km)

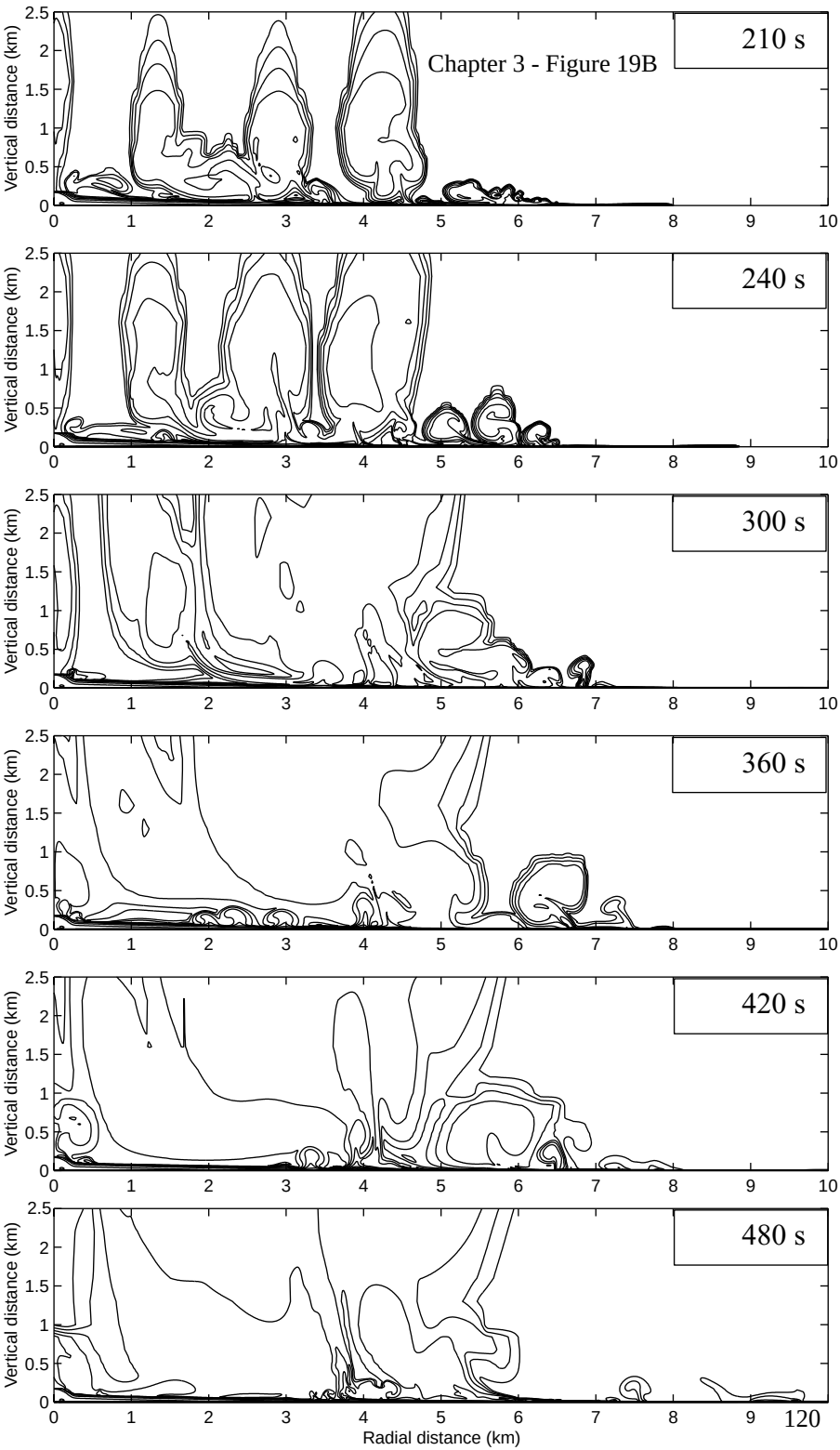
Chapter 3 - Figure 19B
210 s
240 s
300 s
360 s
420 s
480 s
Vertical distance (km)
Radial distance (km)
0
0.5
1
1.5
2
2.5
3
4
5
6
7
8
9
10

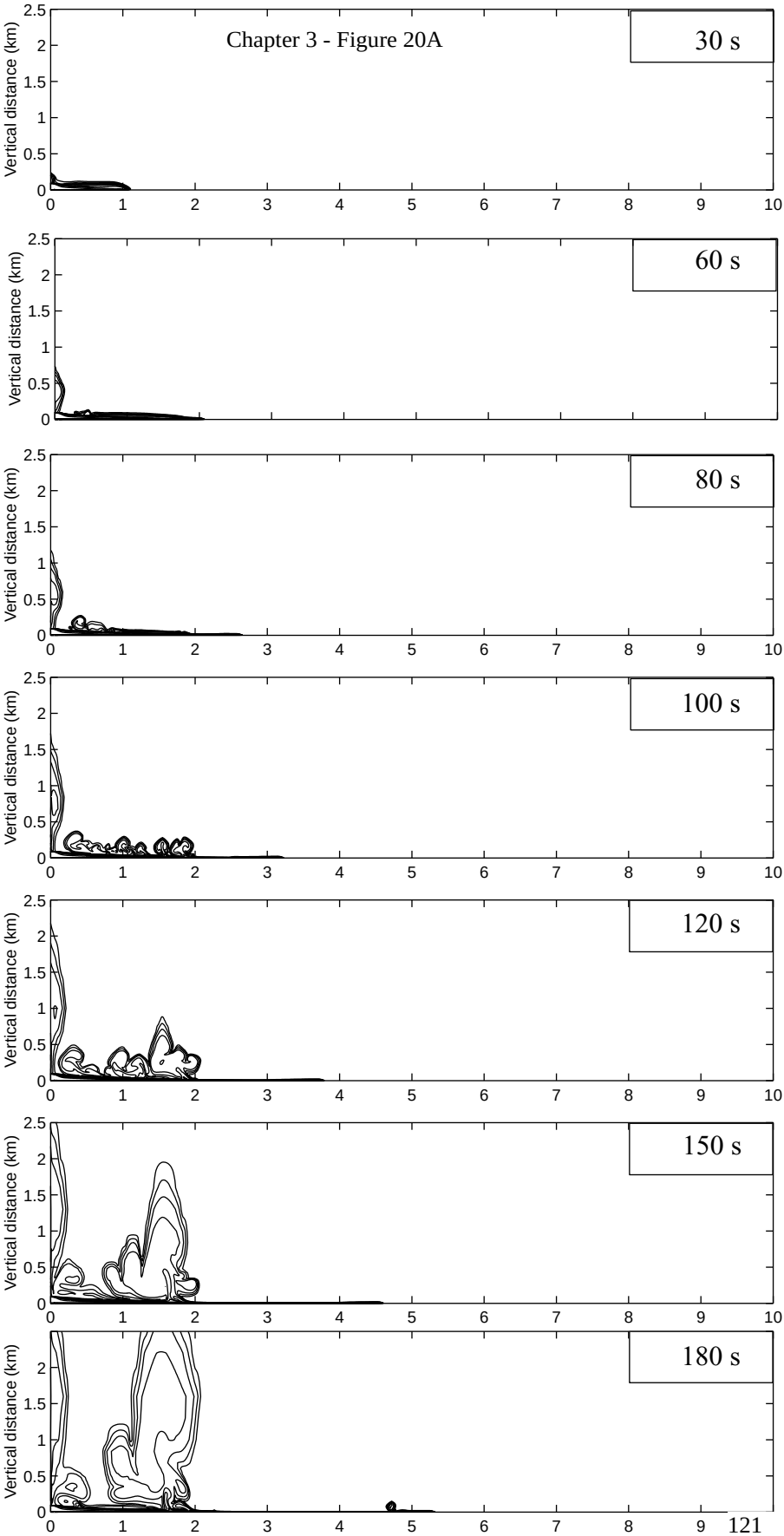
Chapter 3 - Figure 20A
30 s
60 s
80 s
100 s
120 s
150 s
180 s
Vertical distance (km)
Radial distance (km)

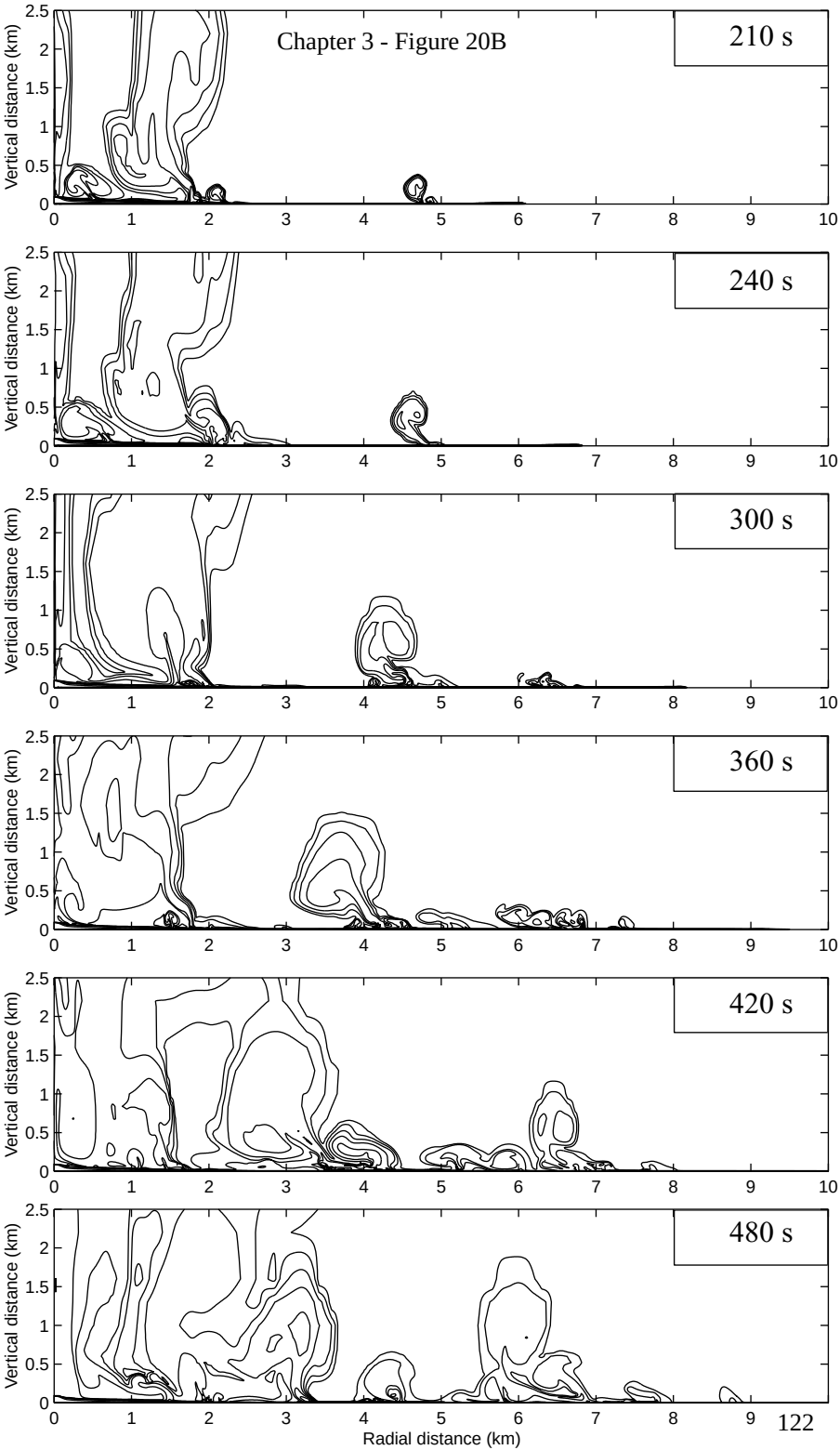
Chapter 3 - Figure 20B
210 s
240 s
300 s
360 s
420 s
480 s
Vertical distance (km)
Radial distance (km)

A. Variable position and time sampling within the head of the flow:

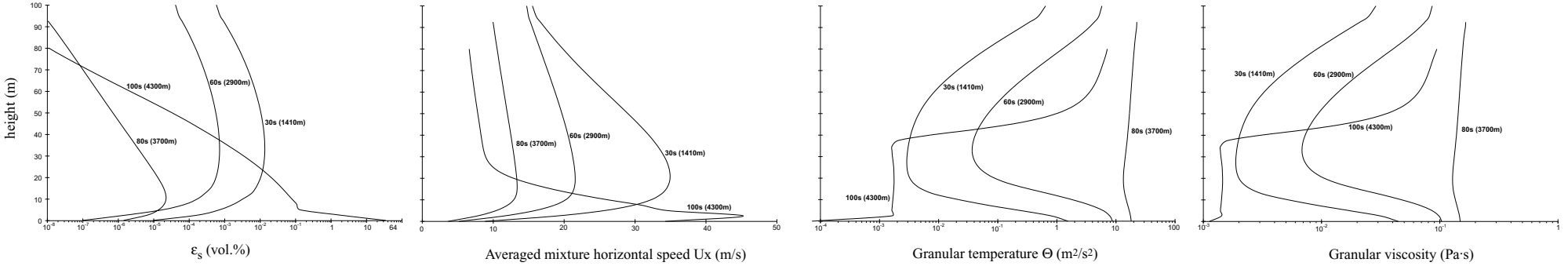

B. Fixed position sampling at 0.25 km from source:

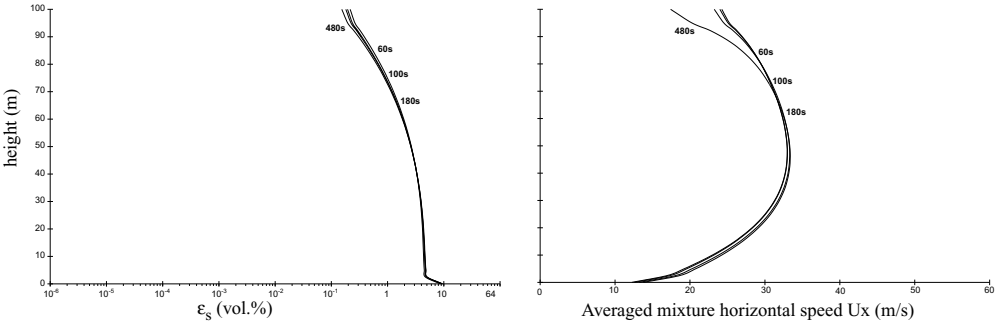

C. Fixed position sampling at 2.5 km from source:

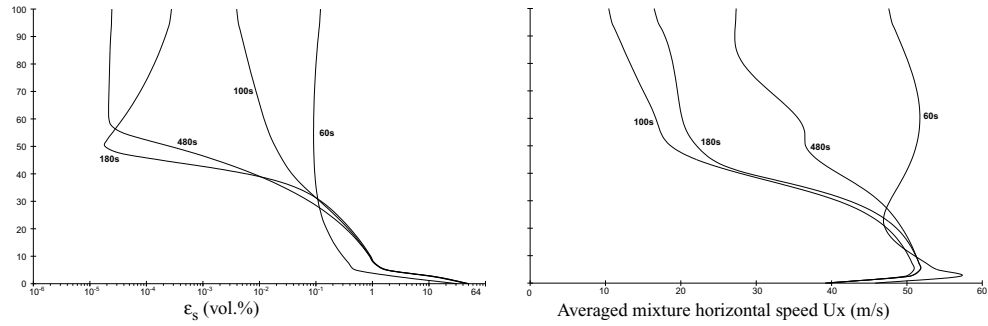

D. Fixed position sampling at 4 km from source:

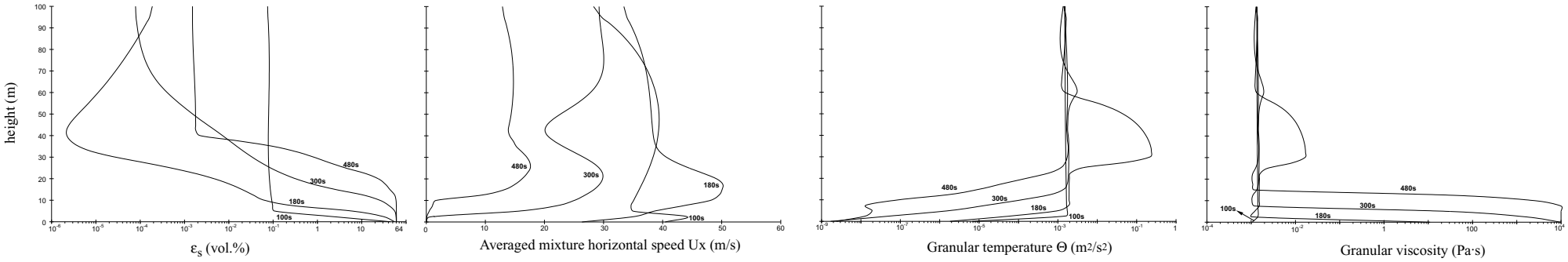

A. Variable position and time sampling within the head of the flow:

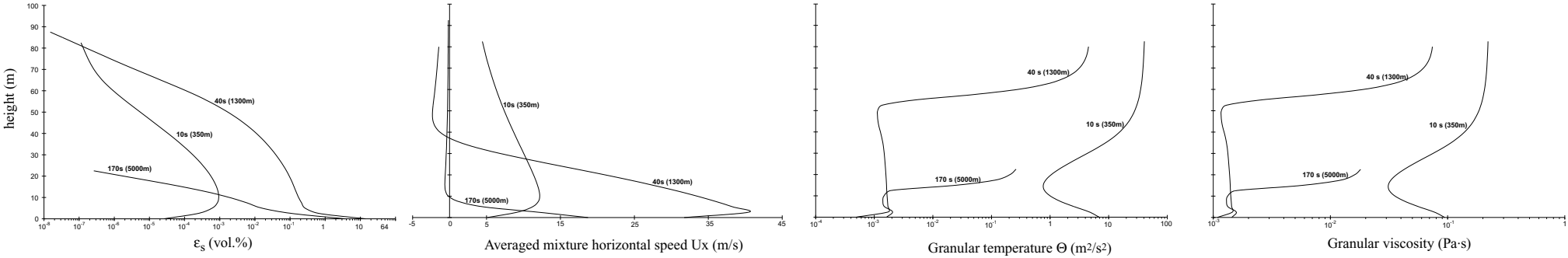

B. Fixed position sampling at 0.25 km from source:

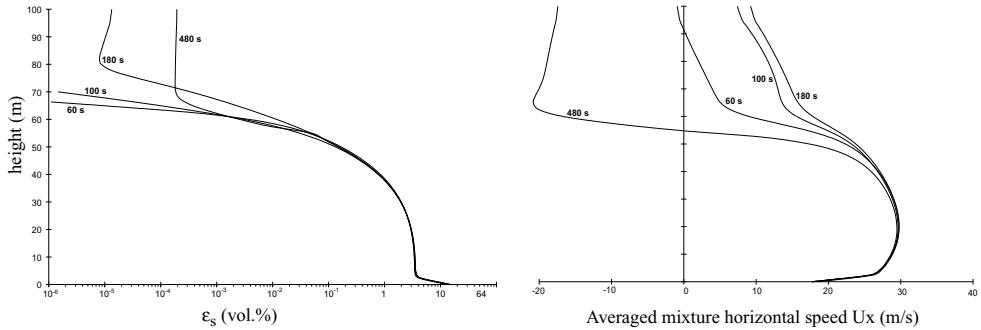

C. Fixed position sampling at 2.5 km from source:

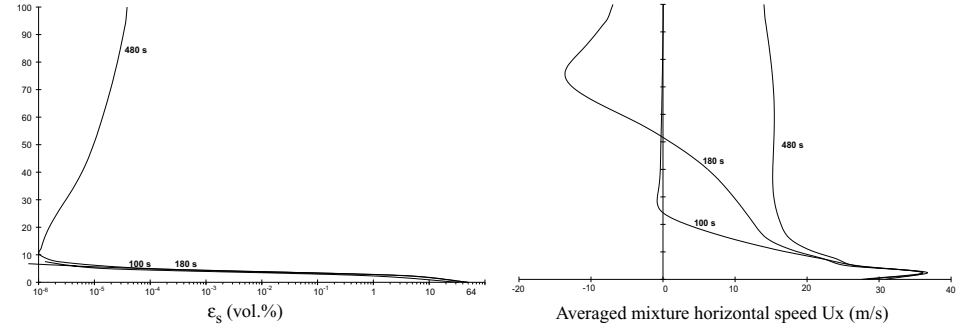

D. Fixed position sampling at 3.7 km from source:

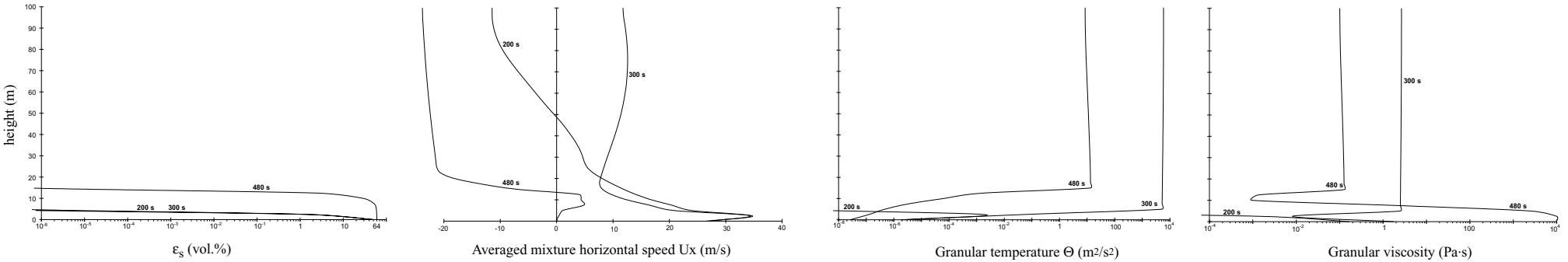

Inviscid Flow Model
PF_3

Chapter 3 - Figure 23

Kinetic-Collisional-Frictional Flow Model
PF_1

A. Volumetric grain concentration sampled at 5.2 km from source

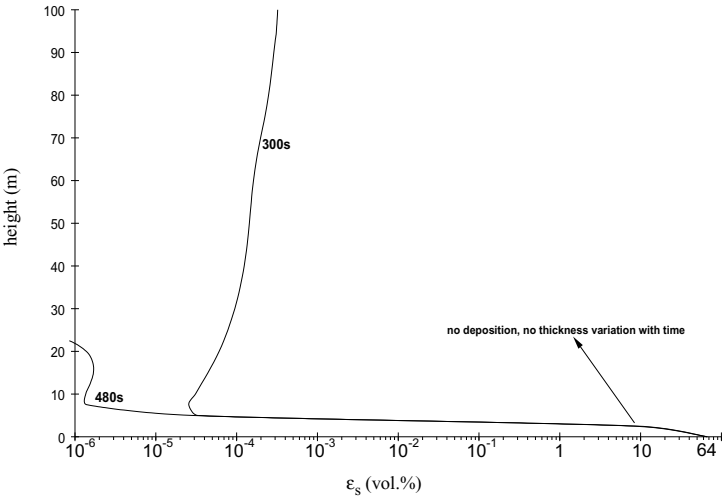

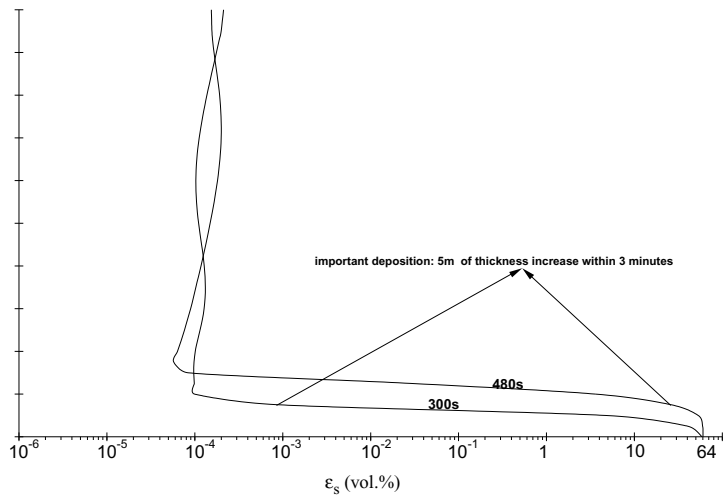

B. Averaged mixture horizontal speed sampled at 5.2 km from source

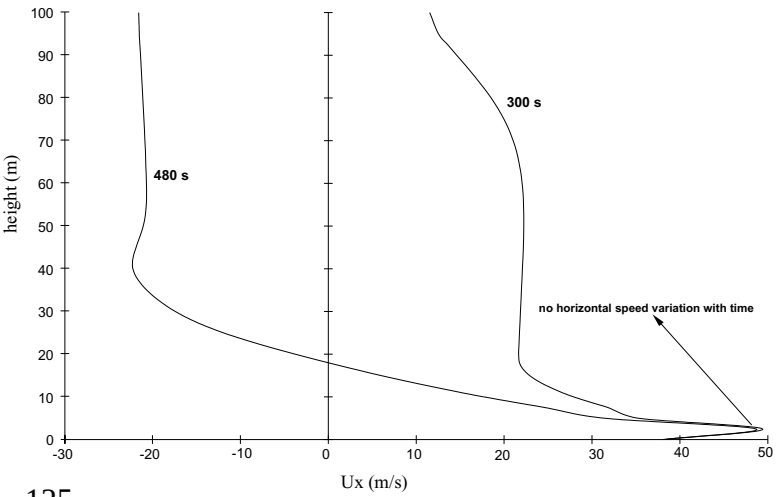

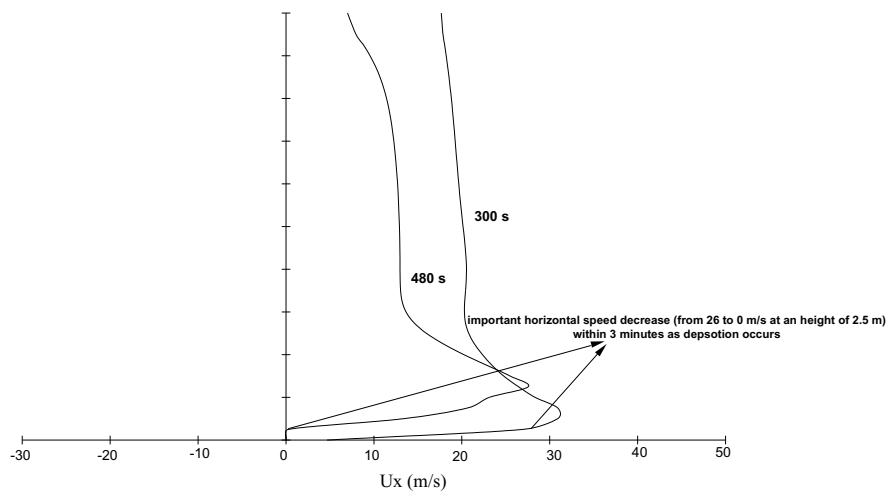

Chapter 3 – Annex 5: Grid-size independence for plinian cloud simulations

Although previous studies have shown that MFIX codes produce results independent on the grid-size [*Guenther and Syamlal, 2001*], it is essential to see whether this is still the case in a typical geophysical-atmospherical plinian column simulation. This is important to establish owing the relative poor resolution of all our simulations and the simplifications in our model [*Dartevelle, 2003b*]. Of course, a highly coarse grid-size will produce unrealistic physics or no solution will be reached but, on the other hand, the values of any seemingly realistic solutions can only be valued if grid-size independence is somehow demonstrated within the typical range of grid-size used in this project. For instance, if a plinian column collapses, would it be related to its physical conditions or would it be related to grid-size issues?

The next table presents two identical simulations achieved with different grid-size. One has a grid-size of 50 m over the whole height and over a radial distance of 6.2 km, while the second has a grid-size of 100 m over the whole height and over a radial distance of 6.2 km. The figure of this annex shows the results over one hour for both simulations. Clearly no significant differences can be seen even if as expected more details in the eddy structures and the umbrella shape (multi-layered, thickness) appeared between both simulations. However, both radial distance and top altitude are essentially the same.

Table 8:

Eruption	Grid 50 m	Grid 100 m
Geometry	Cylindrical	
Vertical length Y (km)	30	30
Vertical resolution ΔY (m)	50	100
Number of grid-point in the Y-direction	601	301
Radial length X (km)	30	30
Radial resolution from 0 to 6.2 km ΔX (m)	50	100
Radial resolution from 6.2 to 7.0 km ΔX (m)	100	100
Radial resolution from 7.0 to 7.4 km ΔX (m)	200	
Radial resolution from 7.4 to 8.2 km ΔX (m)	400	
Radial resolution from 8.2 to 9.0 km ΔX (m)	800	
Radial resolution from 9.0 to 30.0 km ΔX (m)	1000	
Number of grid-point in the X-direction	158	96
Vent diameter (m)	200	
Mixture vertical speed V_y (m/s)	80	
Volumetric solid concentration ε_s (vol.%)	0.1	
Grain diameter d (μm)	50	
Grain microscopic density ρ_s (kg/m^3)	1500	
Mixture temperature at the vent T_m (K)	900	
Gas pressure at the vent P_g (Pa)	10^5	
Mass fraction of water vapor at the vent	1.0	
Calculated mixture density ρ_m (kg/m^3)	1.74	
Calculated mass flux (kg/s)	1.75×10^7	

Table 8

Initial and boundary conditions for two plinian cloud simulations achieved with two different grid-size.

Chapter 3 – Annex 1, Figure “Grid independence”

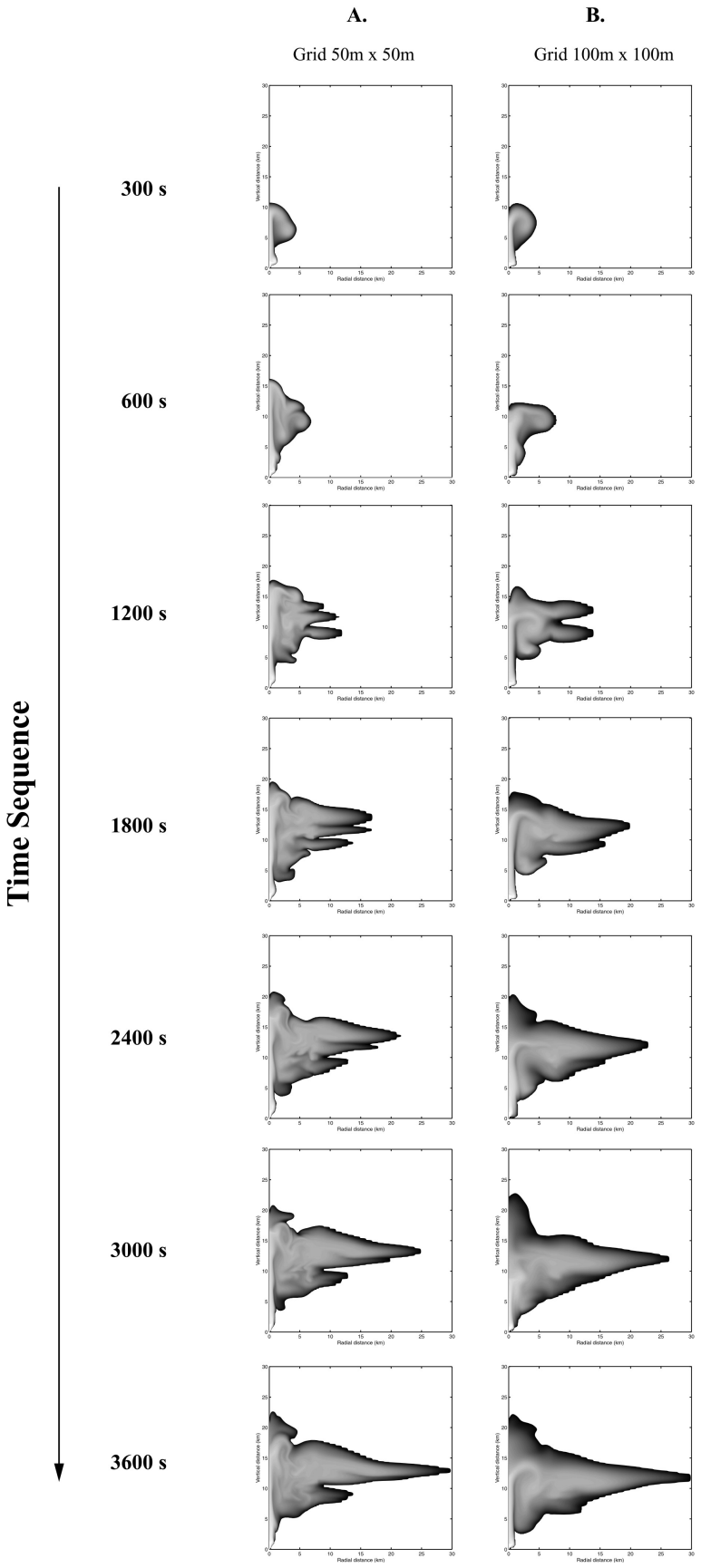

Chapter 3 – Annex 6: Overview of the numerical schemes used in MFIX and (G)MFIX

In a typical multiphase system, the momentum and energy equations (and also mass if phase transition occurs) are highly coupled through exchange terms. Those exchange terms strongly couple the components of velocity, temperature (and possibly mass) in a given phase to the corresponding variable in the other phase. This property is called the "interequation coupling". In addition, the discretized equations are nonlinear because the coefficients of the discretized equation depend on the values of the variable to be found. (G)MFIX uses a semi-implicit numerical scheme which must specifically deal with the interequation coupling and the nonlinearity of the discretized equations. To linearize the equations, the iterative method of Newton could be used [*Press et al., 1986*] but it is more economical and practical, particularly for the momentum equations, to use the Patankar and Spalding's SIMPLE algorithm (**S**emi-**IM**plicit for **P**ressure **L**inked **E**quations) [*Patankar, 1980; Spalding, 1981, 1983*; *Patankar et al., 1998; O'Rourke et al., 1998; Syamlal, 1998; Pannala et al., 2003*]. In the SIMPLE algorithm (Table 9), a system of coupled implicit equations is solved by associating with each equation an independent solution variable and solving implicitly for the value of the associated solution variable that satisfies the equation, while keeping the other solution variables fixed. For instance, pressure appears in all the momentum equations of all the phases (gas pressure in the gas momentum equations and solid pressure in the solid momentum equations), therefore making the velocity components dependent on the pressure value and vice-versa (hence making the momentum equations nonlinear). Therefore, in the gas momentum equations, the pressure is chosen as independent variable and special treatment is used for solving the gas pressure (i.e., the pressure correction equation of *Patankar* [*1980*]; see also *Spalding* [*1983*], *Patankar et al*. [*1998*]; *Syamlal* [*1998*]). In the solid momentum equation, the solid volume fraction is chosen as independent variable (i.e., the solid volume fraction correction equation) [*Syamlal*, *1998*]. To help convergence during the SIMPLE iteration process, an underrelaxation technique is used to slow down the changes in the coefficient from iteration to iteration with an under-relaxation factor, ω, less than unity [*Patankar et al., 1998*] (see Table 9). The interequation coupling must be dealt with some degree of implicitness to ensure fast convergence in anticipating the effects of a change in the local property of one phase on the properties of the other phase at the same location and simultaneously [*Spalding, 1981*]. This is accomplished with the **P**artial **E**limination **A**lgorithm (PEA) of *Spalding* [*1981*] (see also, *Syamlal* [*1998*]). With PEA, in a given phase, all the coefficients of the discretized equations involving the exchange terms (e.g., momentum exchange, K, and heat transfer, Q, between phases see Eq.(T1.5) to Eq.(T1.8) in *Dartevelle*

[*2003b*]) and the value of the corresponding variable from the other phase (e.g. velocities and temperature) are treated as source terms evaluated from the previous time-step iteration [*Syamlal, 1998*]. Once both linearization and interequation are dealt with, within the SIMPLE algorithm, (G)MFIX can solve the discretized equation using a classical linear solver iterative method (a point iteration, also called relaxation), such as the SOR method (successive over-relaxation, which is an improved version of the Gauss-Seidel iterative method; e.g., see *Kapitza and Eppel* [*1987*]), the generalized minimal residual method (GMRES; *Saad and Schultz* [*1986*]), and a more stable variant of the biorthogonal-conjugate gradient method (BI-CGSTAB; *van der Vorst* [1*992*]). See Table 9 for the specific linear solver/variable combination used in our simulations.

(G)MFIX uses an automatic time-step adjustment to reduce the total run-time in achieving the best time step/number of iteration needed for convergence ratio at any given simulation time [*Syamlal, 1998*]. For instance, the semi-implicit algorithm imposes a very small time-step for very dense gas-solid flow simulations or whenever sharp gradient develops within the flow field. On the other hand for quasi-steady diluted flows, a small time-step would make the run unnecessarily long. MFIX monitors the total number of iterations needed for convergence for several previous time-steps. If there is a favorable reduction in the number of iterations per second of simulation, then a small upward time-step adjustment is performed. Or, for instance, if the simulation fails to converge for a given time-step, then the time-step is decreased till convergence is obtained [*Syamlal, 1998*]. Convergence of iterations in the linear equation solvers is judged from the residuals of various equations over the whole computational domain. Convergence is declared whenever each residual of each discretized equation within the same iteration tends to zero. If the residuals are not reduced, a supplementary iteration will be performed. If convergence is not obtained within a specified number of iterations (30 in our simulations), or if the system is divergent, then nonconvergence is declared and the time-step is decreased.

(G)MFIX uses portable OPEN-MP (for shared memory multi-processors) and MPI (for distributed memory parallel computers) in a unified source code. The MFIX codes has been ported to a Beowulf Linux cluster, SGI SMP, Compaq SC cluster, IBM SP, and Windows2000/XP workstation (2 to 4 CPUs in SMP) and can be used on Hybrid-computer SMP-DMP [*Pannala et al., 2003*; G. Bergantz, personal communication, 2003].

Table 9

Multiphase SIMPLE algorithm in relation with Partial Elimination Algorithm and linear solver techniques used in the (G)MFIX codes. For the calculation techniques of pressure correction equation, solid volumetric correction equation, velocity field correction equations, under-relaxation factors, and Partial Elimination Algorithm: see *Patankar* [*1980*], *Spalding* [*1983*], *Syamlal* [*1998*], and *Patankar et al*. [*1998*]. For the linear equation solver techniques, such as successive over-relaxation method (SOR) and the biorthogonal-conjugate gradient stable method (BI-CGSTAB), see *Kapitza and Eppel* [*1987*] and *van der Vorst* [*1992*] respectively. All symbols are defined in the Appendix 1 of the companion paper [*Dartevelle, 2003b*]. When starting a new time-step (step 1), the physical properties and exchange coefficient are given in Table 3/Table 4, and Table 2 respectively in *Dartevelle* [*2003b*]. Typically between 5 to 20 iterations are needed before declaring convergence. Note that at convergence the gas pressure ($\ddot{}P_g$) and solid volume fraction ($\ddot{}\varepsilon_s$) corrections must go to zero [*Syamlal, 1998*].

Table 9:

"SIMPLE" algorithm for multiphase granular flows in MFIX and (G)MFIX codes

1. Start of a new time-step iteration. Calculate physical properties, exchange coefficients, and reaction rates (if any).
2. Calculate guessed velocity fields of both solid and gas phase ($^{o}\mathbf{u}_s$ and $^{o}\mathbf{u}_g$) based on the available current pressure fields ($^{o}P_s$ and $^{o}P_g$) and volumetric concentrations ($^{o}\varepsilon_s$ and $^{o}\varepsilon_g$). Use SOR and PEA.
3. Calculate the gas pressure correction with BI-CGSTAB: $\ddot{}P_g$.
4. Update the gas pressure field with under-relaxation technique: $P_g={}^{o}P_g+\varpi_g\ddot{}P_g$, where the under-relaxation factor for the gas phase: $0<\varpi_g<1$.
5. Calculate gas velocity correction fields ($\ddot{}\mathbf{u}_g$) from $\ddot{}P_g$ and update velocity fields: $\mathbf{u}_g={}^{o}\mathbf{u}_g+\ddot{}\mathbf{u}_g$.
6. Calculate tentative estimates of solid velocity field knowing the updated $\mathbf{u}_g$ and P_g values: $^{1}\mathbf{u}_s$.
7. Calculate the solid volumetric concentration correction with SOR: $\ddot{}\varepsilon_s$.
8. Calculate solid velocity correction fields ($\ddot{}\mathbf{u}_s$) and update velocity fields: $\mathbf{u}_s={}^{1}\mathbf{u}_s+\ddot{}\mathbf{u}_s$.
9. Update the solid volumetric concentration: $\varepsilon_s={}^{o}\varepsilon_s+\varpi_s\ddot{}\varepsilon_s$, where the under-relaxation factor for the solid phase:
   - if $\ddot{}\varepsilon_s>0$ (i.e., solid volumetric faction is increasing) and $\varepsilon_s>{}^{f}\varepsilon_s$ (i.e., where the contact between particle is frictional), then $0<\varpi_s<1$.
   - otherwise, $\varpi_s=1$.
10. Update the gas volumetric concentration: $\varepsilon_g=1-\varepsilon_s$.
11. Update the solid pressure field P_s from ε_s.
12. Calculate solid and gas temperatures with BI-CGSTAB and PEA.
13. Calculate the granular-temperature (if needed) with BI-CGSTAB.
14. Check for convergence judged from the normalized residuals of the linear equation solvers used in Step 2, 3, 7, 12, and 13:
    - if reached, start the next time-step (step 1) and automatically adjust the time-step.
    - if not reached, restart the iteration process (step 2) with the new corrected velocity fields, pressure fields, and concentration values.